Performance Investigation of a Turbocharger Compressor

by

Andrew Louis de Wet

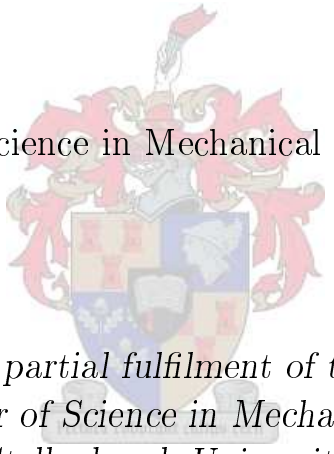

Master of Science in Mechanical Engineering

Thesis presented in partial fulfilment of the requirements for the degree of Master of Science in Mechanical Engineering at Stellenbosch University

Department of Mechanical and Mechatronic Engineering,
University of Stellenbosch,
Private Bag X1, Matieland 7602, South Africa.

Supervisor: Prof. T.W. von Backström
Co-supervisor: Mr. S.J. van der Spuy

December 2011

Declaration

By submitting this thesis electronically, I declare that the entirety of the work contained therein is my own, original work, that I am the owner of the copyright thereof (unless to the extent explicitly otherwise stated) and that I have not previously in its entirety or in part submitted it for obtaining any qualification.

Signature: .....
A.L. de Wet

Date: 2011/11/16 .....

Abstract

Performance Investigation of a Turbocharger Compressor

A.L. de Wet

Department of Mechanical and Mechatronic Engineering,
University of Stellenbosch,
Private Bag X1, Matieland 7602, South Africa.

Thesis: MScEng (Mech)

December 2011

Stellenbosch University participated in a project to re-design the compressor section of a diesel locomotive turbocharger. Tests conducted on the prototype compressor showed possible rotating stall in the diffuser section before the designed higher pressure ratio could be achieved. When approaching the higher pressure ratio, the compressor inlet trunk started to rhythmically collapse (due to suction), the engine shook and bellows of black smoke were exhausted by the engine. It was decided to simulate the prototype compressor's operation by using the 1-D theory of Aungier (2000) and to perform a 3-D CFD analysis of the compressor using FINE™/Turbo of NUMECA International.

A verification process was followed to show the accuracy of the 1-D and 3-D modelling methods using two well-known centrifugal compressor test cases found in the literature, namely the O-Rotor by Eckardt (1975, 1976, 1980) and the "Radiver" open CFD test case by Ziegler *et al.* (2003*c*). Results from the models were compared to available experimental results and the accuracy was found to be sufficient to investigate the prototype compressor's impeller and diffuser.

Both prediction methods confirmed separation in the vaned diffuser across the entire operating flow range of the prototype compressor at the design impeller speed. The 3-D method identified supersonic flow at the vaned diffuser inlet at the operating point and also predicted a smaller operating range than originally anticipated. Both the 1-D and 3-D methods also predicted impeller blade stall over the entire operating flow range at the design impeller speed.

A recommendation was made to redesign the impeller and diffuser of the prototype compressor.

Keywords: CFD, NUMECA, Aungier, Eckardt, Radiver, centrifugal compressor.

Uittreksel

Ondersoek in die Werkverrigting van 'n Turbo-aanjaer Kompressor

("Performance Investigation of a Turbocharger Compressor")

A.L. de Wet

Departement Meganiese en Megatroniese Ingenieurswese,
Universiteit van Stellenbosch,
Privaatsak X1, Matieland 7602, Suid Afrika.

Tesis: MScIng (Meg)

Desember 2011

Die Universiteit van Stellenbosch het deel geneem aan 'n projek om die kompressor gedeelte van 'n diesel lokomotief se turbo-aanjaer te herontwerp. Toetse uitgevoer op die prototipe kompressor het moontlike roterende wegbreking in die diffuser seksie uitgewys voordat die ontwerpte hoër drukverhouding bereik kon word. Toe die hoër drukverhouding genader is, het die kompressor inlaatpyp begin ritmies inmekaar vou (as gevolg van die suig aksie), die enjin het geskud en wolke swart rook is deur die enjin uitgeblaas. Die besluit is geneem om die prototipe kompressor se werking te simuleer met behulp van die 1-D teorie van Aungier (2000) en om ook 'n 3-D berekenings vloeimeganika (BVM) analise op die kompressor uit te voer met behulp van FINE™/Turbo van NUMECA Internasionaal.

'n Verifikasieproses is gevolg om die akkuraatheid van die 1-D en 3-D modelle te illustreer met behulp van twee welbekende sentrifugaal kompressor toetsgevalle beskikbaar in die literatuur, naamlik die O-Rotor deur Eckardt (1975, 1976, 1980) en die "Radiver" oop BVM toetsgeval deur Ziegler *et al.* (2003*c*). Resultate van die modelle is vergelyk met beskikbare eksperimentele resultate en die bevinding is gemaak dat die akkuraatheid genoegsaam is om die prototipe kompressor se rotor en diffuser te ondersoek.

Beide voorspellingsmetodes het wegbreking bevestig in die gelemde diffuser oor die hele werksbestek van die prototipe kompressor teen die ontwerp rotor-

spoed. Die 3-D metode het supersoniese vloei by die gelemde diffuser se inlaat by die bedryfspunt geïdentifiseer en het ook 'n kleiner werksbestek voorspel as wat vroeër verwag is. Beide die 1-D en 3-D metodes het ook wegbreking in die rotor oor die hele werksbestek teen die ontwerp rotorspoed voorspel. 'n Voorstel is gemaak om die rotor en diffuser van die prototipe kompressor te herontwerp.

Sleutelwoorde: BVM, NUMECA, Aungier, Eckardt, Radiver, sentrifugaal kompressor.

Acknowledgements

I wish to express my sincere gratitude to the following individuals and institutions who accompanied me on this journey:

- Our Allmighty God who knows how to keep my path interesting and makes provision for me to surmount obstacles.
- My parents, Louis and Suzanne, who noticed my passion for engineering before I did and encouraged me to pursue it.
- My loving wife, Gretha, for encouraging and motivating me to finish this thesis.
- All my friends and family who never lost faith in me whilst I was busy with this project. There are too many to single out.
- My two supervisors for their encouragement and guidance during the project. Prof. T.W. von Backström who is always patient and Mr. S.J. van der Spuy who kept believing in my determination to finish.
- Ballast, Prof. T.W. von Backström and Mr. S.J. van der Spuy for providing and facilitating financial support.
- The use of the high performance cluster at Stellenbosch University.

Dedications

To Prof. G.D. Thiart...

Contents

List of Figures

List of Tables

Nomenclature

Constants

$\pi =$ 3.141 592 654

$R =$ 287 J/kg·K

Symbols

A	Total blade passage area	[m^2]
A_R	Area ratio	[−]
a/c	Point of maximum camber	[−]
B	Fractional area blockage	[−]
b	Hub-to-shroud passage width	[m]
C	Absolute velocity	[m/s]
C_L	Correction coefficient, see Equation (B.2.15)	[−]
C_M	Disk torque coefficient	[−]
C_p	Specific heat at constant pressure	[J/kg · K]
$\overline{C}_R$	Correction coefficient, see Equation (B.2.17)	[−]
C_r	Contraction ratio	[−]
C_θ	Correction coefficient, see Equation (B.2.15)	[−]
c_f	Skin friction coefficient	[−]
D	Divergence parameter	[−]
D_{eq}	Equivalent diffusion factor	[−]
D_m	Diffusion criterion parameter	[−]
d	Diameter	[m]
E	Empirical diffusion efficiency	[−]
e	Peak -to-valley surface roughness	[m]
f_c	Correction factor	[−]
h	Enthalpy	[J/kg]
h_{th}	Blade-to-blade throat width	[m]
I	Work input coefficient	[−]
i	Incidence angle $(\beta - \alpha)$	[°]

K	Clearance gap swirl parameter, vaned diffuser stall parameter	$[-]$
K_0	Zero leakage swirl parameter, unguided vaned diffuser stall parameter	$[-]$
K_1	Correction coefficient, see Equation (B.2.17)	$[-]$
K_2	Correction coefficient, see Equation (B.2.17)	$[-]$
k	Turbulent kinetic energy, hyperbola constant	$[\mathrm{m^2/s^2}, \mathrm{m^2}]$
L	Mean streamline meridional length, dimensionless diffuser blade loading parameter	$[\mathrm{m}]$
L_B	Full blade or vane mean streamline camberline length	$[\mathrm{m}]$
Ma	Mach number	$[-]$
m	Meridional length	$[\mathrm{m}]$
$\dot{m}$	Mass flow rate	$[\mathrm{kg/s}]$
N	Rotation speed	$[\mathrm{RPM}]$
PR	Pressure ratio	$[-]$
p	Absolute pressure	$[\mathrm{Pa}]$
peri	Perimeter	$[\mathrm{m}]$
p_v	Velocity pressure $(p_t - p)$	$[\mathrm{Pa}]$
R	Rothalpy	$[\mathrm{J/kg}]$
Re	Reynolds number	$[-]$
r	Radius	$[\mathrm{m}]$
s	Clearance gap, specific entropy	$[\mathrm{m}, \mathrm{J/kg \cdot K}]$
T	Absolute temperature	$[\mathrm{K}]$
t_b	Blade thickness	$[\mathrm{m}]$
U	Blade speed (ωr), leakage tangential velocity	$[\mathrm{m/s}]$
V	Velocity	$[\mathrm{m/s}]$
v^*	Friction velocity	$[\mathrm{m/s}]$
W	Relative velocity	$[\mathrm{m/s}]$
w	Vane-to-vane passage width	$[\mathrm{m}]$
X	Choke parameter	$[-]$
x	Hyperbola horizontal coordinate	$[\mathrm{m}]$
y	Hyperbola vertical coordinate, distance from wall	$[\mathrm{m}]$
y^+	Dimensionless wall distance	$[-]$
y_{wall}	Wall cell height	$[\mathrm{m}]$
z	Number of blades or vanes	$[-]$
α	Flow angle with respect to tangent	$[^\circ]$

α_C	Mean streamline angle with respect to zenith axis	[rad]
β	Blade angle with respect to tangent	[°]
γ	Specific heat ratio	[−]
Δ	Difference	[−]
δ	Boundary layer thickness, dimensionless pressure correction factor	[m]
δ^*	Minimum-loss deviation angle	[°]
$\partial\delta/\partial i$	Variation of deviation angle with incidence, see Equation (B.2.24)	[−]
ϵ	Impeller mean streamline radius ratio (r_1/r_2)	[−]
η	Isentropic efficiency	[%]
θ	Dimensionless temperature correction factor, camber angle	[°]
κ_m	Mean streamline curvature	[rad/m]
λ	Tip distortion factor	[−]
μ	Dynamic viscosity coefficient	[kg/s · m]
ρ	Density	[kg/m^3]
σ	Slip factor, point of maximum solidity	[−]
σ^*	Parameter to determine ϵ_{LIM}, see Equation (B.1.2)	[−]
τ	Torque	[N · m]
ϕ_2	Tip flow coefficient	[−]
ω	Rotation speed $(2N\pi/60)$, specific dissipation rate	[rad/s, 1/s]
$\overline{\omega}$	Total pressure loss coefficient	[−]
$2\theta_C$	Diffuser divergence angle	[°]

Superscripts

$*$	Reynolds number effect investigation results, sonic flow condition, optimum

Subscripts

B	Blade
BL	Blade loading
C	Impeller cover, curvature
CH	Choke
CL	Shroud clearance gap
CM	Torque coefficient
CR	Critical

$corr$	Corrected
D	Impeller disk, diffusion, diffuser
DF	Disk friction
DIF	Diffusion
e	Boundary layer edge
FB	Full blades
H	Hydraulic
h	Hub
INA	Standard inlet conditions
i	Index for total pressure loss and work input coefficient
$ideal$	Ideal value
j	Index for vaneless annular passage control volume
inc	Incidence
$inc0$	Minimum incidence
$inlet$	CFD inlet boundary
L	Leakage
LE	Leading edge
LIM	Limit
m	Meridional velocity component
max	Maximum value
mix	After mixing at the impeller tip or diffuser discharge
$outlet$	CFD outlet boundary
PS	Pressure surface
R	Recirculation
r	Rough
ref	Reference value
S	Stall
SB	Splitter blades
SEP	Separation
SF	Skin friction
SS	Suction surface, static-to-static ratio
s	Shroud, smooth
sh	Shock
TT	Total-to-total ratio
t	Total thermodynamic condition, turbulent
th	Throat

U Tangential velocity component
wake Before mixing at the impeller tip or diffuser discharge

λ Abrupt expansion

0 Impeller eye condition
1 Impeller inlet condition
2 Impeller tip condition
3 Diffuser inlet condition
4 Diffuser discharge condition

Auxiliary Symbols

$'$ Value relative to rotating frame of reference
$\bar{}$ Average of values

Acronyms

A-D DEEP prototype measurement planes, see Figure 4.3
B2B Blade-to-blade
CD-ROM Compact disk read-only memory
CFD Computational fluid dynamics
CGNS Computer format for storage and retrieval of CFD data
CV Control volume
GUI Graphical user interface
H&I AutoGrid5™ grid topology
HOH AutoGrid5™ grid topology
H2S Hub-to-shroud
IGES 3-D computer model format
IGV Inlet guide vane
INEWKE Expert parameter of the EURANUS™ solver
k-ϵ Turbulence model
k-ω Turbulence model
L2F Laser-2-focus
M1-M3 O-Rotor measurement points
O4H AutoGrid5™ grid topology
P1 Radiver operating point
R-S Rotor-stator
RMS Root-mean-square

S-A Spalart-Allmaras
SST Shear stress transport
S2 Radiver choke limit
TORRO Expert parameter of the EURANUS™ solver
v^2-f Turbulence model

1-D One-dimensional
3-D Three-dimensional
1M-8M Radiver test case measurement planes, see Figures 3.13 and 3.14

Chapter 1

Introduction

An opportunity to redesign a centrifugal compressor arose from a project during 2003, which was known as the "Diesel Engine Efficiency Programme" (DEEP) (Van der Spuy, 2003). This joint venture was undertaken between Cape Advanced Engineering (CAE, trading as Stellenbosch Automotive Engineering), the Department of Mechanical Engineering at Stellenbosch University and the Council for Scientific and Industrial Research (CSIR) of South Africa to redesign the General Electric (GE) 7S1408 A1 diesel locomotive turbocharger.

The client was the South African national railroad company, Spoornet, where the GE 7S1408 A1 turbocharger is still in use on the GE 7FDL-12 engine. This engine is utilised in the GE U26C diesel locomotive (referred to as the Class 34 diesel locomotive by Spoornet). The project was headed by Mr. A. Stone of CAE and the aim was to improve power output by 15 % and to reduce the specific fuel consumption by 5 % of the V12 diesel engine. Besides redesigning the turbocharger, the intercooling system was improved by separating the liquid cooled intercooler coolant from the engine coolant by utilising a secondary coolant circuit.

1.1 Previous Work

The CSIR found that the turbine stage needed no re-rating and only redesigning the compressor stage was investigated further. The redesigned compressor was named the DEEP prototype and the impeller utilised backswept blades including splitter blades and the logarithmic spiral type diffuser was replaced by a flat plate profile (patented by Concepts ETI™) type diffuser. Unfortunately significant stall occurred in the DEEP compressor during testing before the designed higher pressure ratio could be reached. Figure 1.1 shows the designed operating line reaching a total-to-total pressure ratio of 3.25, but the two measured operating lines experiencing choke at a lower total-to-total pressure ratio of roughly 2.8. The improved intercooling system was included in the test and

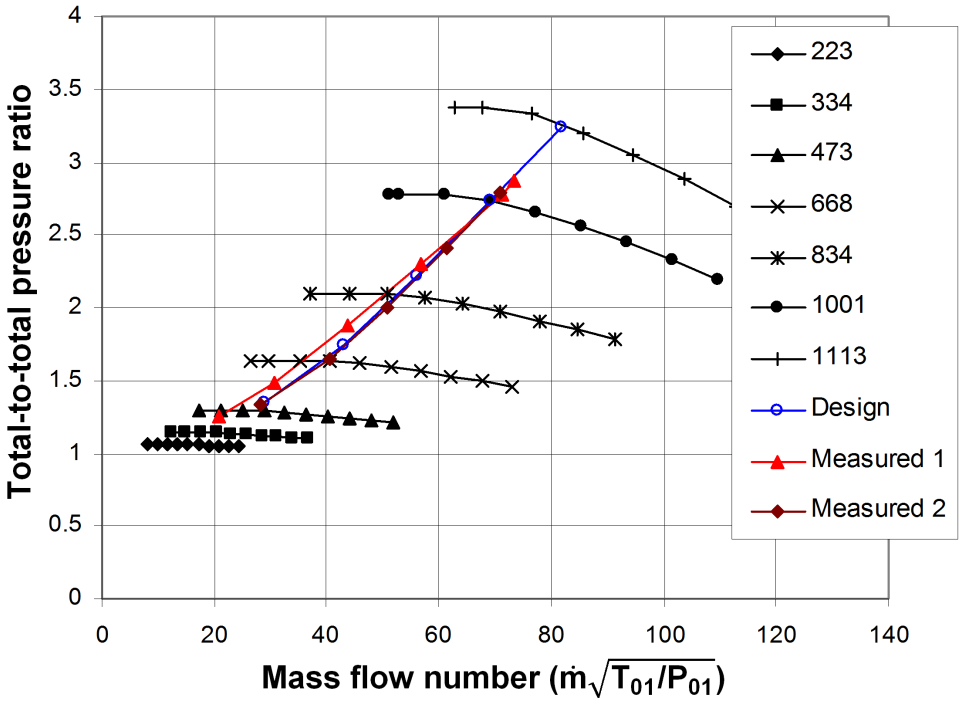

Figure 1.1: DEEP prototype designed and measured non-dimensionalised compressor data (Van der Spuy, 2003).

the highest stable operating engine power was measured as 2025 kW, which is a 4.4 % increase from the maximum rated output of 1940 kW.

The occurrence of stall was also observable by rhythmic collapsing (due to suction) of the compressor inlet trunk, shaking of the engine and bellows of black smoke being exhausted by the engine when approaching the higher pressure ratio. Stall in the vaned diffuser was confirmed by Van der Spuy (2003) during initial 3-D Computational Fluid Dynamics (CFD) modelling utilising the commercial CFD code CFX™.

1.2 Problem Statement and Study Objective

The DEEP project came to an end before any re-design of the DEEP compressor could be performed and a reliable improved compressor could not be delivered to the client.

It is the aim of this thesis to determine where the aerodynamic stall occurs in the DEEP prototype and provide recommendations on the problematic component or components to improve the performance and reliability of the compressor. This investigation will be performed using one- and three-dimensional (1-D and 3-D) analysis approaches.

The 1-D analysis relies on a combination of fundamental analysis and empirical loss models along a mean stream surface presented by Aungier (2000),

who divided the theory into the main components of a centrifugal compressor. Not all of the sub-component theories were implemented and only those relevant to the thesis compressors were coded using a programming language familiar to the author, MATLAB®. These sub-component theory codes are for the impeller itself, the vaneless annular passage and the vaned diffuser. The MATLAB® codes will be verified using two well-known case studies, namely the O-Rotor of Eckardt (1975, 1976, 1980) and the "Radiver" open CFD test case by Ziegler *et al.* (2003*c*).

The 3-D analysis will be conducted using CFD software of NUMECA™ International, namely FINE™/Turbo. FINE™/Turbo specialises in the automatic meshing of turbomachinery components and simple setup of the solver which has been tailored to accommodate rotating components. Terminology from the turbomachinery field are evident throughout the entire package with the post-processing of results also including dimensionless parameters associated with turbomachinery evaluation. The software package can be divided into three programs; namely AutoGrid5™ for meshing, FINE™/Turbo for solving and CFView™ for post-processing of results. Furthermore, the package can be extended to facilitate detailed 3-D turbomachinery geometry design using AutoBlade™.

FINE™/Turbo has not been used at the Department of Mechanical and Mechatronic Engineering of Stellenbosch University when the thesis study commenced, but was chosen due to the niche market of turbomachinery CFD analysis it addresses. Due to the inception of using FINE™/Turbo at the academic institution, the above-mentioned case studies will also be used to verify the 3-D modelling capabilities of FINE™/Turbo.

With credibility obtained in both the 1-D and 3-D analysis approaches through benchmarking with the O-Rotor and Radiver test cases, the prototype compressor stage will be investigated, identifying the problematic components, upon which recommendations for improvement will be made. No comparisons with the CFX™ results of Van der Spuy (2003) will be made.

Chapter 2

Literature Study

A good starting point in explaining basic turbomachinery principles is to present a discussion on the geometry and operating principles of the centrifugal compressor components relevant to this thesis. After this the 1-D analysis procedure of Aungier (2000) will be discussed followed by a summary of FINE™/Turbo and a discussion on CFD modelling methods.

2.1 Basic Centrifugal Compressor Operating Principles

The centrifugal compressor stage geometry relevant to this thesis can be divided into different components which can be viewed in Figure 2.1. No Inlet Guide Vanes (IGV's) or return channels are included in this figure as the test cases and prototype compressor stage do not employ such geometry.

For visual reference the reader can view a photo of the GE 7S1408 A1 compressor impeller viewed from the inlet in Figure 2.2. The impeller is the only rotating component in a centrifugal compressor stage. Dixon (2005) provides the following simple explanation of the operating principle of a centrifugal compressor.

The fluid enters the impeller from the inlet casing into the eye (which is bound by the hub and shroud). Typically this flow is in the axial direction and is assumed to be uniform. Pre-whirl can be introduced to the fluid by means of IGV's. If a channelling system is employed to direct the fluid to the eye by means of pipe bends, the flow might not be uniform and could contain some whirl. If this is the case, either the use of IGV's to manage the flow or prediction of the velocity vector with the help of the return channel analysis procedure by Aungier (2000) is recommended.

The fluid then moves into the inducer section which starts at the eye and typically finishes in the region where the flow is starting to move into the radial direction (thus leaving the axial portion of the passage). This section can therefore be separate from or be part of the blades. The case where the

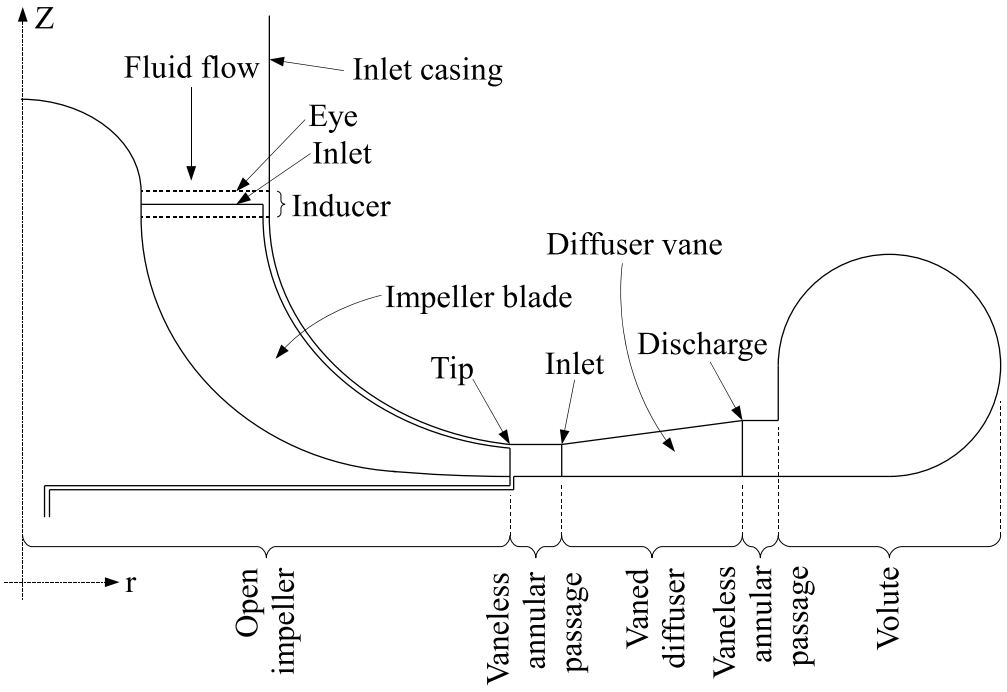

Figure 2.1: Centrifugal compressor component overview in the r-Z plane.

Figure 2.2: GE 7S1408 A1 compressor impeller (Courtesy of Johan van der Spuy).

Figure 2.3: GE 7S1408 A1 compressor diffuser (Courtesy of Johan van der Spuy).

blade leading edge extends up to the eye is known as a full-inducer impeller. Similarly, a semi-inducer impeller blade's inlet only extends partway into the inducer portion as can be seen in Figure 2.1. Lastly, in a few cases a radial impeller has blades only in the radial direction, hence the blades do not extend into the axial direction at all.

The inducer transfers the fluid smoothly into the blade passages where the rotating blades energise the fluid. The energy addition associated with this rotation results in a total enthalpy rise. A static pressure rise of the fluid is the result of it moving from the inlet to tip (otherwise known as the impeller outlet), which results in an increase in flow area and hence diffusion of the relative velocity. The increase in radius from inlet to tip as well as the transfer of angular momentum from the rotating blades cause an increase in angular momentum of the fluid, after which the fluid moves off the blades.

After the fluid leaves the impeller tip it enters a vaneless annular passage which facilitates some static pressure recovery. An example of a vaneless annular passage can be seen in Figure 2.3 between the inner diameter of the disk and the leading edge of the stationary vanes of the diffuser. If only the vaneless annular passage is present and extends up to the volute casing, it is known as a vaneless diffuser. Typically a vaneless annular passage is parallel sided where diffusion takes place from the impeller tip to either the vaned diffuser or volute inlet, depending on configuration. Aungier (2000) mentions the importance of this vaneless space to reduce possible high Mach number flows from the impeller tip to the vaned diffuser vanes in his design procedure for vaned diffusers.

Employing a vaned diffuser has the advantage of further static pressure

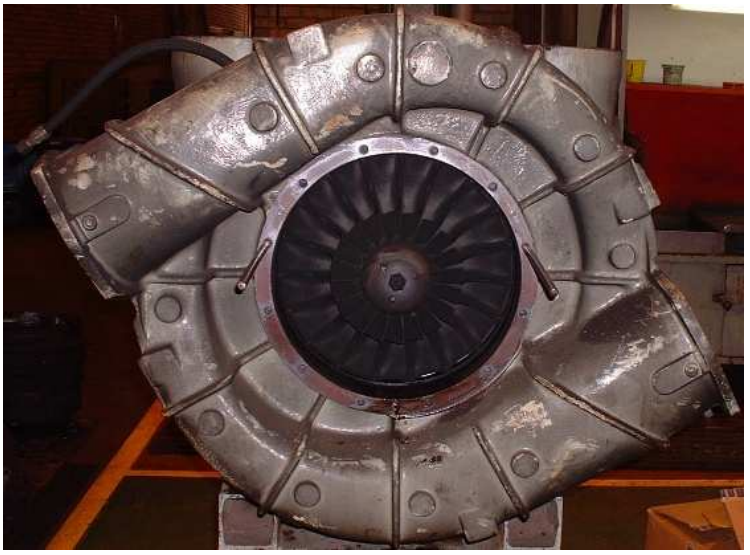

Figure 2.4: GE 7S1408 A1 compressor dual-exit volute (Courtesy of Johan van der Spuy).

recovery from the kinetic energy remaining in the fluid after it leaves the vaneless annular space (Dixon, 2005). An example of the GE 7S1408 A1 compressor diffuser can be viewed in Figure 2.3. According to Dixon (2005) the advantage of a vaned diffuser above a vaneless diffuser is a much smaller overall diffuser length which Sayers (1990) supports by adding that the diffusion occurs at a much higher rate with higher efficiency. But Aungier (2000) also mentions in his preliminary design approach how a vaned diffuser ceases to be effective at higher flow coefficients when compared to a vaneless diffuser, thus indicating a smaller operating range.

In some cases another vaneless annular space is present after the fluid discharges from the vaned diffuser. Aungier (2000) provides an explanation for this; if the maximum diffuser (volute casing) radius is supplied it might exceed the discharge radius calculated using the design approach for vaned diffuser sizing. The solution is to add a vaneless annular passage after the vaned diffuser discharge.

After the fluid leaves the vaneless annular passage or vaned diffuser it enters the volute (scroll) or collector which then smoothly collects the fluid and guides it into the discharge pipe. A collector is similar to a volute, but has a uniform cross-sectional area in it's circumferential direction. Figure 2.4 shows a photo of the GE 7S1408 A1 compressor dual-exit volute with the impeller visible in the center.

2.2 1-D Centrifugal Compressor Theory

In preparation for the thesis the author consulted the centrifugal compressor analysis guidelines provided by Aungier (2000). Attention was paid to Chapters 4 and 5 which comprise of a 1-D analysis along a mean stream surface. Chapter 4 discusses "The Impeller Work" input only, whereas Chapter 5 discusses the "One-Dimensional Aerodynamic Performance Analysis". The last-mentioned chapter covers the analysis of the entire compressor, including the inlet guide vanes, impeller performance, vaneless annular passage, vaned diffuser, return channel and volute or collector. Chapter 5 closes by discussing multistage compressor analysis.

A MATLAB® code was compiled to implement the theory from Aungier (2000). For the scope of this project, only the impeller, vaneless annular passage and vaned diffuser were coded as the other components are not included in the test cases (the Eckardt O-Rotor and "Radiver" open CFD test case as described in Sections 3.2 and 3.3) or in the "DEEP" prototype (as described in Section 4). The volute theory was excluded due to lack of test data including the volute or sufficient geometry of the volute.

Due to the majority of the compressor operating variables being initially unknown, the 1-D analysis procedure is iterative in nature and will be explained by means of a hand-calculation. The discussion is supported by detailed drawings providing the geometry of the required measurements, fluid mechanics in the form of velocity vector diagrams and also the thermodynamics in the form of Mollier charts.

2.2.1 Main Overview of Analysis Methodology

The analysis uses a skin friction model based on generalised pipe or channel friction data. This is implemented in both the impeller (using a rotating frame of reference), the vaneless annular passage (with the necessary adjustments made) and the vaned diffuser (with a stationary frame of reference).

As mentioned, the 1-D theory mainly relies on measurements taken along the mean stream surface, which is defined such that the passage flow area on either side of the surface is equal. This is true for both the impeller, vaneless annular passage and vaned diffuser theories.

The analysis methodology for each compressor component is modular and for each component analysis the appropriate boundary conditions are imposed. Downstream components receive their inlet boundary conditions from upstream results and it must be noted that upstream components are not influenced by downstream components. An example of this is that the length of the vaneless annular passage does not influence the impeller performance in any way.

Aungier (2000) mentions that the analysis has been qualified against more than a hundred different stages, with stage flow coefficients ranging from 0.009

to 0.16. But the analysis methodology's validation limits imply that it is only applicable to industrial compressors. Pressure ratios for detailed validation studies extend to 3.5, with the pressure ratio range being extended to 4.2 during actual application. Validity beyond this range cannot be guaranteed.

2.2.2 Impeller Performance

Aungier (2000) discusses the impeller work input in Chapter 4 of his book and the loss coefficients are discussed in Chapter 5. During implementation this entailed alternating between the two chapters. To avoid confusion, the analysis will be presented in the order as it was coded in MATLAB®. The analysis progresses from the impeller inlet to tip.

Assumptions are made to start the iterative calculation. All of the required geometry is provided and the operating fluid is assumed to be a perfect gas. The total inlet conditions ($T_{t,1}$ and $p_{t,1}$) and intended range of mass flow rates with a specific impeller rotational speed are known. Even though not a prerequisite, knowing the impeller total-to-total efficiency (η_{TT}) and pressure ratio (PR_{TT}) will help in estimating the initial tip conditions. Through iteration one can determine the inlet and throat conditions before commencing with the impeller performance analysis by Aungier (2000). The analysis is then applied iteratively and the final result is that the required tip conditions are known.

To calculate the tip conditions, two complimentary approaches are used. In one approach, the total work input coefficient is used to determine the absolute total enthalpy at the tip ($T_{t,2}$). The other approach assumes that the process from inlet to tip is isentropic and a total pressure loss is calculated along the mean stream surface (based on the inlet conditions) to account for the actual process not being isentropic. This loss is then used to estimate the actual relative total pressure at the tip ($p'_{t,2}$) from the isentropic or ideal relative total pressure ($p'_{t,2,ideal}$). Through entropy-velocity and isentropic relations for a perfect gas, the other static conditions are calculated.

The execution sequence is explained in more detail in the following paragraphs, but the basic procedure is summarised in Figure 2.5.

The discussion will commence with details on relevant geometry and velocity triangles. For an overview of the impeller geometry in both the r-Z and r-θ planes, the reader can refer to Figure 2.6. All blade angles for the compressor stages are measured relative to the tangent.

The velocity triangle for the impeller inlet is shown in Figure 2.7. The channel flow area is defined as A_1/z_{FB} due to Aungier (2000) using the entire flow area and mass flow rate for the analysis. Equation (2.2.1) is used to determine the inlet area. Furthermore, the relative flow angle (α'_1) is not assumed to be equal to the blade angle (β_1).

$$A_1 = \pi \left(r_{1,s}^2 - r_{1,h}^2 \right) \tag{2.2.1}$$

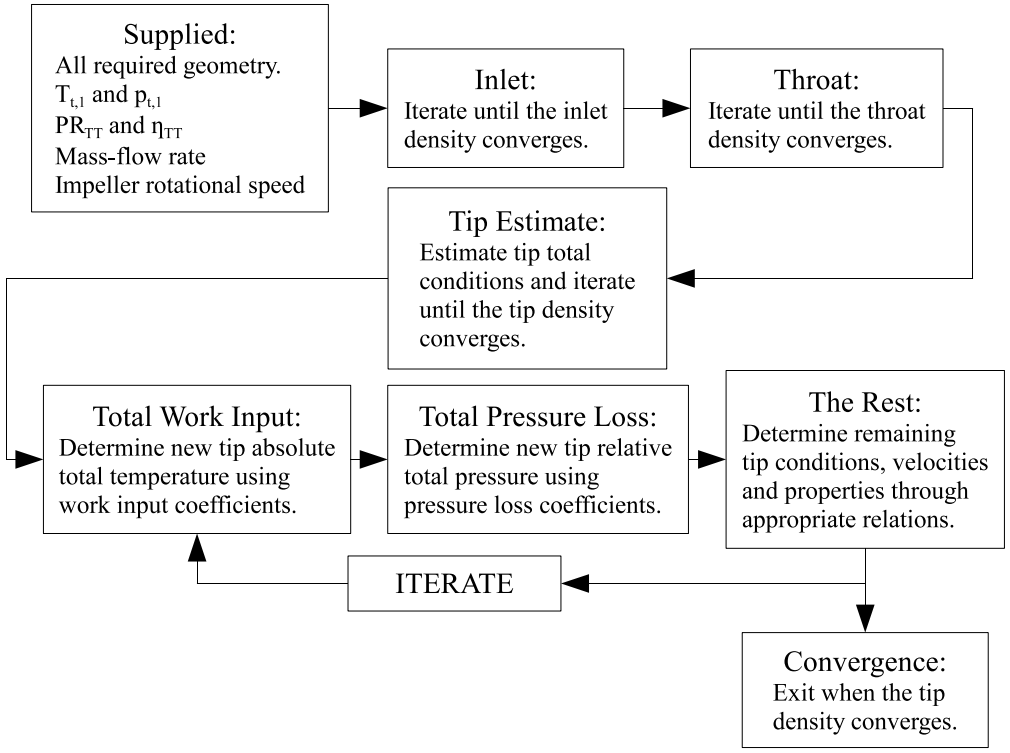

Figure 2.5: Impeller MATLAB® 1-D code execution sequence.

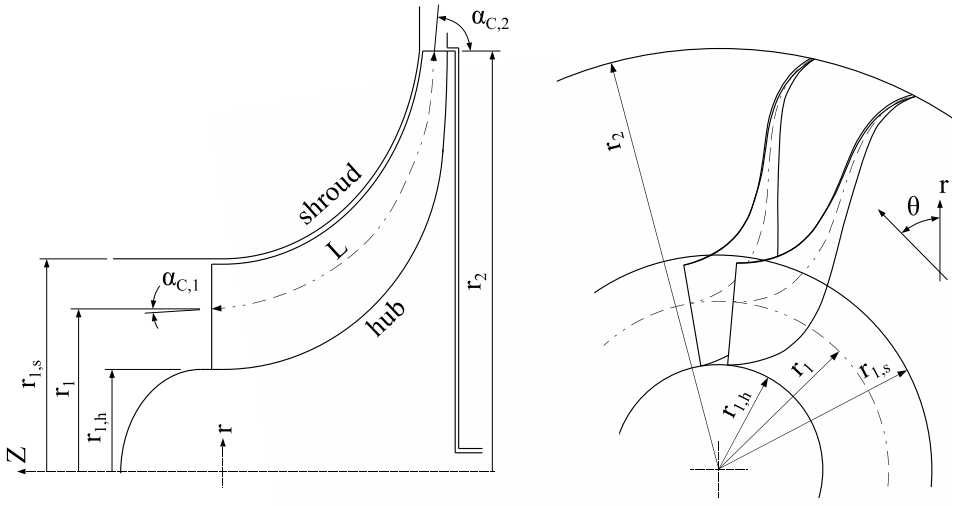

Figure 2.6: Impeller geometry in the r-Z and r-θ planes.

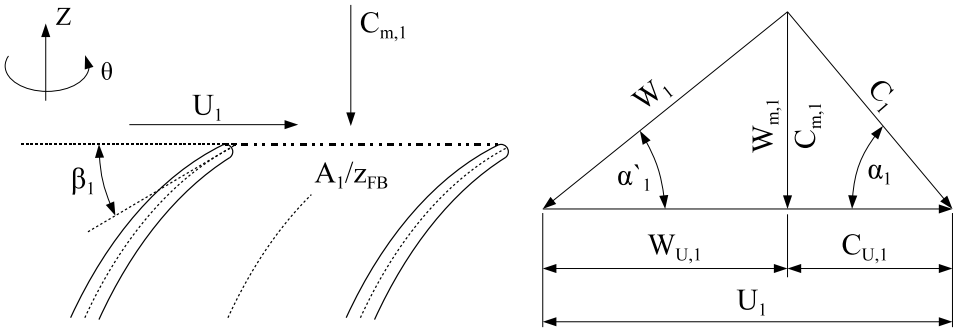

Figure 2.7: Velocity triangle of impeller inlet.

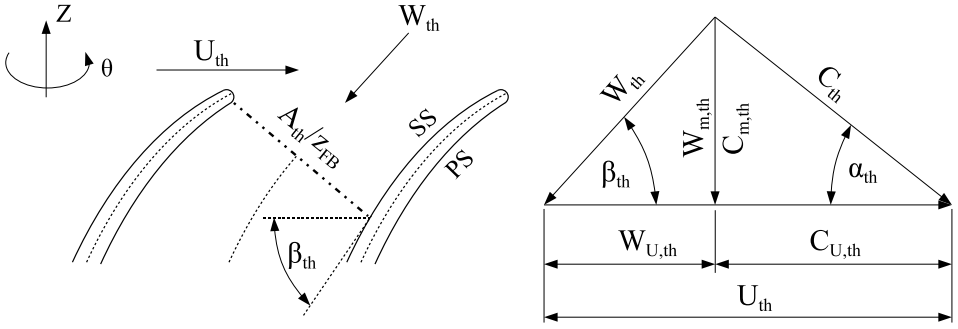

Figure 2.8: Velocity triangle of impeller throat.

Figure 2.8 shows a velocity diagram of the impeller throat. The impeller throat is per definition found at the smallest passage flow area where choking is most likely to occur and this is typically just after the inlet of the impeller. To determine the throat area (A_{th}) and wetted perimeter per channel, Aungier (2000) supplies a detailed method in Section 7.6 of his book. It must be noted that the throat blade angle (β_{th}) is found on the suction surface (SS) of the blade passage (as Aungier (2000) notes on p58) and that the relative flow angle (α'_{th}) is assumed equal to β_{th}.

Aungier (2000) simplifies the throat area to $A_1 \sin\beta_{th}$ in determining the passage area ratio (A_R) shown in Equation (2.2.2) below. This was done for two reasons, of which one is to promote better convention in the literature and avoid confusion, as Aungier (1995) points out. The other is to be able to make somewhat arbitrary adjustments to A_{th} in order to match a measured choke limit without a significant effect on the work input prediction (Aungier, 2000). During compilation of the 1-D code, it was also found that the choking loss coefficient calculation is very sensitive to the throat area.

$$A_R = \frac{A_2 \sin\beta_2}{A_1 \sin\beta_{th}} \tag{2.2.2}$$

A detailed sketch of the impeller tip is shown in Figure 2.9 and the tip flow area is determined according to Equation (2.2.3).

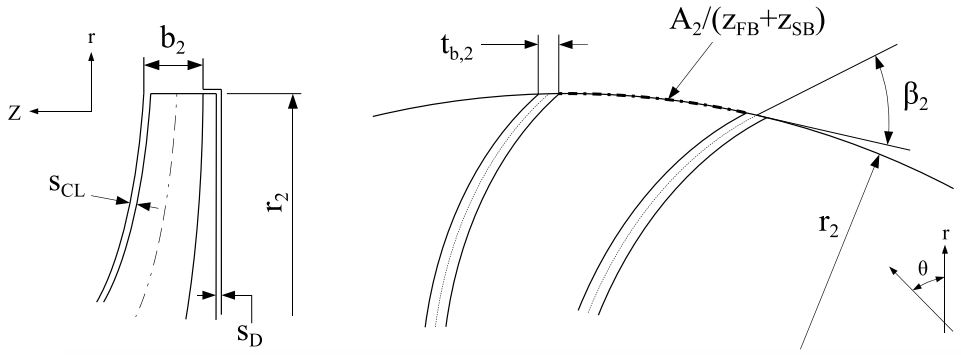

Figure 2.9: Impeller tip geometry.

$$A_2 = b_2 \left[2\pi r_2 - (z_{FB} + z_{SB})\, t_{b,2}\right] \tag{2.2.3}$$

From the area formula in Equation (2.2.3), the influence of splitter blades (SB) is noticeable. These are partial-length blades between neighbouring full blades (FB) such as found on the DEEP prototype. Aungier (2000) proposes adjusting the effective number of blades as shown in Equation (2.2.4) when splitter blades are present. Splitter blades are employed in a compressor designed for high rotational Mach numbers in which the purpose is to maintain an acceptable solidity whilst reducing blade metal blockage at the throat. This provides a larger throat area for a higher mass flow rate, thus reducing the possibility of impeller choke. Furthermore, splitter blades should ideally not extend into the throat as this will decrease the flow area. Calculation of the throat area remains the same and is calculated between two adjacent full blades and multiplied by the number of full blades.

$$z = z_{FB} + z_{SB} L_{SB} / L_{FB} \tag{2.2.4}$$

The impeller tip velocity triangle is shown in Figure 2.10. When the fluid enters the impeller, it can be considered to be irrotational. To maintain irrotational flow in the absolute frame of reference, a relative eddy rotating in the opposite direction to the impeller is required (Aungier, 2000). Due to this relative eddy, the flow will not be perfectly guided by the blades and the phenomenon of slip is observed where the outlet relative flow angle is less than the blade angle. Estimation of slip in the 1-D analysis is applied by using the approximated Busemann slip factor by Wiesner (1967).

If the total inlet thermodynamic conditions are known, the velocities and static conditions can be determined iteratively. If no pre-whirl is defined, the absolute meridional velocity ($C_{m,1}$) can be determined through the conservation of mass, as shown in general terms in Equation (2.2.5). This is after initially calculating an inlet density (ρ_1) using the total conditions and substituting A with A_1 and V with $C_{m,1}$.

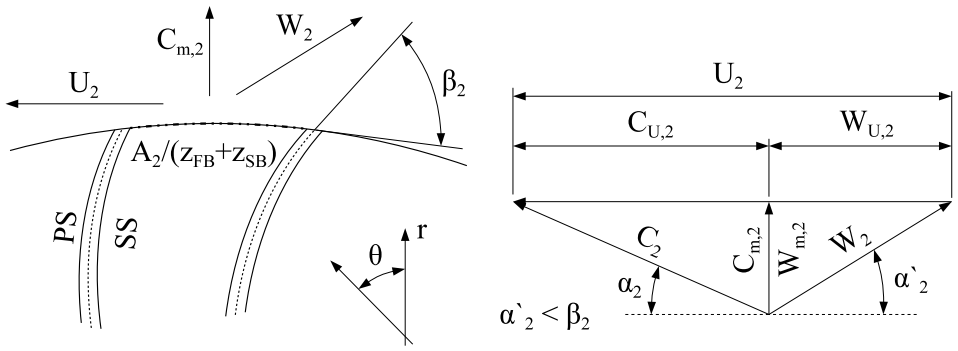

Figure 2.10: Velocity triangle of impeller tip.

$$\dot{m} = \rho V A \tag{2.2.5}$$

After this, the absolute inlet velocity (C_1) is obtained with the help of Figure 2.7. From Aungier (2000), the total enthalpy ($h_{t,1}$) is calculated using Equation (2.2.6) and is then used to determine the static enthalpy (h_1) through Equation (2.2.7). From h_1, the static temperature (T_1) is determined using Equation (2.2.6) again. A correlation for C_p is provided in Appendix A.1.

$$T_t = h_t/C_p \quad \text{and} \quad T = h/C_p \tag{2.2.6}$$

$$h = h_t - C^2/2 \tag{2.2.7}$$

The inlet static pressure (p_1) follows from the isentropic relations provided by Equation (2.2.8) (Aungier, 2000) using the total properties as reference. From the new static conditions, an iterated ρ_1 can be determined using the perfect gas equation provided in Equation (A.1.1) and the process is repeated until ρ_1 converges.

$$p = p_{ref}\left(\frac{T}{T_{ref}}\right)^{\frac{\gamma}{\gamma-1}} \tag{2.2.8}$$

Due to the impeller rotating, this analysis must be conducted in the rotating frame of reference. The rothalpy remains constant along the streamlines throughout the impeller and can be determined from Equation (2.2.9). The static thermodynamic conditions are identical in both the absolute and rotating frames of reference and it can be shown that the relative and absolute total enthalpy are related by Equation (2.2.10) (Aungier, 2000).

$$\begin{aligned} R &= h_t - \omega r C_U \\ &= h_t - U C_U \end{aligned} \tag{2.2.9}$$

$$h = h'_t - W^2/2 = h_t - C^2/2 \tag{2.2.10}$$

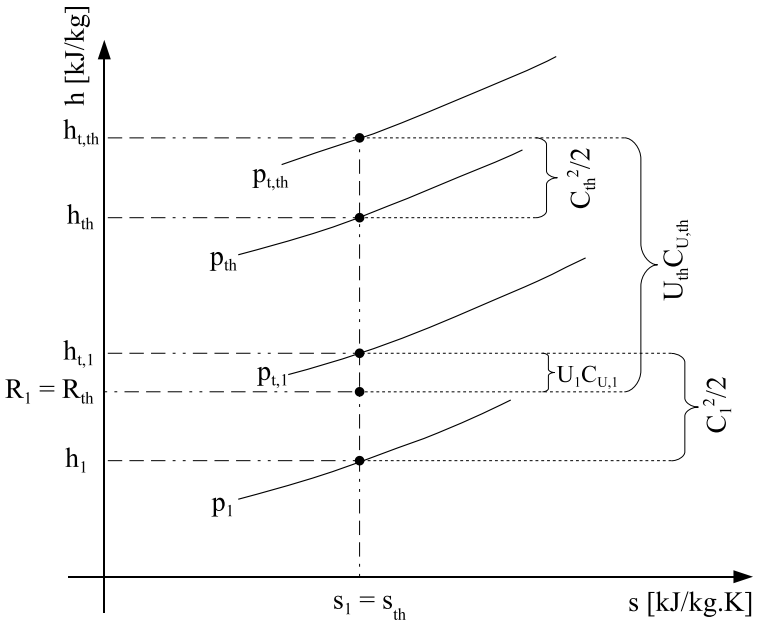

Figure 2.11: Impeller inlet to throat Mollier chart.

The impeller throat plays a vital role in the analysis to determine the onset of choking in particular. For this the throat thermodynamic state must be known and can be determined using the Mollier chart between the impeller inlet and throat in Figure 2.11 as guidance.

The process between the inlet and throat is assumed to be isentropic and no total pressure loss occurs. Only the impeller blade speed accounts for the total enthalpy rise and pressure difference. Similar to the inlet, the relative throat velocity (W_{th}) is determined iteratively using Equation (2.2.5) (by substituting V with W_{th}) whilst accounting for throat aerodynamic blockage or contraction due to the sudden change in area between the inlet and throat. This contraction ratio is defined in Equation (2.2.11) and implemented by replacing A with $A_{th}C_r$ in Equation (2.2.5).

$$C_r = \sqrt{\frac{A_1 \sin\beta_1}{A_{th}}}$$
$$C_r \leq 1 - \left(\frac{A_1 \sin\beta_1}{A_{th}} - 1\right)^2 \tag{2.2.11}$$

The throat absolute velocity (C_{th}) is then determined with the help of Figure 2.8 and the static properties can be determined using Equations (2.2.6) to (2.2.9). The iterated throat density (ρ_{th}) is calculated using the perfect gas equation (Equation (A.1.1)) and the iteration process is repeated until ρ_{th} converges.

The tip conditions have to be estimated for the first iteration. This can be done by using η_{TT} and PR_{TT} (if available) to iteratively determine the

tip air density (ρ_2) after using the total conditions to calculate an initial ρ_2 and tip specific heat ($C_{p,2}$). Similar to the inlet and throat, the absolute meridional velocity ($C_{m,2}$) can be calculated using the conservation of mass equation provided in Equation (2.2.5). The area used is A_2 as calculated in Equation (2.2.3).

The tip relative flow angle (α'_2) can initially be estimated equal to the blade angle (β_2) and from Figure 2.10 the other velocity components follow. To determine the static temperature (T_2), the absolute total enthalpy ($h_{t,2}$) must first be calculated using Equation (2.2.6) after which Equation (2.2.7) is used to determine the static enthalpy (h_2). From Equation (2.2.6) again, T_2 is calculated.

The tip static pressure (p_2) can then be determined using the isentropic relations for a perfect gas supplied in Equation (2.2.8). With an iterated p_2 and T_2, an iterated ρ_2 can be calculated using the perfect gas equation (Equation (A.1.1)) and the process repeated until ρ_2 converges. This then serves as an initial estimate of the tip conditions for the impeller analysis.

At this point of the calculation, the necessary inlet and throat properties are known and a good estimate of the tip properties has been determined. The following steps are to determine $h_{t,2}$ and $p'_{t,2}$. A summary of the following discussion regarding the impeller analysis as a whole is shown in Figure 2.12 in the form of a Mollier chart.

The total work input coefficient on the mean stream surface (I) is the impeller work expressed in dimensionless form and can be expanded as shown in Equation (2.2.12). These work coefficients respectively account for work done by the blade (I_B), windage and friction work on the impeller disk (I_{DF}), work due to leakage between the blade passages through the clearance gap (I_L) and then work done on flow recirculating back into the impeller tip (I_R). The work coefficients are discussed in Appendix B.1.

$$\begin{aligned} I &= \left(h_{t,2} - h_{t,1}\right)/U_2^2 \\ &= I_B + I_{DF} + I_L + I_R \end{aligned} \tag{2.2.12}$$

As previously mentioned, two complimentary paths are used to determine the tip conditions. The first path computes the tip temperatures. When I is known, an iterated $h_{t,2}$ can be calculate from $h_{t,1}$ using Equation (2.2.12). Using Equations (2.2.7) and (2.2.10), h_2 and $h'_{t,2}$ can be calculated. An iterated T_2 is then computed from h_2 using Equation (2.2.6).

The next complimentary path is to determine the actual $p'_{t,2}$ using the calculated total pressure loss as shown in Equation (2.2.13) (Aungier, 2000).

$$p'_{t,2} = p'_{t,2,ideal} - f_c\left(p'_{t,1} - p_1\right)\sum_i \overline{\omega}_i \tag{2.2.13}$$

The ideal relative total conditions ($p'_{t,2,ideal}$ and $T'_{t,2,ideal}$) follow from rothalpy being conserved in the rotating frame of reference. From Equations (2.2.9)

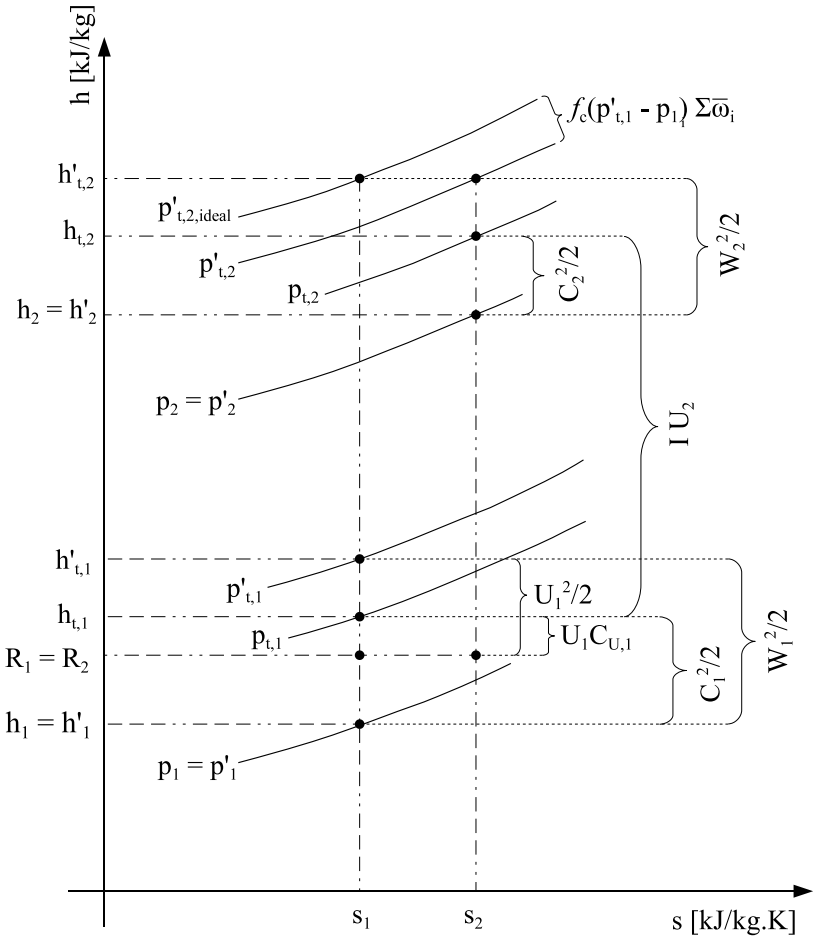

Figure 2.12: Impeller inlet to tip Mollier chart.

and (2.2.10) a definition for the relative velocities and total enthalpy at the inlet is provided in Equation (2.2.14) (Aungier, 2000).

$$\begin{aligned} h'_{t,1} &= h_{t,1} - U_1 C_{U,1} + U_1^2/2 \\ &= R_1 + U_1^2/2 \end{aligned} \tag{2.2.14}$$

Due to the rothalpy being conserved in the rotating frame of reference, the ideal relative total enthalpy at the impeller tip ($h'_{t,2,ideal}$) can be calculated from Equation (2.2.15) (Aungier, 2000), which is then assumed equal to the actual relative total enthalpy at the impeller tip ($h'_{t,2}$). With $h'_{t,2,ideal}$ known, the ideal or isentropic tip relative total conditions can be determined using Equation (2.2.8) with the inlet as reference.

$$\begin{aligned} h'_{t,2,ideal} &= h'_{t,1} + \left(U_2^2 - U_1^2\right)/2 \\ &= R_1 + U_2^2/2 \\ &= h'_{t,2} \end{aligned} \tag{2.2.15}$$

The correction factor (f_c) used in Equation (2.2.13) is defined in Equation (2.2.16). Aungier (2000) notes that without f_c, the prediction accuracy will vary with the stage pressure ratio and thus would limit the range of validity. This is only found in the impeller analysis since the total pressure loss is invariant throughout stationary components.

$$f_c = \frac{\rho'_{t,2} T'_{t,2}}{\rho'_{t,1} T'_{t,1}} \tag{2.2.16}$$

The pressure loss coefficients ($\overline{\omega}_i$) used in Equation (2.2.13) are discussed in Appendix B.1. With the sum of $\overline{\omega}_i$ known, $p'_{t,2}$ is calculated from Equation (2.2.13). From the iterated T_2 and Equation (2.2.8), an iterated p_2 and $p_{t,2}$ are calculated with the tip relative total conditions as reference.

With new values for p_2 and T_2 known, a new ρ_2 is calculated using the perfect gas equation in Equation (A.1.1). A new $C_{m,2}$ is computed using conservation of mass (Equation (2.2.5)) and the absolute tangential velocity ($C_{U,2}$) follows from Equation (2.2.17) (Aungier, 2000). The iterated velocity components and angles then follow from Figure 2.10.

$$C_{U,2} = I_B U_2 + U_1 C_{U,1}/U_2 \tag{2.2.17}$$

The impeller analysis is then repeated until ρ_2 converges, after which the analysis moves on to the vaneless annular passage.

2.2.3 Vaneless Annular Passage Performance

Examples of vaneless annular passages in centrifugal compressors are vaneless diffusers, crossover bends and inlet passages. It is also used to connect two components in the stage, such as the impeller tip and vaned diffuser inlet. The last-mentioned example is found in the centrifugal compressor studies of this thesis. The analysis procedure presented here follows from Aungier (2000), which is based on the work by Aungier (1993).

The vaneless annular passage is discretised into control volumes and the passage solved using a "marching" method. This implies that no outlet boundary conditions are required and each control volume (CV) is iterated until a convergence criterion is met before moving on to the next CV. The approach is that of a conventional 1-D analysis which includes wall friction forces, such as suggested by Johnston and Dean (1966). Figure 2.13 provides the dimensions of a CV in the vaneless annular passage. Curvature of the passage is accounted

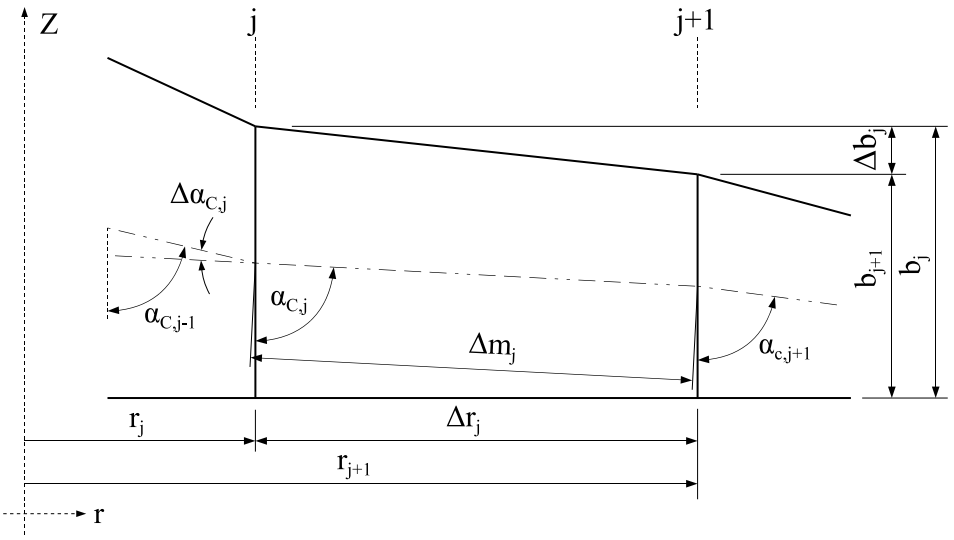

Figure 2.13: Vaneless annular passage control volume geometry.

for by using the curvature term (κ_m) defined in Equation (B.1.29) (Aungier, 2000).

The diffusion process along the passage is governed by 1.) the conservation of angular momentum and 2.) the flow area increasing due to an increase in radius (Sayers, 1990). It is assumed to be adiabatic, hence the total enthalpy remains constant, and not isentropic due to friction forces accounting for a drop in total pressure. This is summarised in Figure 2.14 in the form of a Mollier chart with the impeller tip and vaned diffuser inlet as reference.

Aungier (2000) provides Equations (2.2.18) to (2.2.20) and a repetition of Equation (2.2.7) as governing equations for 1-D flow in a vaneless annular passage which includes wall friction forces. These equations are presented in discretised form, where j is the current computing station. The last two terms of Equation (2.2.20) address losses due to flow diffusion and passage curvature respectively.

$$2\pi r_{j+1}\rho_{j+1}b_{j+1}C_{m,j+1}\left(1-B_{j+1}\right)=\dot{m} \tag{2.2.18}$$

$$b_jC_{m,j}\frac{\Delta\left(rC_U\right)_j}{\Delta m_j}=-r_jC_jC_{U,j}c_{f,j} \tag{2.2.19}$$

$$\frac{1}{\rho_j}\frac{\Delta p_j}{\Delta m_j}=\frac{C_{U,j}^2\sin\alpha_{C,j}}{r_j}-C_{m,j}\frac{\Delta C_{m,j}}{\Delta m_j}-\frac{C_jC_{m,j}c_{f,j}}{b_j}-\frac{\Delta I_{D,j}}{\Delta m_j}-I_{C,j} \tag{2.2.20}$$

An upwind differencing scheme is used where the CV inlet thermodynamic conditions are implemented to determine the density and friction coefficient. This is also the scheme used by Johnston and Dean (1966). The working fluid is again assumed to be a perfect gas.

Boundary conditions include the inlet thermodynamic conditions and velocity components as well as the boundary layer thickness. In the validation

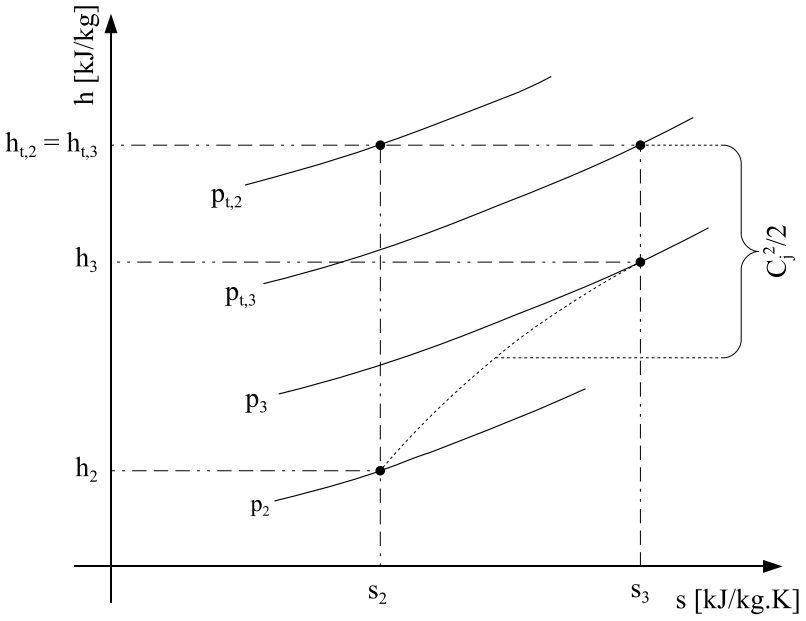

Figure 2.14: Vaneless annular passage Mollier chart.

studies these properties followed from the impeller or vaned diffuser analysis, depending on which components were being evaluated. In the event of an impeller or vaned diffuser found upstream of the analysis, the inlet boundary layer thickness (δ_2 keeping with the convention in Figure 2.14) can be calculated using the simple flat plate theory provided in Equation (A.4.1). Averages of the impeller inlet and tip or vaned diffuser inlet and discharge are used to determine δ_2. Aungier (2000) provides further empirical equations to determine δ_2 for other implementations of the analysis.

Aungier (2000) models diffusion losses using diffuser analogies by Reneau *et al.* (1967). This analogy identifies a low loss regime when the divergence parameter, D_j, is less than a certain value, $D_{m,j}$. The analogies of D_j and $D_{m,j}$ implemented by Aungier (2000) are provided in Equations (2.2.21) and (2.2.22).

$$D_j = -\frac{b_j}{C_j}\frac{\Delta C_j}{\Delta m_j} \tag{2.2.21}$$

$$D_{m,j} = 0.4\,(b_2/L_{2,3})^{0.35}\sin\alpha_j \tag{2.2.22}$$

Aungier (2000) notes that the flow angle term in Equation (2.2.22) is an empirical factor derived from comparisons of more than 35 compressor stage tests. An empirical diffusion efficiency model was formulated from this same comparison and is provided in Equation (2.2.23).

$$\begin{aligned} E_j &= 1 && \text{if} \quad D_j \leq 0 \\ E_j &= 1 - 0.2\left(D_j/D_{m,j}\right)^2 && \text{if} \quad 0 < D_j < D_{m,j} \\ E_j &= 0.8\sqrt{D_{m,j}/D_j} && \text{if} \quad D_j \geq D_{m,j} \end{aligned} \tag{2.2.23}$$

The streamwise diffusion loss term implemented by Aungier (2000) is then provided in Equation (2.2.24).

$$\frac{\Delta I_{D,j}}{\Delta m_j} = -2\left(p_{t,j} - p_j\right)\left(1 - E_j\right)\frac{1}{\rho_j C_j}\frac{\Delta C_j}{\Delta m_j} \tag{2.2.24}$$

In addition to this term, higher losses can be caused by an excessive meridional gradient of the passage area. To check for this situation, a diffuser analogy is again used at each computing station and Aungier (2000) estimates the maximum, stall-free, local area by using Equation (2.2.25). The equation is relative to the vaneless annular passage inlet, the impeller tip (station 2) in this example.

$$\left(rb\right)_{m,j} = \left(rb\right)_2\left[1 + 0.16 m_j/b_2\right] \tag{2.2.25}$$

This is the equivalent of a diffuser divergence angle ($2\theta_C$) of 9° and if the local area exceeds this value, a second estimate of the diffusion loss term is determined by Equation (2.2.26) (Aungier, 2000).

$$I_{D,j} = 0.65\left(p_{t,j} - p_j\right)\left[1 - \left(rb\right)_{m,j}/\left(rb\right)_j\right]/\rho_j \tag{2.2.26}$$

If the value obtained by Equation (2.2.26) exceeds the value obtained by integrating Equation (2.2.20), it replaces the last-mentioned discretised value. To implement this in dicretised form at a specific computing station, the values obtained from Equation (2.2.24) of all the preceding and current control volumes are summed to $\sum_j \Delta I_{D,j}$. If the value from Equation (2.2.26) exceeds $\sum_j \Delta I_{D,j}$, a new value for $\Delta I_{D,j}$ is determined using Equation (2.2.27), which then replaces the current CV value.

$$\Delta I_{D,j} = I_{D,j} - \sum_j \Delta I_{D,j} \tag{2.2.27}$$

To account for losses due to passage curvature, Aungier (2000) provides Equation (2.2.28). This equation was also empiricaly developed from comparisons of 35 different compressor stage tests. Aungier (2000) mentions that it has negligable effect on vaneless diffusor performance but is always significant for crossover bends, if not sometimes dominant.

$$I_{C,j} = \kappa_{m,j}\left(p_{t,j} - p_j\right)C_{m,j}/\left(13\rho_j C_j\right) \tag{2.2.28}$$

The boundary layer thickness (δ_j) will influence the meridional velocity in the passage ($C_{m,j}$) and an area blockage factor (B_j) is used to determine its effect. Aungier (2000) proposes the use of a simple boundary layer growth model based on the $1/7^{\text{th}}$ power law for the boundary layer velocity profiles to determine B_j and the skin friction coefficient ($c_{f,j}$). The power law is shown in Equation (2.2.29) where the subscript e designates a value at the boundary layer edge.

$$\begin{aligned} C_{m,j} &= C_{m,e,j}\left(y/\delta_j\right)^{1/7} \\ C_{U,j} &= C_{U,e,j}\left(y/\delta_j\right)^{1/7} \end{aligned} \tag{2.2.29}$$

If δ_j is known and both layers are identical, integrating accross the passage using conservation of mass flow yields an expression for B_j as a function of $2\delta_j/b_j$ as shown in Equation (2.2.30) (Aungier, 2000).

$$\begin{aligned} \int_0^b \rho_j C_{m,j} dy &= \rho_j b_j C_{m,e,j}\left(1 - B_j\right) \\ B_j &= 2\delta_j/\left(8b_j\right) \end{aligned} \tag{2.2.30}$$

When applying this integration approach for angular momentum flux, the result in Equation (2.2.31) is found by Aungier (2000). This will determine an average angular momentum flux.

$$\int_0^b r_j \rho_j C_{m,j} C_{U,j} dy = r_j \rho_j b_j C_{m,e,j} C_{U,e,j}\left[1 - 2\delta_j/\left(4.5b_j\right)\right] \tag{2.2.31}$$

Noting that Equation (2.2.30) includes B_j, one can use it to determine $C_{m,e,j}$. Through Equations (2.2.30) and (2.2.31) it can be shown that the predicted angular momentum and the boundary layer edge value are related by Equation (2.2.32) (Aungier, 2000).

$$\left(rC_U\right)_j = \left(rC_{U,e}\right)_j\left[1 - 2\delta_j/\left(4.5b_j\right)\right] \tag{2.2.32}$$

If δ_2 is known, Equation (2.2.32) can be used to determine $C_{U,e,2}$ from $\left(rC_U\right)_2$ and r_2. From $C_{U,e,2}$ and r_2, $\left(rC_{U,e}\right)_2$ is computed which is conserved until the boundary layer fills the passage, i.e. when $2\delta_j = b_j$.

As the anlysis progresses along the passage, a new locally predicted $\left(rC_U\right)_{j+1}$ can be determined using Equation (2.2.19). With this $\left(rC_U\right)_{j+1}$ and the known $\left(rC_{U,e}\right)_2$, Equation (2.2.32) is used to compute the CV exit boundary layer thickness (δ_{j+1}) and blockage factor (B_{j+1}). Hence, if δ_2 is known, Equations (2.2.30) and (2.2.32) provide a means for computing the boundary layer growth through yielding local values δ_{j+1} and B_{j+1}.

Aungier (2000) notes that a high degree of accuracy for δ_2 is not required and that the previously mentioned simple flat plate boundary layer thickness estimate provided in Equation (A.4.1) is sufficient. The influence of δ_j is primarily on the local friction factor ($c_{f,j}$) which is computed using the pipe friction model described in Appendix A.3 with the pipe diameter replaced by $2\delta_j$. The effect is most noticeable when $2\delta_j/b_j$ is rather small, as found in compressors with very high flow coefficients (Aungier, 2000).

$C_{m,j+1}$ is calculated using the known value for B_{j+1} and Equation (2.2.18). Implementing the mentioned relations, the CV outlet static pressure (p_{j+1}) is determined using Equation (2.2.20). The static temperature (T_{j+1}) follows from the enthalpy-velocity relations supplied in Equation (2.2.6) and (2.2.7). From this a new CV outlet density (ρ_{j+1}) is calculated using the perfect gas equation supplied in Appendix A.1. The process is then repeated until ρ_{j+1} converges before moving onto the next CV.

2.2.4 Vaned Diffuser Performance

The vaned diffuser performance analysis by Aungier (2000) is similar in concept to the impeller analysis. Originally the 1-D analysis was for conventional thin-vaned or airfoil style vaned diffusers (Aungier, 1990), but a modified form by Aungier (2000) is presented in this thesis. The analysis has been generalised for application on vaned diffusers with non-parallel end walls and thick vanes. Even though the generalisation is simple in approach, Aungier (2000) emphasises that the analysis procedure has only been validated against experiments of thin-vaned and parallel-walled diffusers, but reasonable results have been obtained during occasional use for vane-island diffusers.

Two vaned diffusers were investigated in this thesis, one is found in the Radiver test case and the other in the DEEP prototype. The Radiver has a wedge-type vaned diffuser and thus the analysis procedure by Aungier (2000) has not been verified for this type of geometry. The DEEP prototype's vaned diffuser implements a Concepts ETI™ patented flat plate profile and is thus ideal for analysis by the presented analysis procedure. To agree with the terminology used in this thesis, the geometry presented in Figure 2.15 is for a wedge-type vaned diffuser.

As with the impeller performance analysis, flow calculations are performed along a mean stream surface at the vaned diffuser inlet, throat and discharge. The inlet thermodynamic conditions, mass flow rate and velocity components are supplied by a performance analysis upstream of the vaned diffuser. All of the required geometry is supplied and the working fluid is again assumed to be a perfect gas. No energy addition is performed due to the absence of rotating blades and the process is assumed to be adiabatic, hence the total enthalpy remains constant throughout the vaned diffuser.

Solving the discharge conditions is an iterative process where loss coefficients are determined along the mean stream surface. The loss coefficients

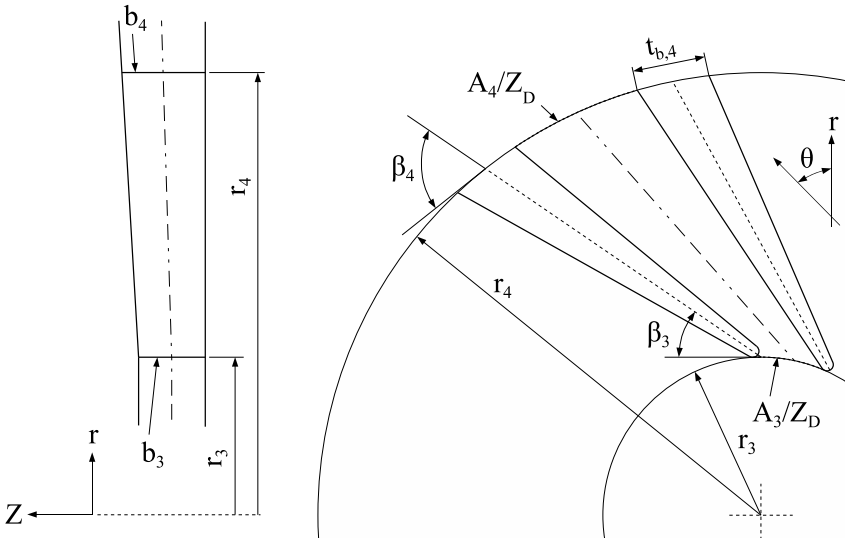

Figure 2.15: Vaned diffuser geometry in the r-Z and r-θ planes.

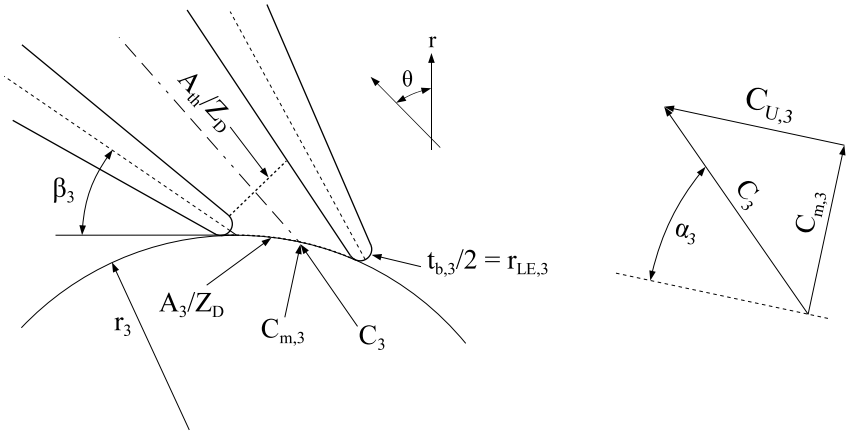

Figure 2.16: Vaned diffuser inlet and throat geometry and velocity triangle.

are summed and then used to determine the discharge total pressure from the inlet total and static pressure. An isentropic process is assumed between the inlet and throat and thus the throat static thermodynamic properties and absolute velocity can be determined iteratively, similar to the impeller, before proceeding with the performance analysis.

The vaned diffuser inlet and throat geometry and inlet velocity triangle is shown in Figure 2.16. Due to the inlet conditions being dependent on the mass flow rate and impeller speed, the inlet flow angle will not necessarily coincide with the vaned diffuser inlet blade angle. The inlet area (A_3) is calculated using Equation (2.2.33).

$$A_3 = 2\pi r_3 b_3 \tag{2.2.33}$$

By assuming that the progression from inlet to throat is isentropic and that the overall process is adiabatic, the throat total pressure is equal to that of the inlet. Thus the total conditions for the inlet and throat are the same. To iteratively solve the throat static conditions and absolute velocity, the throat density (ρ_{th}) is initially assumed identical to the inlet value. The throat absolute velocity (C_{th}) is determined using conservation of mass, as shown in Equation (2.2.5) by substituting V with C_{th}.

The sudden change in flow area is again accounted for as found in the impeller analysis by using a contraction ratio, shown in Equation (2.2.34) (Aungier, 2000). This contraction ratio is implemented by correcting A to $C_r A_{th}$ in Equation (2.2.5). To determine the throat area (A_{th}), the same detailed method provided by Aungier (2000) in Section 7.6 of his book is implemented.

$$C_r = \sqrt{\frac{A_3 \sin \beta_3}{A_{th}}}$$
$$C_r \leq 1 - \left(\frac{A_3 \sin \beta_3}{A_{th}} - 1 \right)^2 \tag{2.2.34}$$

With the constant throat total enthalpy ($h_{t,th}$) and iterated C_{th} known, the static temperature (T_{th}) is determined using Equations (2.2.6) and (2.2.7). Using the isentropic relation in Equation (2.2.8) with the total throat conditions as reference, the throat static pressure (p_{th}) is determined. From the perfect gas equation in Appendix A.1, an iterated ρ_{th} is calculated. The process is then repeated until ρ_{th} converges before moving on to the performance analysis.

The vaned diffuser discharge geometry and velocity diagram is shown in Figure 2.17. The discharge area (A_4) is determined similar to the impeller's tip area and the implemented definition is shown in Equation (2.2.35). As can be seen, thick vanes at the discharge can have a noticeable effect on the value of A_4.

$$A_4 = 2\pi r_4 b_4 - z_D t_{b,4} b_4 \tag{2.2.35}$$

The static discharge conditions need to be determined iteratively and for the first iteration, the static temperature and pressure must be estimated to determine an initial discharge density. The discharge total enthalpy ($h_{t,4}$) remains constant and the total pressure is determined using Equation (2.2.36) (Aungier, 2000). The discharge absolute meridional velocity ($C_{m,4}$) is calculated from conservation of mass using Equation (2.2.5) with $C_{m,4}$ instead of V and A_4 as the area.

$$p_{t,4} = p_{t,3} - (p_{t,3} - p_3) \sum_i \overline{\omega}_i \tag{2.2.36}$$

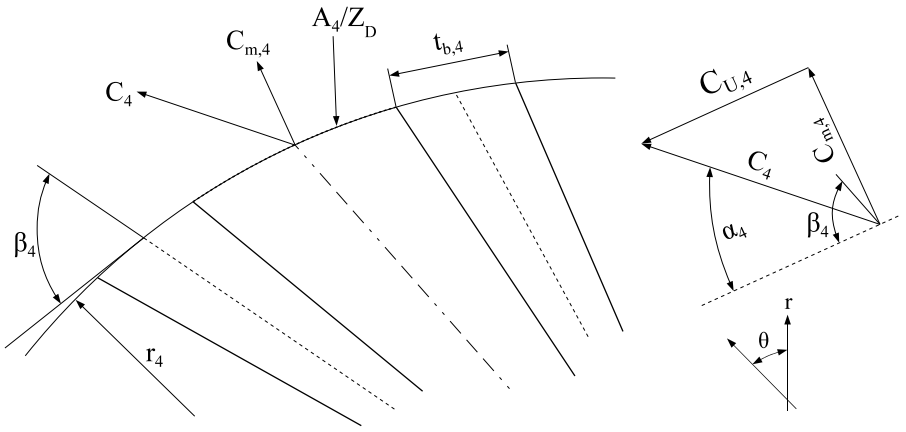

Figure 2.17: Vaned diffuser tip geometry.

The discharge flow angle (α_4) is determined using axial-flow compressor correlations which Aungier (2000) transformed to the radial plane. The definition is supplied in Equation (2.2.37).

$$\alpha_4 = \beta_4 - \delta^* - \frac{\partial \delta}{\partial i}(\beta_3 - \alpha_3) \tag{2.2.37}$$

With α_4 known, the absolute discharge velocity (C_4) follows from Figure 2.17. Using the relations in Equations (2.2.6) and (2.2.7), the discharge static temperature (T_4) is determined. Using the isentropic relation from Equation (2.2.8), the discharge static pressure (p_4) is calculated with the discharge total properties as reference. From the perfect gas equation provided in Equation (A.1.1), the iterated value of ρ_4 is determined. The process is then repeated until $C_{m,4}$ converges.

To summarise the above discussion, the vaned diffuser Mollier chart is supplied in Figure 2.18. The required loss coefficients and variables for Equations (2.2.36) and (2.2.37) are provided in Appendix B.2.

2.3 CFD Modelling using FINE™/Turbo

To support the 1-D model, the thesis included the use of 3-D Computational Fluid Dynamic (CFD) software. CFD software packages typically divide the computational environment into three distinctive programs:

- The pre-processor program where the operating fluid volume around the physical geometry of the model (also known as the "domain") is divided up into finite volumes (also known as "meshed").
- The solver program where the solving algorithm is configured to solve the set of discretised equations of the selected flow field and turbulence

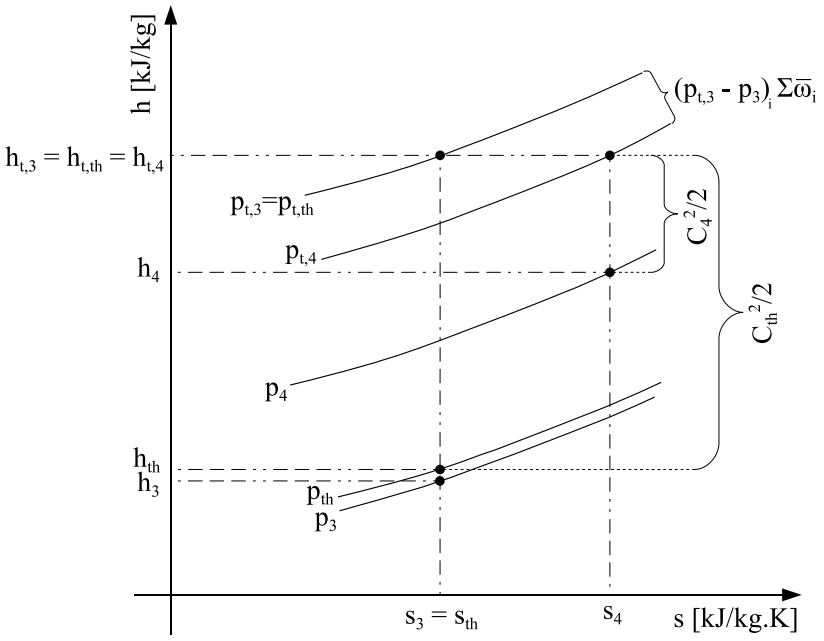

Figure 2.18: Vaned diffuser Mollier chart.

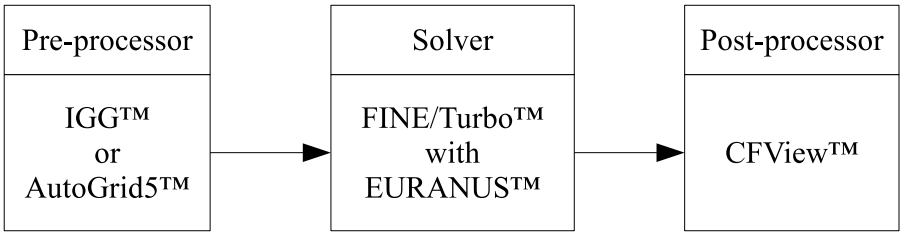

Figure 2.19: The FINE™/Turbo environment.

model (an approximation of the Reynolds stresses in the Navier-Stokes equation) with boundary conditions.

- The post-processor program where the solved flow domain's results are evaluated and presented.

The FINE™/Turbo commercial CFD package from NUMECA International (Intl.) was used. The package is primarily aimed at automating the meshing, solving and post-processing of turbomachinery applications in a CFD environment, as Figure 2.19 shows.

During solving, the program Monitor™ can be used to monitor the residual error of the properties relevant to the model and in doing so the user can determine whether numerical convergence has been achieved. The package can be extended to include Design3D™ with AutoBlade™ for 3-D turbomachinery geometry design and generation. Two versions of FINE™/Turbo were used during the thesis, v8.4-3 and v8.7-2.

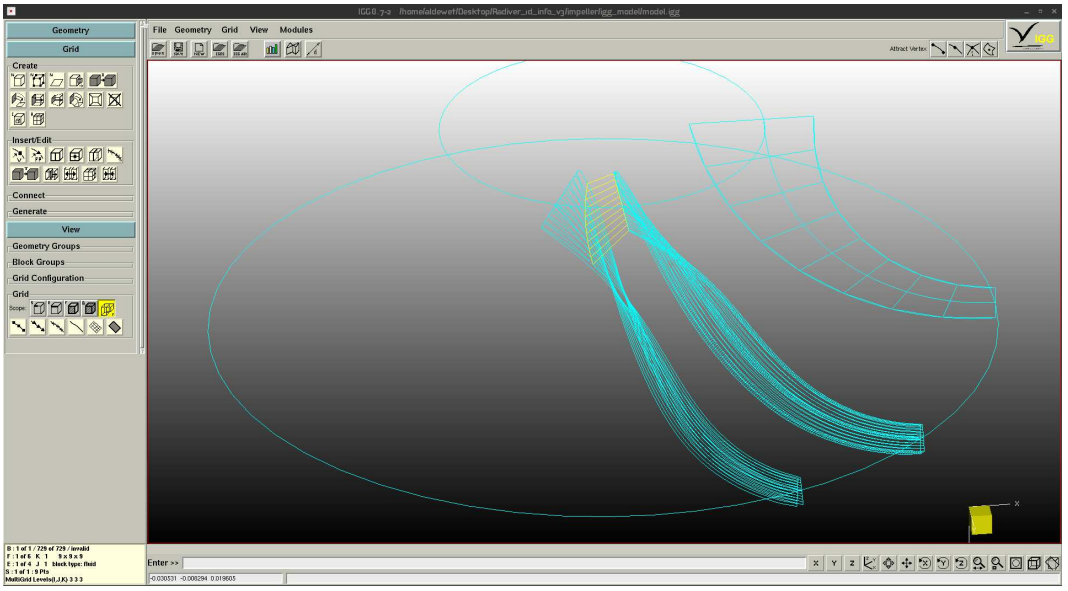

Figure 2.20: Screenshot of IGG™.

2.3.1 Overview of the CFD Environment

This section is an overview of the capabilities of the software package.

IGG™ (**I**nteractive **G**rid **G**enerator) is a general meshing utility, rendering structured hexahedral grids with multiple blocks around 2-D and 3-D geometries using an advanced graphical user interface (GUI). The program is supported by interactive 3-D geometry generation capabilities, which proved useful when obtaining 1-D geometry information of the thesis compressors for use in the 1-D theory of Aungier (2000). The resulting mesh is contained in the CGNS format for use by FINE™/Turbo. A screenshot of IGG™ is provided in Figure 2.20, which shows part of the process of obtaining the Radiver test case 1-D geometry with the throat indicated in yellow.

AutoGrid5™ (**Auto**mated **Grid** Generator for Turbomachinery) is designed for automatic meshing of centrifugal and axial turbomachinery components to produce high quality, complex, structured hexahedral grids. An older variant of the program, AutoGrid4™, is still being maintained. Amongst AutoGrid5™'s features are facilities for splitter blades, hub and shroud clearance gaps and blade fillet radii. Geometry can be supplied in the *.geomTurbo* format or imported using specific computer model formats such as the IGES format. Three blade meshing topologies are available to generate grids for turbomachinery components, namely the default (O4H), HOH and H&I topologies. The O4H topology is aimed at fully automatic meshing for all kinds of turbomachinery, whilst the HOH and H&I topologies produce high quality grids but are not suitable for all applications (AutoGrid5™ Manual, 2010). To minimise the mesh size and reduce computation time, a single blade passage is meshed and rotational periodic boundary conditions are imposed by AutoGrid5™ by

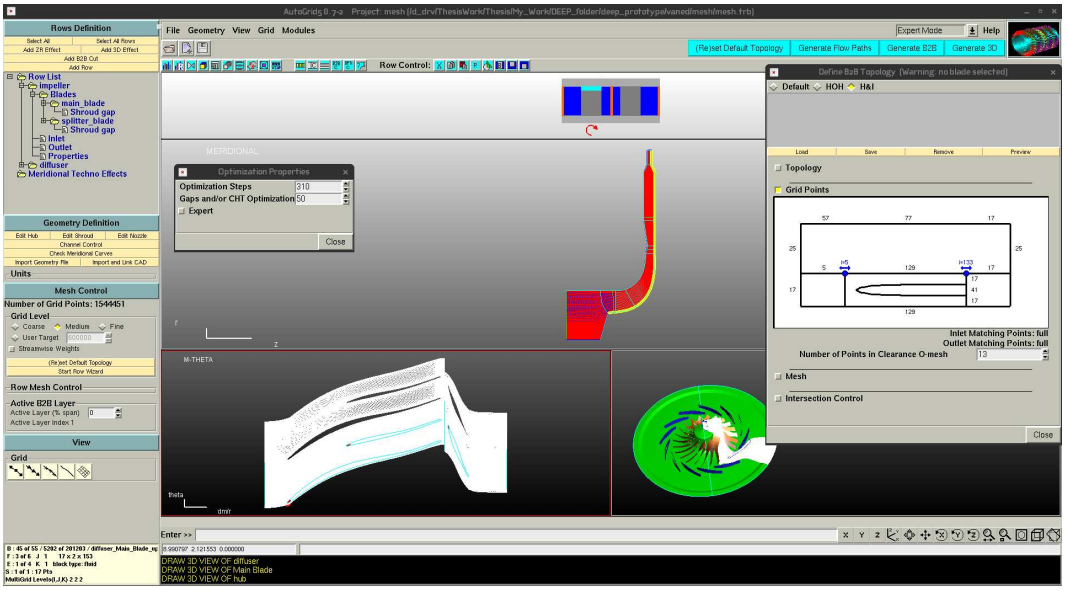

Figure 2.21: Screenshot of AutoGrid5™.

default. The number of rotational periodic meshes can be increased to obtain a full compressor mesh. The resulting mesh is also contained in the CGNS format. A screenshot of AutoGrid5™ is supplied in Figure 2.21, showing part of the meshing procedure of the DEEP prototype.

FINE™/Turbo (**Flow Integrated Environment**) serves as 1.) a GUI for setup of the NUMECA Intl. solver, EURANUS™ and 2.) a project management utility for different solver setups. EURANUS™ is tailored to accommodate rotating components in both steady and unsteady flow models. A project can be defined in FINE™/Turbo, which is coupled to a specific IGG™ or AutoGrid5™ CGNS model. Multiple computations can then be defined within the project to facilitate different solver setups with the same geometry. To illustrate this, a screenshot of the project used for the Eckardt O-Rotor with a linear shroud is shown in Figure 2.22.

CFView™ (**C**omputational **F**ield **V**isualization system) is designed to visually evaluate the flow properties of the solved discretised domain, supporting both structured and unstructured grids. Outputs of the program are extensive, with representations of local values, scalar plots, vector plots and streamlines to name a few. Features include terminology relevant to turbomachinery analysis. A screenshot of the relative velocity magnitude in the impeller and absolute velocity magnitude in the diffuser of the DEEP prototype at 50% span is shown in Figure 2.23.

2.3.2 Turbulence Models

Three mathematical models are available in FINE™/Turbo to model the flow state in the discretised domain (FINE™/Turbo Manual, 2010):

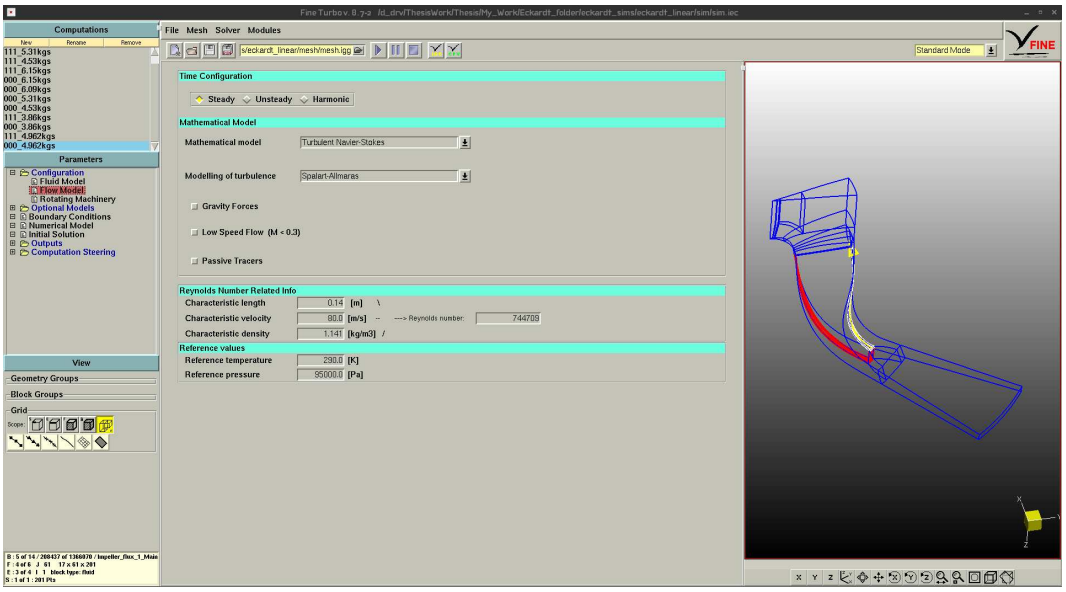

Figure 2.22: Screenshot of FINE™/Turbo.

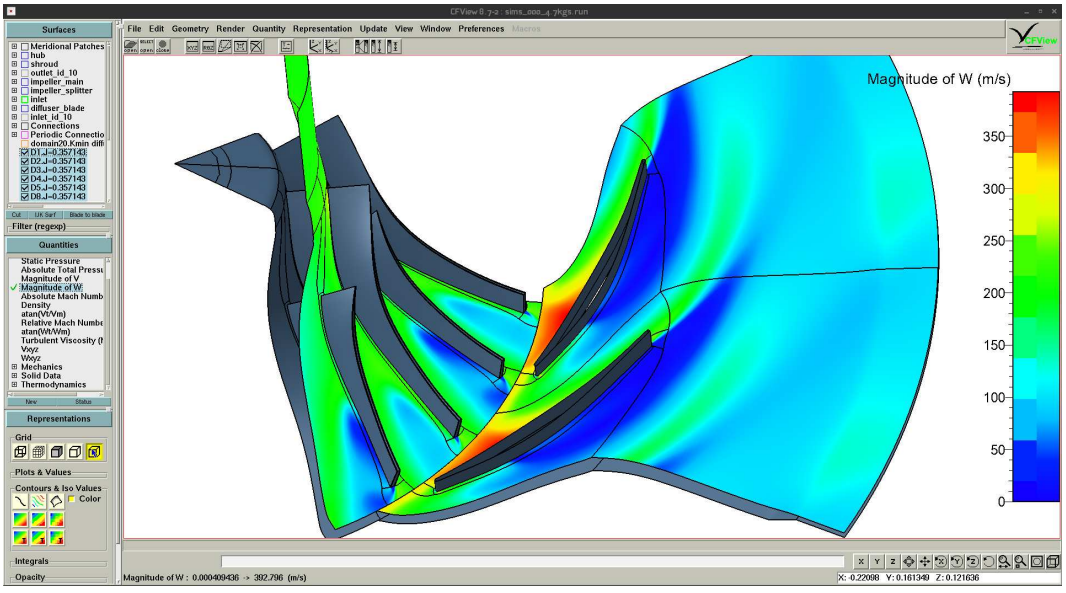

Figure 2.23: Screenshot of CFView™.

- The Euler model, which performs an inviscid calculation where all of the solid walls are considered to be zero shear walls and the non-zero velocity is tangential to the wall. This is due to the assumption that fluid slip occurs at the wall boundary.
- The Laminar Navier-Stokes equation, which only affects the thermodynamic properties of the fluid and does not contain a turbulent eddy viscosity model. Thus the laminar kinematic viscosity is used.
- The Turbulent Navier-Stokes equation, of which a turbulence model has to be chosen to determine the Reynolds stresses in the Navier-Stokes equation.

Several turbulence models are available for use (FINE™/Turbo Theoretical Manual, 2010), i.e. the algebraic model by Baldwin and Lomax (1978), the 1-equation model by Spalart and Allmaras (1992), a total of six 2-equation models and also a 4-equation model using a code-friendly variant of the v^2-f model described by Lien and Kalitzen (2001).

Four of the 2-equation models are variants of the k-ϵ model, namely the:

- Low Reynolds number k-ϵ model by Chien (1982).
- Standard high Reynolds number k-ϵ model by Launder and Spalding (1974) with extended wall functions.
- Low Reynolds number k-ϵ model by Launder and Sharma (1974).
- Low Reynolds number k-ϵ model by Yang and Shih (1993).

The other two 2-equation models are variants of the k-ω model, of which one is the standard variant by Wilcox (1988) and Wilcox (1993). The other model addresses the sensitivity to the small free stream value of ω of the original model by implementing a Shear Stress Transport (SST) model proposed by Menter (1994), namely the k-ω SST model.

To determine how well the turbulence model approximates the boundary layer properties at solid surfaces, the y^+ parameter can by computed by FINE™/Turbo. This y^+ parameter is defined in Equation (2.3.1) and the accompanying friction velocity (v^*) in Equation (2.3.2) (FINE™/Turbo Manual, 2010).

$$y^+ = \frac{\rho v^* y_{wall}}{\mu} \tag{2.3.1}$$

$$v^* = \sqrt{1/2 V_{ref}^2 c_f} \tag{2.3.2}$$

y^+ values provide a measure of how well the specific turbulence model predicts the gradients in the boundary layer, specifically the viscous sub-layer.

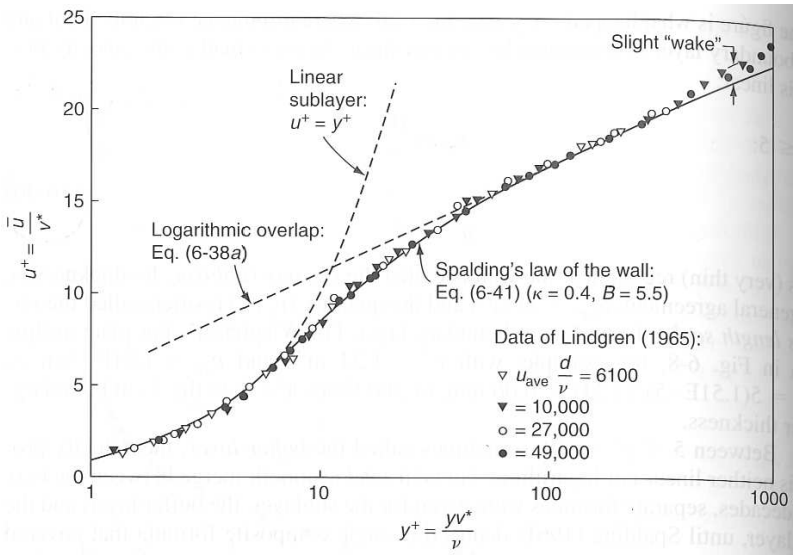

Figure 2.24: Approximation of the boundary layer profiles (White, 2006).

The viscous sub-layer is where $y^+ \leq 5$ in Figure 2.24 (White, 2006), but the acceptable range of y^+ values depends on the turbulence model used.

To actively influence the y^+ value, the size of the first CV at the solid wall surface (y_{wall}) can be changed as seen in Equation (2.3.1). Thus it is advisable to evaluate the y^+ values on all of the surfaces after a computation to determine if the grid is sufficiently defined at the solid wall. The medium velocity also influences the y^+ value, with an increase in velocity resulting in an increase in y^+ value. Thus when evaluating the y^+ value for a specific mesh and range of mass flow rates, the highest mass flow rate must be investigated. Adjustments to the wall cell height can then be made accordingly.

Two turbulence models were investigated, namely the 1-equation model by Spalart and Allmaras (1992) (subsequently referenced as "S-A") and the standard k-ϵ with extended wall function model by Launder and Spalding (1974) (subsequently referenced as "k-ϵ"). This was done to justify the decision on using a single turbulence model during the rest of the thesis. The models were applied to identical meshes of the Eckardt O-Rotor (with a hyperbolic shroud) and the computation performance and accuracy was observed.

NUMECA Intl. documentation (FINE™/Turbo Manual, 2010) suggests an acceptable y^+ value range for both the S-A and k-ϵ models of $1 \leq y^+ \leq 10$. The default INEWKE expert parameter of 10 has to be chosen during the EURANUS™ solver setup for the k-ϵ model. This is to enable a mesh independent formulation of the wall functions, which results in an acceptable y^+ value range of $1 \leq y^+ \leq 10$ for the k-ϵ model (FINE™/Turbo Manual, 2010). Some overshoot can be expected on surfaces where a high degree of separation is possible, such as the impeller tip.

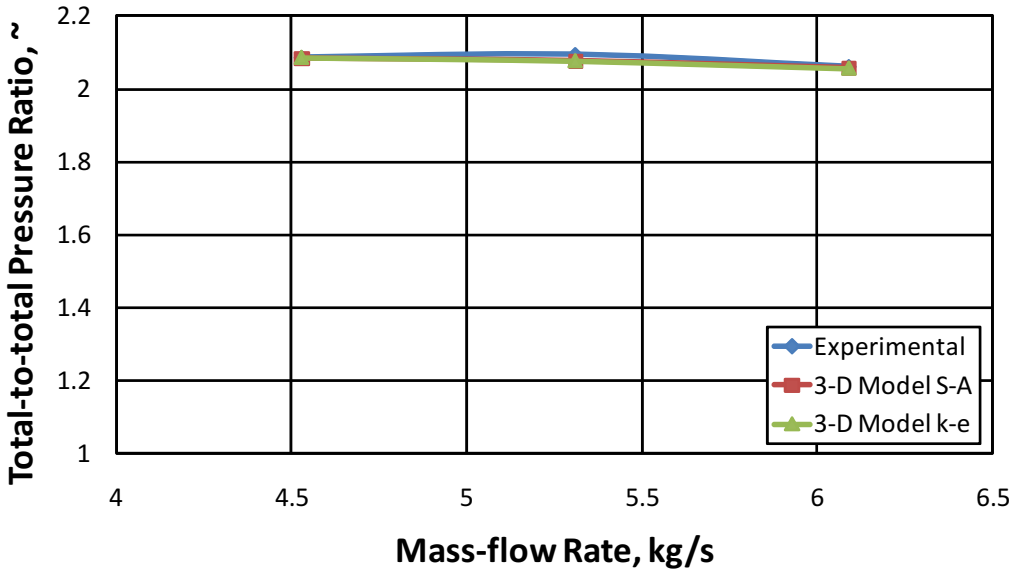

Figure 2.25: Total-to-total pressure ratio of the Eckardt O-Rotor using different turbulence models.

Satisfactory convergence using the k-ϵ model was achieved after roughly 28.5 h and 5600 iterations. For the S-A model, convergence was achieved after roughly 14 h and 5590 iterations, hence, solving the domain faster. The k-ϵ model also showed roughly twice the memory usage of the S-A model during computation. The two remaining test mass flow rates of the Eckardt O-Rotor were then solved by both turbulence models. As shown in Appendix E, the single mesh provided satisfactory y^+ values for both turbulence models.

A comparison of the mass flow rate and total-to-total pressure ratio results are shown in Figure 2.25. The mass flow rate versus total-to-total efficiency results are shown in Figure 2.26.

Similar differences in convergence times and memory usage were observed for the higher and lower mass flow rates. From Figures 2.25 and 2.26, the reader can observe that the difference in results of both models are minimal. Comparisons of in-depth flow-field solutions were not performed as overall performance and basic flow indications were the primary objective.

Due to the good accuracy, quicker solving time and reduced memory requirements of the Spalart-Allmaras model, the author chose to use it for the remainder of the thesis. Taking the recommended range of y^+ values for the S-A model into account, the author aimed to achieve y^+ values of less than six for the thesis compressors.

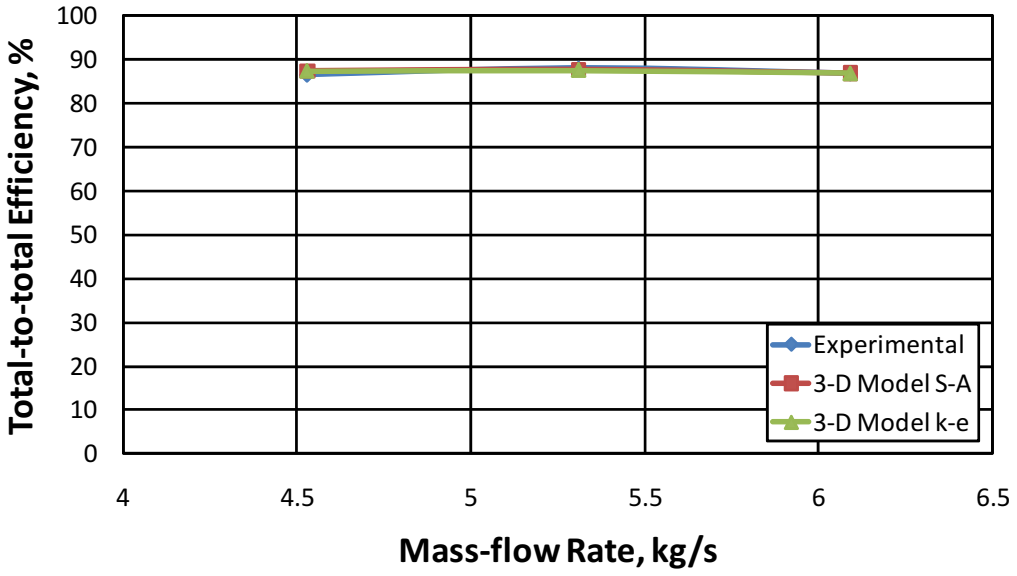

Figure 2.26: Total-to-total efficiency of the Eckardt O-Rotor using different turbulence models.

2.3.3 Mesh Quality and Grid Convergence

AutoGrid5™ includes parameters to assess the quality of the grid during blade-to-blade (B2B) generation at the current hub-to-shroud streamline, hence in a 2-D plane. The same quality parameters are available once the 3-D mesh has been generated. Three parameters were identified to be sufficiently indicative of the mesh quality, namely the orthogonality, aspect ratio and expansion ratio.

The orthogonality is defined by the smallest angle between edges in the control volume (CV), thus the smaller the angle, the sharper the corner of the CV and the lower the quality of the grid. The aspect ratio is defined by the fraction of the longest average of opposing edges over the shortest average of opposing edges of the CV. This is illustrated in Figure 2.27 (AutoGrid5™ Manual, 2010). Thus, a higher aspect ratio indicates a longer, narrower CV, which is undesired.

The expansion ratio involves two adjacent CVs in 3-D. It is a measure of the size variation between the two CVs and is direction dependent. This definition is illustrated in Figure 2.28 (AutoGrid5™ Manual, 2010). Lower values are preferred, as this implies a steady "growth" of the CVs in the particular direction.

The author attempted to achieve a grid orthogonality higher than 34° at the hub, with 24° considered acceptable at the shroud. Aspect ratios lower than 2200 and expansion ratios lower than 2.2 were the objective. If the mentioned objectives could not be met, the number of CVs over or under the respective objective were minimised as best possible. This resulted in high quality meshes

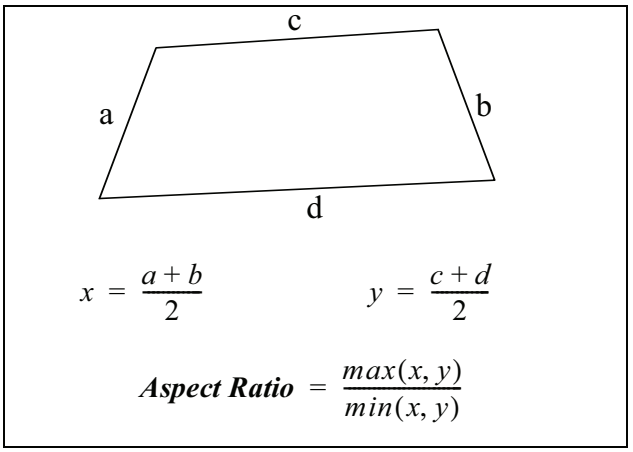

Figure 2.27: Aspect ratio definition of the control volume (AutoGrid5™ Manual, 2010).

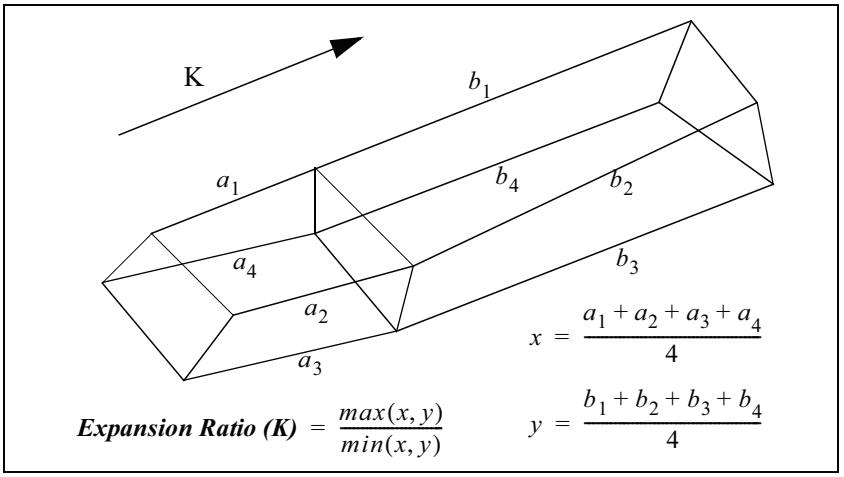

Figure 2.28: Expansion ratio definition of the control volume (AutoGrid5™ Manual, 2010).

with a large number of control volumes.

The term "grid convergence" is often noted in the CFD environment to access the quality of the solution. The argument is that the solution is dependent, amongst others, on the total number of CVs in the grid. As the number of CVs increase for subsequent grids of the same geometry, the error relative to the previous grid reduces to the point where an increase in CVs does not translate in sufficiently better accuracy. Thus convergence of the number of CVs in the grid has been achieved.

During the thesis, the meshes routinely contained more than 1 million CVs for the impeller and nearly 1 million CVs for the diffuser section. This was after configuring the meshing parameters to achieve a high quality mesh. Thus the

aim wasn't to create a grid with a sufficient number of CVs, but to primarily create a high quality mesh.

2.3.4 The Reynolds Number Effect

Through similarity relations, a researcher can perform tests on a centrifugal compressor at certain inlet conditions, but then scale the results to different inlet conditions. This is commonly done, as was evident in the Eckardt O-Rotor and Radiver test cases. The researchers involved in both these cases provide equations to scale the results appropriately and the commonly affected values are the mass flow rate, impeller rotation speed and the static and total pressures and temperatures. The boundary layer thickness is typically not scaled.

Scaling the values introduces what is referred to as the "Reynolds Number effect" by Ziegler *et al.* (2003*c*). Due to the mass flow rate (hence the Reynolds number as well) changing, the skin friction coefficient will change according to the model supplied in Appendix A.3. With a change in c_f, the boundary layer thickness will be affected as seen in Equation (A.4.1). Thus a change in Reynolds number will result in a change in relative boundary layer thickness and hence a change in effective flow area.

Analysis models actively implementing the boundary layer will report different results, even if scaled, when presented with scaled inlet conditions. This is true in the CFD environment where the viscous sub-layer is solved by the turbulence model. Thus CFD simulation results are especially prone to the Reynolds number effect.

To prevent this, Ziegler *et al.* (2003*c*) provide the unscaled measured data and recommends the use thereof for CFD simulations instead of the scaled values. It is generally good practice to use measured results where available instead of scaled values.

2.3.5 Stable Simulations

Solving the Radiver and DEEP prototype models with FINE™/Turbo presented unstable simulations, i.e. negative pressures were routinely calculated by the solver and would lead to the solver stopping. The main reason was due to flow re-entering at the outlet boundary with the preliminary meshes. For the Radiver test case, the re-entering was caused by the thick vaned diffuser blades introducing separation at the trailing edge and subsequent eddies propagating to the outlet boundary.

Similarly, the observed separation over the larger part of the vane of the DEEP prototype vaned diffuser was not fully recovered before reaching the outlet boundary, thus recirculating flow was still present at the outlet.

It was decided to lengthen the outlet with a vaneless annular passage and then pinch (narrow) the outlet to constrict the flow. The length of additional

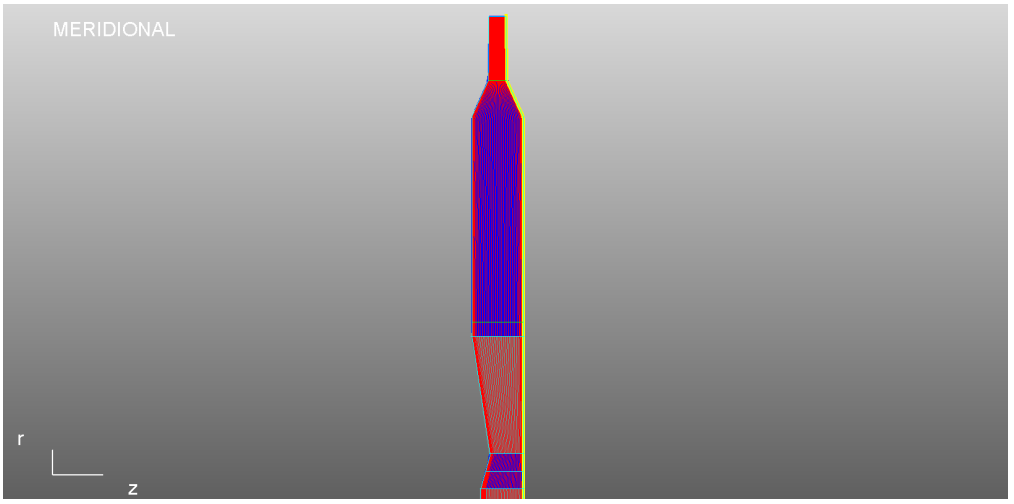

Figure 2.29: Pinching of the DEEP prototype outlet in AutoGrid5™.

vaneless space ideally needs to be the radial length of the vaned diffuser section (downstream of the last measuring station) and the pinching has to be performed symmetrically from both the hub and shroud surfaces. This is illustrated at the top of Figure 2.29, which shows pinching of the DEEP prototype.

By lengthening the outlet, the flow has time to recover before reaching the outlet boundary. The pinching process accelerates the flow leading to a higher velocity gradient and reducing the chances of recirculation. However, the pinching must not be applied too aggressively, as defining the flow area too small could lead to higher Mach numbers and subsequent supersonic flow. The vaneless annular passage must also not be too long as this will increase the total number of grid points and will lead to a longer solving time and larger solution files size.

Pinching the flow sufficiently downstream of the last measuring station does not influence the results as this resembles throttling the flow, similar to constricting the flow during experimental testing with a valve. By inserting a cutting plane in CFView™ at the intended measuring station, the values can be observed on the newly created plane. If a range of mass flow rates are solved, a compressor curve can be compiled by averaging the values on the cutting plane for each computation.

Chapter 3

Validation of 1-D Theory and FINE™/Turbo

Due to a lack of reliable geometric data of the GE 7S1408 A1 compressor impeller, it was not possible to model the compressor stage with confidence and the need arose to illustrate the proficiency of the 1-D theory MATLAB® code and 3-D modelling capabilities of FINE™/Turbo. The result is a validation study using two well-known centrifugal compressor cases, namely the O-Rotor by Eckardt (1975, 1976, 1980) and Eckardt and Trültzsch (1977) and the Radiver open CFD test case by Ziegler *et al.* (2003*c*, 2003*a*, 2003*b*) and Ziegler *et al.* (2004).

This section discusses the various parameters considered during selection of the test cases. Summaries of the required geometry and operating conditions for 1-D and 3-D modelling are supplied for each test case. In conclusion, the results obtained by the 1-D and 3-D models are supplied and discussed.

The focus was on performance prediction (pressure ratios, flow angle etc.) using area and time averaged values, as the 1-D modelling method by nature cannot provide pressure distributions from hub to shroud for instance.

3.1 Justification of Validation Study Cases

This subsection provides an overview of the two test cases with comparisons to the two compressors (GE 7S1408 A1 and DEEP prototype) relevant to this thesis. More detailed information on the compressors are supplied in the following subsections.

To ensure that the results of the case studies were applicable to the investigation project, certain criteria were identified and needed to be adhered to. These were:

- It must be a well known study with published results.

- It must have been previously used for validation studies or investigated by the turbomachinery community.
- The geometry and operating conditions must be similar to the GE 7S1408 A1 and DEEP prototype compressors.
- The geometric data and operating conditions must be obtainable.

Eckardt analysed three different centrifugal impellers with vaneless diffusers. These impellers are known as the following:

- The O-Rotor [Eckardt (1975), Eckardt (1976) and Eckardt and Trültzsch (1977)] with radial blades, $\beta_2 = 90°$.
- The A-Rotor [Eckardt and Trültzsch (1977) and Eckardt (1980)] with backswept blades of $\beta_2 = 60°$.
- The B-Rotor [Eckardt and Trültzsch (1977) and Eckardt (1980)] with backswept blades of $\beta_2 = 50°$.

The first test case was designated to be the O-Rotor. The O-Rotor utilises a single, radial impeller with vaneless diffuser (linearly tapered or hyperbolically contoured shroud). The impeller is an early design and implements circular arcs for hub and shroud contours and an ellipsoidal camberline curve. Difficulties in obtaining reliable geometrical information of the A- and B-Rotor discouraged their use for validation purposes.

The second test case was identified as the Radiver open CFD test by Ziegler *et al.* (2003*c*), which studied the influence of the impeller-diffuser gap on compressor performance. This compressor implements a back-swept impeller with a parallel-walled, wedge-type diffuser and is of a more modern and complex design than the O-Rotor, hence providing an adequate range in complexity for modelling between the two cases.

To compare the operating ranges of the O-Rotor and GE 7S1408 A1 compressor, refer to Table 3.1. Similarly, to compare the Radiver and DEEP prototype, refer to Table 3.2.

The O-Rotor was chosen due to similarities to the GE 7S1408 A1 impeller. This included similar operating conditions and near identical impeller tip geometry, with both having radial ending blades and similar channel heights at

Table 3.1: Operating range comparison of the O-Rotor and GE 7S1408 A1 compressor [Eckardt (1975), Japikse and Baines (1997) and Van der Spuy (2003)].

Compressor	N_{max} (RPM)	$PR_{TT,max}$	$\eta_{TT,max}$ (%)	$\dot{m}_{max}$ (kg/s)
O-Rotor	18 000	3.1	0.9	8.0
GE 7S1408 A1	19 000 to 20 000	2.7 to 2.8	±0.76	3.8

Table 3.2: Overall performance comparison between the Radiver and DEEP prototype [Ziegler *et al.* (2003*c*) and Van der Spuy (2003)].

Compressor	N_{max} (RPM)	$PR_{TT,max}$	$\eta_{TT,max}$ (%)	$\dot{m}_{max}$ (kg/s)
Radiver test case	35 200	4.07	0.834	2.5
DEEP prototype	19 200	3.25	0.78	4.7

the tip. The O-Rotor has a larger inlet area due to the smaller hub radius and resulting larger channel height, which in part accounts for the higher maximum mass flow rate with similar maximum rotational speeds. The O-Rotor utilises a vaneless diffuser only, with the GE 7S1408 A1 compressor implementing a logarithmic spiral type diffuser.

Testing procedures and results of the O-Rotor have been widely used for turbomachinery validation and comparison purposes, both in the CFD [Rulth and Kelecy (2004), Anderson (2009)] and literature environment [Japikse and Baines (1997), Qiu *et al.* (2007) and Anderson (2009)]. Concepts NREC™'s interest in the O-Rotor also lead to a 3-D model being supplied in a tutorial for CCAD® users. This model was used to define the geometry used in the validation study.

Few comparisons between the DEEP prototype and Eckardt's O-Rotor can be drawn, but the shortfalls are overcome with the Radiver test case. Even though the Radiver impeller is smaller than the two project compressors, it is applicable to the DEEP prototype due to the backswept blades at the impeller tip and inclusion of a vaned diffuser. The amount of backsweep of the Radiver places the DEEP prototype impeller tip's geometry "between" the radial blades of the O-Rotor and the backswept blades of the Radiver.

The wedge type diffuser implemented by the Radiver is relevant to the thesis as Concepts NREC™ suggested this type of diffuser for the DEEP prototype (Van der Spuy, 2003). The vaned diffuser theory by Aungier (2000) was originally intended for thin-vaned or airfoil diffusers (Aungier, 1990) and has been adapted for use on thick or wedge type vanes. If adequate correlations between the Radiver 1-D and experimental results are found, it will thus also illustrate robustness of the 1-D theory.

From a CFD point of view, the separation caused (hence with high turbulence level) by the Radiver diffuser's thick vanes at the discharge presents a challenge to the numerical solver. Thus, the much thinner vanes of the DEEP prototype will prove to be relatively simple to model once the 1-D and 3-D modelling methods have been verified.

Information on the Radiver is easy to obtain since Ziegler *et al.* (2003*c*) compiled a CD-ROM containing both steady and unsteady experimental results, the compressor geometry, figures, animations and supplementary information. This CD-ROM can be obtained by contacting the original authors.

No case could be obtained which implemented splitter blades in the im-

peller (the DEEP prototype includes splitter blades) and which also satisfied the decision criteria for the test cases. Krain and Eckardt (1978) and subsequently Krain (1981) performed tests on a variation of the O-Rotor which consisted of a similar impeller geometry. The impeller included splitter blades with 24 blades in total, compared to 20 of the O-Rotor. The impeller stage was followed by a wedge-type vaned (15 vanes in total) diffuser of flat-plate design and has since been known as the Krain diffuser stage.

Krain (1981) does not supply sufficient geometrical information and a copy of Krain and Eckardt (1978) could not be procured, thus no verifiable geometry and operating conditions for the Krain diffuser could be obtained. Hence, the Krain diffuser was not used for validation purposes. But the theory of Aungier (2000) includes alterations for modelling a splitter blade impeller and the meshing capabilities of AutoGrid5™ accommodates splitter blades in the impeller design.

3.2 The Eckardt O-Rotor

This section provides the required geometry and operating conditions of the Eckardt O-Rotor to perform the 1-D and 3-D test case analysis, followed by a discussion on the 1-D and 3-D results.

3.2.1 Geometric Information and Operating Conditions

A photo of the O-Rotor is shown in Figure 3.1 and Figure 3.2 shows a meridional view of the compressor, detailing the measurement stations.

Insufficient geometrical information is supplied by Eckardt (1975, 1976) to compile the 3-D blade geometry from literature alone, but the software package CCAD® by NREC™ includes a demonstration file of the O-Rotor in a tutorial. The CCAD® model's hub and shroud contours (from impeller inlet to tip) as well as the blade stream surface coordinates can be exported, which were used to compile the project *.geomTurbo* file. The validity of the model is supported by the use of Concepts NREC™'s software by other authors (Japikse and Baines (1997), Anderson (2009), Dubitsky and Japikse (2008) and Japikse and Oliphant (2005)). The original 3-D model was altered to include a bulb inlet and vaneless diffuser, of which the outlet was lengthened and pinched. AutoGrid5™ v8.4-3 meshing results are shown in Appendix C.1 and the resulting domain contained 1 366 070 grid points.

Eckardt (1976) describes the relation of the diffuser shroud contour and flow area as follows: *"the attached vaneless diffuser has constant flow area up to* $r/r_2 = 2$*"* and Eckardt (1980) describes the geometry as having a *"vaneless constant-area diffuser up to* $r/r_2 = 2$*"*. To obtain a constant flow area, the shroud requires a hyperbolic curved profile, assuming the hub profile has a constant axial coordinate starting at the impeller tip. This is shown in Equa-

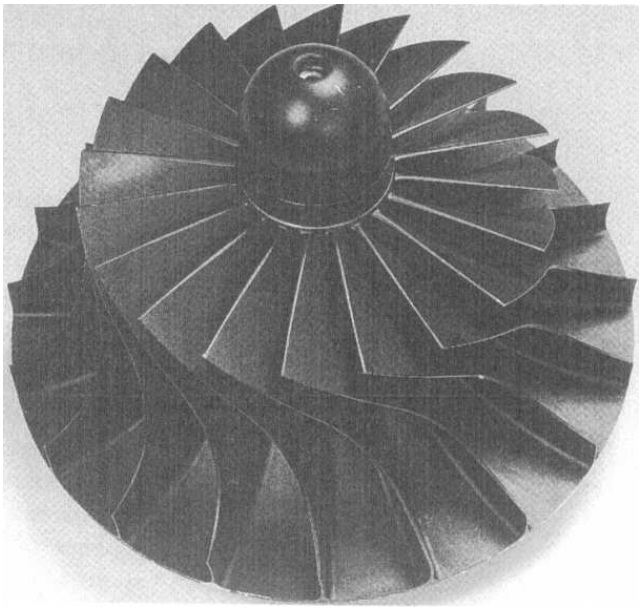

Figure 3.1: Eckardt's O-Rotor (Japikse and Baines, 1997).

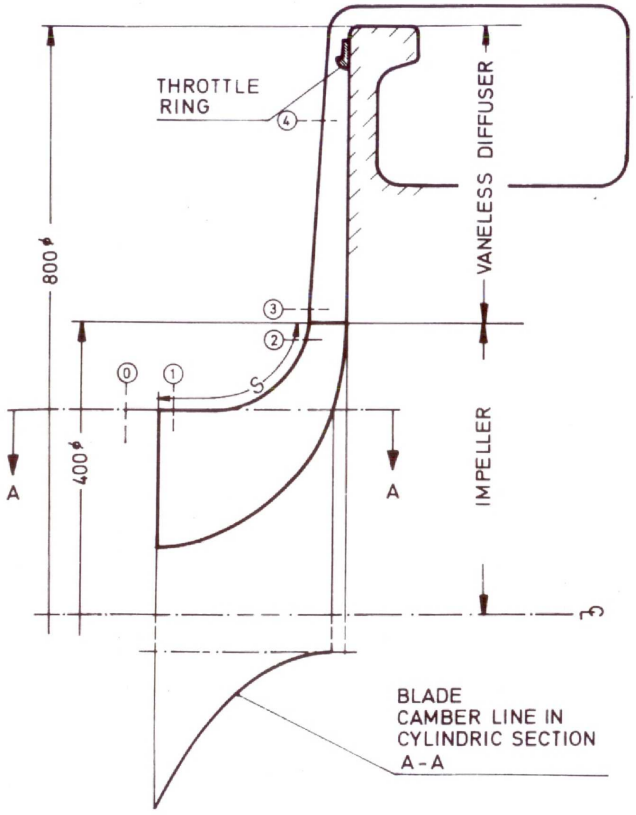

Figure 3.2: Original meridional view of the O-Rotor (Eckardt, 1975).

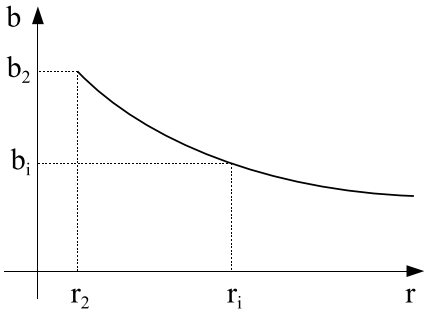

Figure 3.3: O-Rotor hyperbolic diffuser shroud sketch.

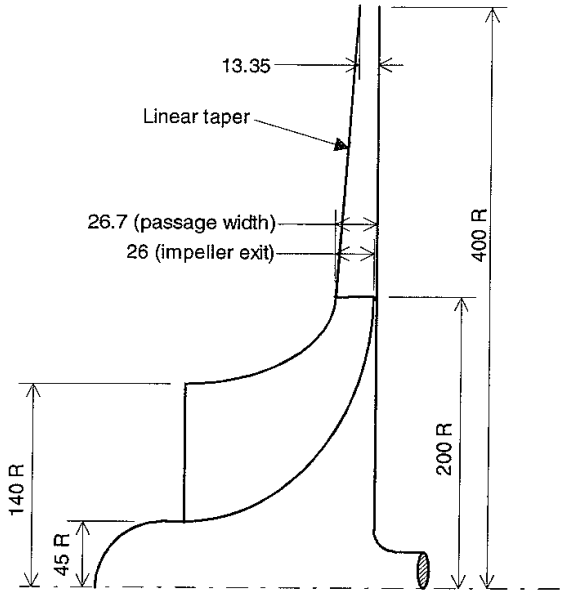

Figure 3.4: Additional O-Rotor meridional view (Japikse and Baines, 1997).

tion (3.2.1), which is accompanied by Figure 3.3. A hyperbola is characterised by the equation $xy = k$ with $k > 0$ and k a constant (Stewart, 2003), or in this case $r_i b_i = k$.

$$\begin{aligned} \text{Flow Area} &= b_2\,(2\pi r_2) = b_i\,(2\pi r_i) \\ \Rightarrow r_i b_i &= r_2 b_2 \\ &= \text{constant} \qquad (r_2 \text{ and } b_2 \text{ are constants}) \end{aligned} \tag{3.2.1}$$

The written literature conflicts with the sketches available, such as found upon closer inspection of Figure 3.2 where the shroud seems to be linear. Another example of the meridional view by Japikse and Baines (1997) is shown in Figure 3.4, which refers to the diffuser shroud contour as having a linear taper. This is repeated by Japikse and Baines (1998).

Thus, the author found a contradicting definition of the shroud contour. No clarification could be found in the literature between figures and information supplied in the text describing the shroud contour, thus the author chose to use both cases.

Not all of the geometric information required for 1-D modelling was supplied by the available publications, such as the clearance width of the labyrinth seal between the impeller disk and casing or the blade thickness distribution. The labyrinth seal clearance width was chosen to be identical to the shroud clearance gap and the impeller inlet and tip blade thickness was extracted from the 3-D model using IGG™. The throat area, streamline curvature and blade mean streamline and camberline lengths were calculated using IGG™ and the method described in Section 7.6 by Aungier (2000).

The fixed throttle ring depicted in Figure 3.2 at $r/r_2 = 1.9$ was installed to control the choke limit of the compressor and prevent the exit flow from disturbing the axisymmetric impeller flow pattern according to Eckardt (1975, 1976). No further geometric information is supplied in any of the subsequent publications, other than the replacement of the fixed throttle ring with an axially traversable throttle ring according to Eckardt (1980). The closest measurements were taken upstream at station 4, thus the ring was excluded in the 1-D and 3-D models.

Further geometrical information regarding the impeller required for 1-D modelling is supplied in Table 3.3, which includes information of the GE 7S1408 A1 compressor for comparison. Due to the O-Rotor having a vaneless diffuser, no direct comparison can be made between the O-Rotor and GE 7S1408 A1 compressor other than the diffuser outlet diameter being similar at $r_2 = 0.4\,\mathrm{m}$.

A compressor performance curve at $N = 14\,000\,\mathrm{RPM}$ is provided by Eckardt (1975) and three (M1, M2 and M3) specific test points are supplied, shown in Table 3.4. These points were used during the validation process. The performance curve by Eckardt (1975) specifies that the total-to-total conditions are taken from the inlet (station 0) to a radius ratio of $r/r_2 = 1.69$ (station 4).

Eckardt (1975) used the total inlet and outlet temperatures and pressures to calculate the total-to-total isentropic efficiency as shown in Equation (3.2.2).

$$\eta_{TT,0-4} = T_{t,0}\frac{(p_{t,4}/p_{t,0})^{(\gamma-1)/\gamma} - 1}{(T_{t,4} - T_{t,0})} \tag{3.2.2}$$

As shown in Table 3.4, correction factors are used to adapt the rotational speed and mass flow rate. These factors are coupled to standard atmospheric conditions for scaling due to different inlet conditions as shown in Equation (3.2.3).

$$\begin{aligned} \delta &= p_t/101\,325\,\mathrm{Pa} \text{ for pressure} \\ \theta &= T_t/288.1\,\mathrm{K} \text{ for temperature} \end{aligned} \tag{3.2.3}$$

No explicit inlet operating conditions are specified in the available publications. By choosing the inlet conditions as the indicated atmospheric properties

Table 3.3: Impeller geometry of the O-Rotor and GE 7S1408 A1 compressor [Japikse and Baines (1997) and Van der Spuy (2003)].

		O-Rotor	GE 7S1408 A1
Inlet	$r_{1,h}$ (mm)	45	58
	b_1 (mm)	95	62.6
	r_1 (mm)	103.99	94.6
	$\beta_{1,h}$	57.12°	45.7°
	β_1	33.83°	38.6°
	$\beta_{1,s}$	26.75°	33.1°
	$\alpha_{C,1}$	1.68°	
	$\kappa_{m,1}$ (rad/m)	-2.49	
	$t_{b,1}$ (mm)	2.11	2
	z_1	20	20
Throat	A_{th} (mm^2)	32.0801×10^3	
	r_{th} (mm)	103.99	
	β_{th}	39.76°	
	peri$_{th}$ (m)	4.422	
Tip	r_2 (mm)	200	195
	b_2 (mm)	26	20
	β_2	89.78°	90°
	$\alpha_{C,2}$	86.15°	
	$t_{b,2}$ (mm)	1.08	4
	z_2	20	20
Overall	L_B (mm)	202.26	
	L_{FB} (mm)	171.26	
	s_{CL} and s_D (mm)	0.372	

Table 3.4: O-Rotor compressor performance test points Eckardt (1975).

Test point	$N/\sqrt{\theta}$ (RPM)	$\dot{m}\sqrt{\theta}/\delta$ (kg/s)	$PR_{TT,0-4}$	$\eta_{TT,0-4}$ (%)
M1	14 000	6.09	2.061	86.8
M2	14 000	5.31	2.094	88.0
M3	14 000	4.53	2.086	86.5

($p_{t,0} = 101\,325$ Pa and $T_{t,0} = 288.1$ K), the correction factors reduce to 1. Thus, the rotational speed and mass flow rate values in Table 3.4 do not need to be corrected.

The results can be influenced by the Reynolds number effect (discussed in Section 2.3.4). To investigate the sensitivity, the 3-D simulations for the operating point, M2, were run at different inlet conditions and the values scaled accordingly. After considering the test setup information (open circuit with a straight axial inlet pipe) supplied by Eckardt (1976), the inlet conditions were

chosen as $p_{t,0} = 95\,000\,\text{Pa}$ and $T_{t,0} = 290\,\text{K}$. The scaled rotational speed and mass flow rate equate to 14 046.1 RPM and 4.962 kg/s respectively. Results of these simulations, which were rescaled for comparison, are supplied and referenced with an asterisk (∗) in Section 3.2.2.

3.2.2 Modelling Results and Discussion

Due to the nature of the project, only averaged or 1-D results were needed from the simulations for verification. These are flow angles, pressures and temperatures, such as the information in Table 3.4. The testing method implemented by Eckardt for the 1-D and 2-D measurements resemble an area averaged technique, thus area averaging was implemented in CFView™.

Both the linear and hyperbolic diffuser shroud cases were investigated and the hyperbolic results showed better correlation with the experimental data, both in overall performance and averaged values in the diffuser. This scenario is also the best representation of the description given in the text by Eckardt (1975, 1976 and 1980). Due to this, only the results of the hyperbolic case are shown in the main section of the thesis. Modelling results of the linear case are supplied in Appendix F for comparison.

The 1-D model CV radial length for the vaneless annular passage can be set by the user. In accordance with the grid convergence approach, the CV length was decreased until the change in end result relative to the previous CV length was acceptable. With a decrease in CV length, the number of iterations per CV decreases. The result was a CV length of 10 µm, leading to 20 000 grid points along the length of the vaneless diffuser.

The three specific test results provided by Eckardt (1975) (Table 3.4) are evaluated first. Refer to Figures 3.5 and 3.6 for the hyperbolic contoured total-to-total pressure ratio (PR_{TT}) and total-to-total efficiency (η_{TT}) curves.

As can be seen, the 1-D results show better correlation close to the choke margin, with the largest error near the stall margin. The difference in PR_{TT} at 4.53 kg/s is 0.14 and 5.48 % for η_{TT}. The 3-D results show better correlation close to the stall and choke margins, but at 5.31 kg/s the difference in PR_{TT} is 0.043 and in η_{TT} it is 1.99 %.

The results of the Reynolds number effect investigation show very little difference to the results of the simulation performed at standard inlet conditions. Thus, any error introduced by performing the simulations at standard inlet conditions is considered negligible and it is assumed that the Reynolds number effect only becomes significant when the tested inlet conditions differ considerably from standard inlet conditions. Instead of assuming inlet conditions substantially different from standard inlet conditions, the standard inlet conditions were used for the investigation.

Japikse and Baines (1997) provide impeller tip results at 5.31 kg/s and 14 000 RPM, which originate from the studies by Eckardt (1980). These results are supplied in Table 3.5 and the errors (provided in brackets) for all three

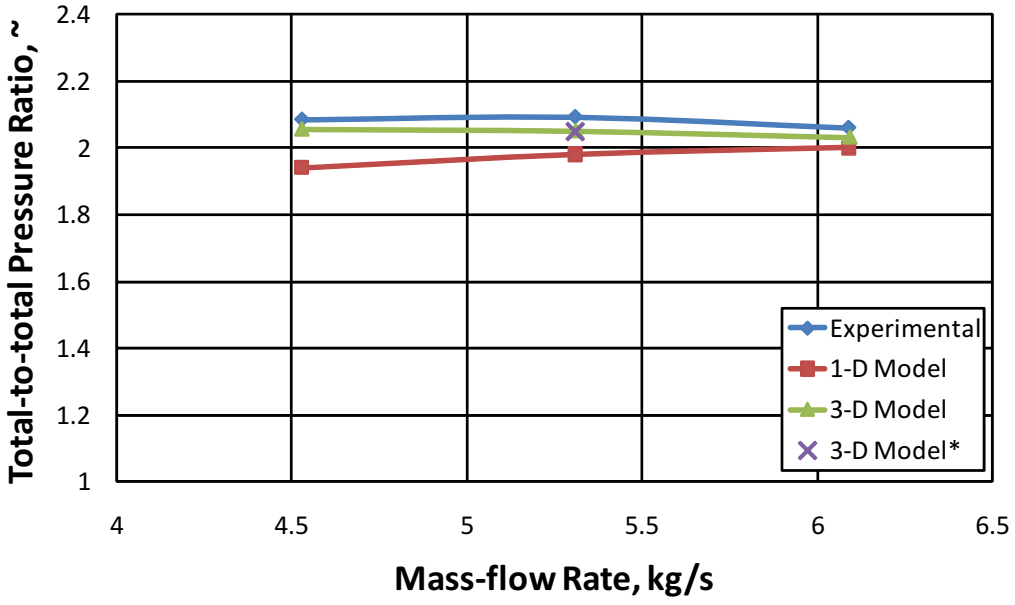

Figure 3.5: Total-to-total pressure ratios of the O-Rotor with a hyperbolic shroud at 14 000 RPM (Eckardt, 1975).

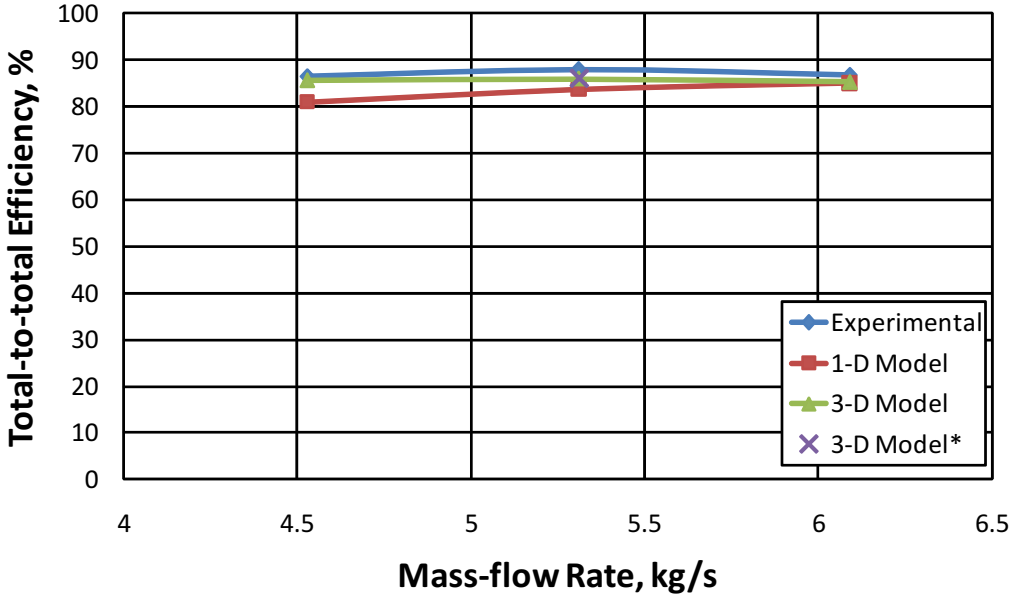

Figure 3.6: Total-to-total efficiencies of the O-Rotor with a hyperbolic shroud at 14 000 RPM (Eckardt, 1975).

Table 3.5: O-Rotor impeller tip conditions at 5.31 kg/s and 14 000 RPM (Japikse and Baines, 1997).

	Exp.	1-D	3-D	
			Linear	Hyperbolic
$T_{t,2}$ (K)	363.5	363.0 (0.14%)	366.6 (−0.85%)	366.5 (−0.82%)
$p_{t,2}$ (kPa)	220.5	219.6 (0.4%)	219.7 (0.35%)	219.6 (0.43%)
p_2 (kPa)	144.7	149.1 (−3.01%)	145.7 (−0.68%)	145.6 (−0.64%)
α_2	23.7°	21.94° (1.76°)	21.93° (1.77°)	21.98° (1.72°)

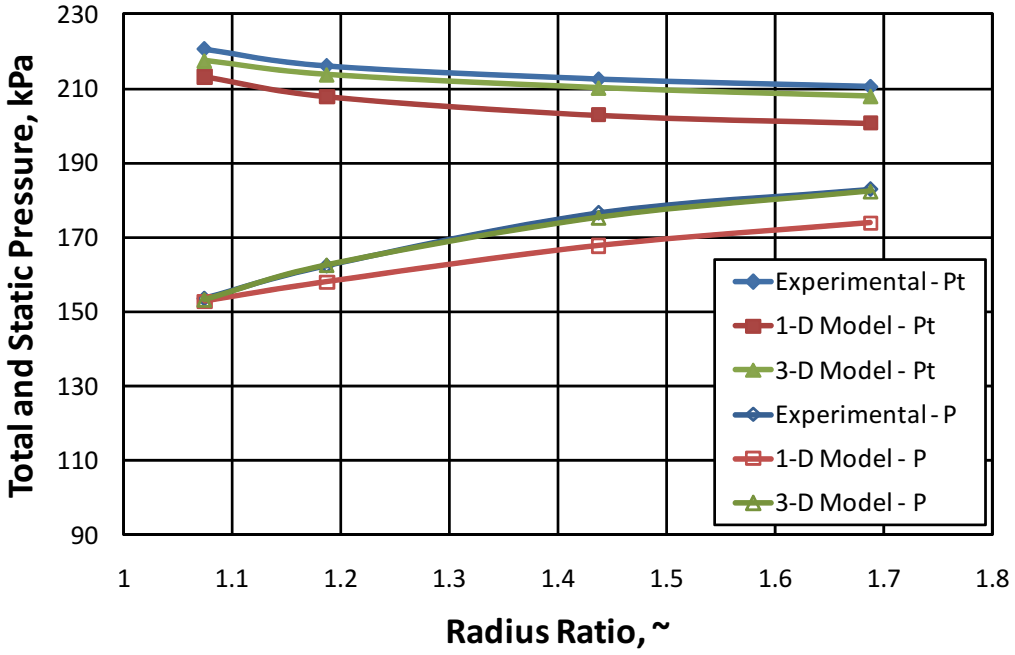

Figure 3.7: Pressures along the diffuser of the O-Rotor with a hyperbolic shroud at 14 000 RPM and 5.31 kg/s (Dubitsky and Japikse, 2008).

measurements are small, with the 1-D analysis performing as good as the 3-D model. Due to the 1-D code addressing the impeller and diffuser separately, the 1-D impeller results for the linear tapered and hyperbolic contoured shroud are identical. Area-averaged values of the 3-D results were evaluated at a radius ratio (r/r_2) of 1.005 to avoid the metal face of the impeller tip. This equates to an acceptable 1 mm difference in the radial direction.

For verification of the flow angle and pressure recovery predictions, results of the O-Rotor diffuser were investigated. Results at 14 000 RPM from studies by Eckardt and Trültzsch (1977) were obtained through the publication by Dubitsky and Japikse (2008) and a comparison of the hyperbolically contoured shroud's modelling results in the diffuser are shown in Figures 3.7 and 3.8.

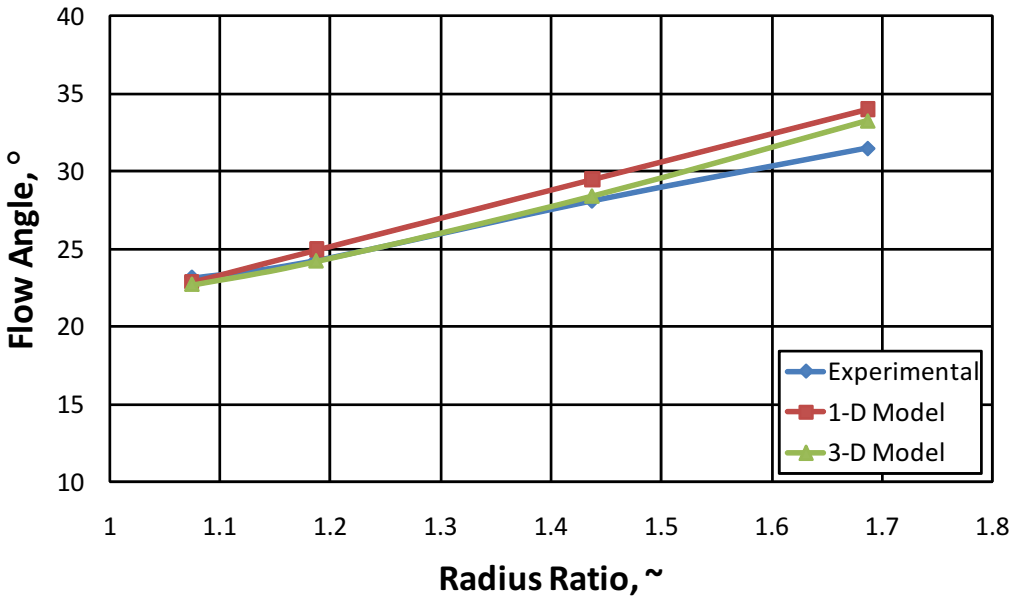

Figure 3.8: Flow angles along the diffuser of the O-Rotor with a hyperbolic shroud at 14 000 RPM and 5.31 kg/s (Dubitsky and Japikse, 2008).

The 1-D model results underestimate both the total (p_t) and static (p) pressure trends, with p_t showing better correlation with the experimental results. The largest error in 1-D results of p_t is 4.64 % (9.76 kPa) at a radius ratio (r/r_2) of 1.6875 and the largest error in p is 5.08 % (8.97 kPa) at $r/r_2 = 1.4375$. Correlation of the 3-D model p results with the experimental results are good, with the largest error of 0.35 % (1.4 kPa) at $r/r_2 = 1.4375$. Even though the trend of the 3-D model p_t curve correlates well with the experimental results, it is underestimated, with the largest error being 1.38 % (3.05 kPa) at $r/r_2 = 1.075$. This is still regarded as good.

Flow angle (α) predictions for both the 1-D and 3-D models are regarded as good, particularly in the area of interest, namely at $r/r_2 \approx 1.1$. Vaned diffuser design guidelines by Aungier (2000) recommends $1.06 \leq r_3/r_2 \leq 1.12$ with a vane incidence angle ($i_3 = \beta_3 - \alpha_3$) at the compressor design point of around $-1°$. The difference for the 1-D results at $r/r_2 = 1.075$ is 0.26°, increasing to $-0.68°$ at $r/r_2 = 1.1875$. The error in 3-D results at $r/r_2 = 1.075$ is 0.45°, reducing to 0.07° at $r/r_2 = 1.1875$, thus being an order less than the recommended incidence angle.

Test results of the O-Rotor at 12 000 RPM by Eckardt and Trültzsch (1977) were obtained through Japikse and Oliphant (2005). Diffuser modelling results at the known mass flow rate of 3.86 kg/s for the hyperbolic shroud are supplied in Figures 3.9 and 3.10.

The 1-D pressure results show poorer correlation at the lower mass flow rate and RPM, with the largest error in p_t of 4.59 % (8.17 kPa) at $r/r_2 = 1.4375$.

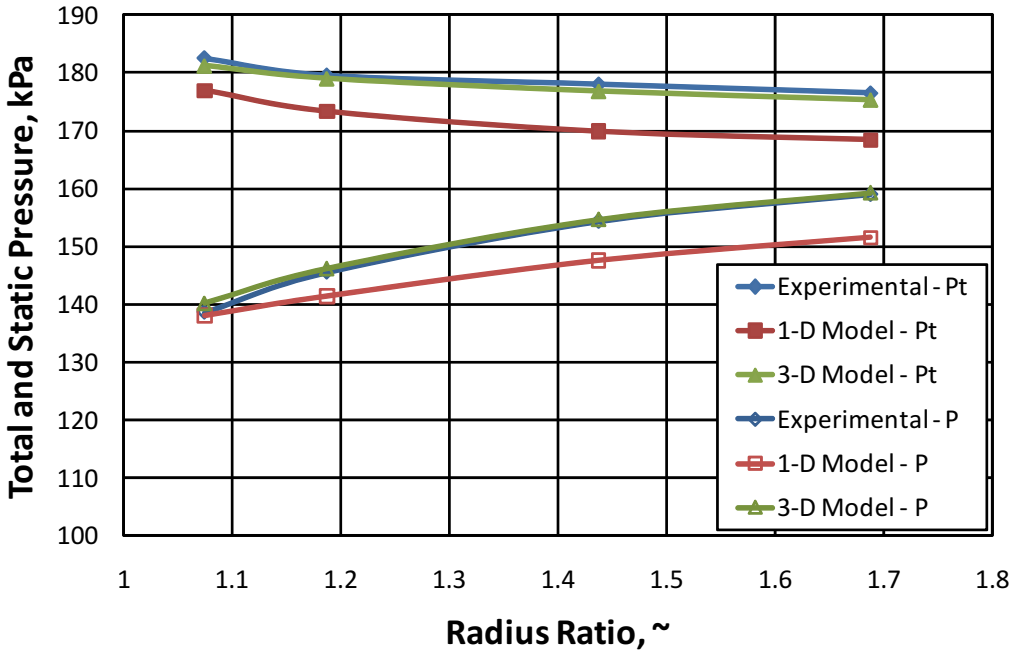

Figure 3.9: Pressures along the diffuser of the O-Rotor with a hyperbolic shroud at 12 000 RPM and 3.86 kg/s (Dubitsky and Japikse, 2008).

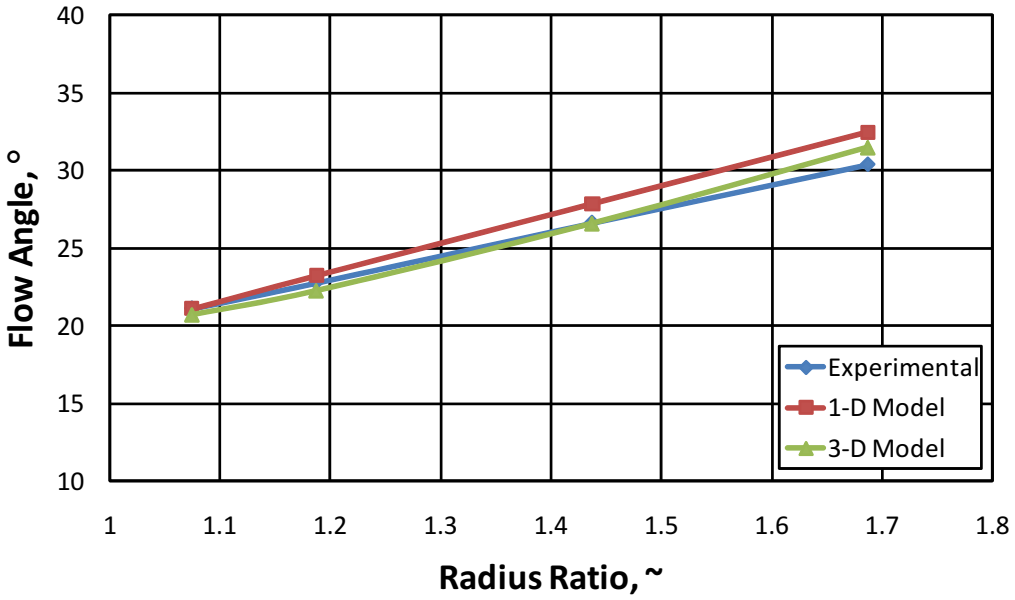

Figure 3.10: Flow angles along the diffuser of the O-Rotor with a hyperbolic shroud at 12 000 RPM and 3.86 kg/s (Dubitsky and Japikse, 2008).

The error in p is 4.68 % (7.44 kPa) at $r/r_2 = 1.6875$. The 3-D results still show good correlation with the experimental results with p_t following the experimental trend with a smaller maximum error than found in Figure 3.7, being 0.74 % (1.35 kPa) at $r/r_2 = 1.075$. The error in p is −1.07 % (−1.49 kPa) at $r/r_2 = 1.075$. The flow angle predictions for both the 1-D and 3-D models show good correlation with the experimental results, with differences of −0.007° and 0.387° at $r/r_2 = 1.075$ for the 1-D and 3-D models respectively.

The 1-D analysis at 14 000 RPM predicts impeller blade stall occurring from 4.53 kg/s to 5.31 kg/s and inducer stall from 4.53 kg/s to 4.962 kg/s. Impeller blade stall is mainly evaluated at the impeller tip by Aungier (2000) and can be expected when $D_{eq} > 2$ according to Equation (B.1.25). Visually this is associated with flow re-entering the impeller at the tip. The 1-D prediction was investigated for the hyperbolic shroud case in CFView™ and the occurrence of blade stall is evident as shown in Figure 3.11. The figure contains plots of relative velocity stream lines at the impeller tip.

Recirculation at the tip is shown in Figure 3.11a where the 1-D code predicted $D_{eq} = 2.206$, diminishing to the conditions shown in Figure 3.11b where $D_{eq} = 2.015$. The 1-D code predicted $D_{eq} = 1.846$ at a mass flow rate of 6.09 kg/s where a small amount of recirculation is still visible.

3.3 The Radiver Test Case

Following the O-Rotor investigation and the absence of reliable Krain diffuser information, an additional similar case with more complex geometry was investigated, namely the Radiver open CFD test case.

Ziegler *et al.* (2003*c*) recognised the lack of knowledge on the influence of interaction between an impeller and diffuser. The result was a study on a back-swept centrifugal compressor impeller (supplied by MTU Aero Engines) with a flat (parallel hub and shroud walls), wedge-type vaned diffuser (designed by Rothstein (1993)). A photo of the Radiver compressor without the shroud is shown in Figure 3.12.

In conclusion of the project, Ziegler *et al.* (2003*b*) mention the challenge in predicting the flow in the diffuser channel whilst focussing on the sensitivity of the radial gap. For this reason, Ziegler *et al.* (2003*c*) published the steady and unsteady experimental results as an open CFD test case with the name "Radiver". A licensed test case CD-ROM containing compressor geometry, figures, animations and supplementary information is available upon request from the original authors. A two-part ASME publication is also available [Ziegler *et al.* (2003*a*) and Ziegler *et al.* (2003*b*)].

No extensive information regarding the test setup and compressor geometry of the Radiver test case is supplied in this thesis, other than what is needed for the 1-D analysis. Additional information can be found on the Radiver CD-ROM.

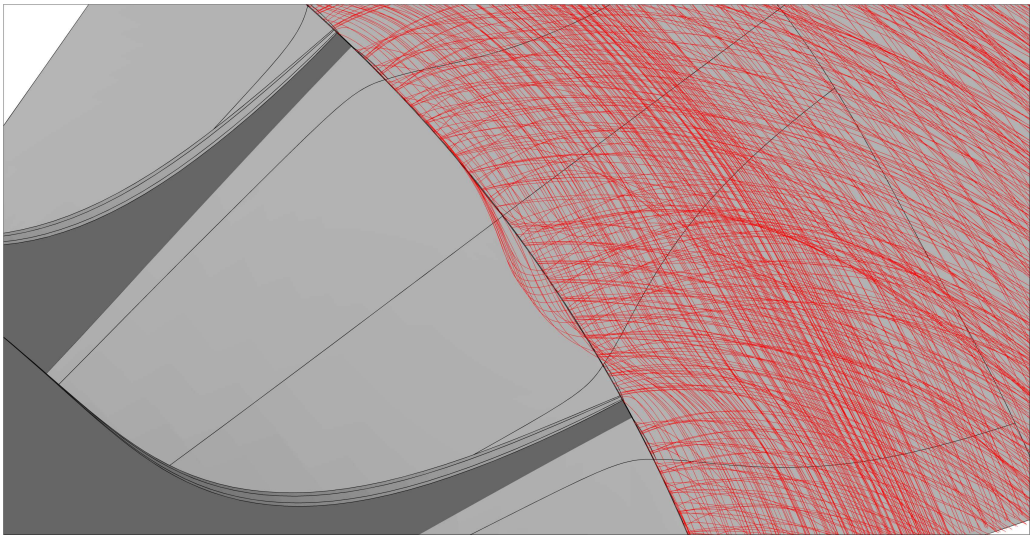

(a) $\dot{m} = 4.53\,\mathrm{kg/s}$ with $D_{eq} = 2.206 > 2$.

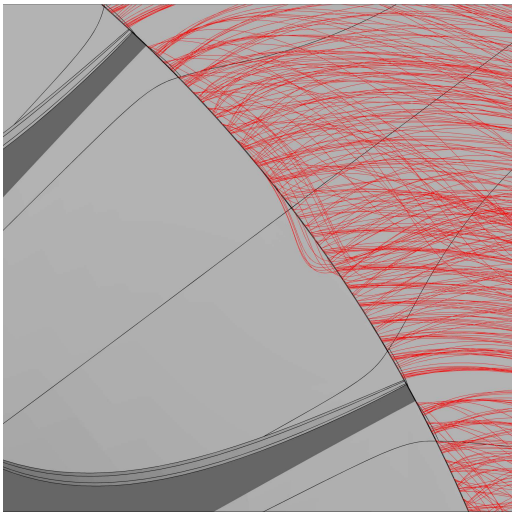

(b) $\dot{m} = 5.31\,\mathrm{kg/s}$ with $D_{eq} = 2.015 > 2$.

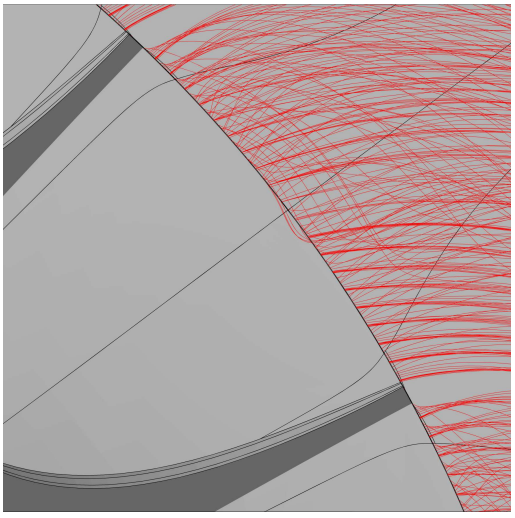

(c) $\dot{m} = 6.09\,\mathrm{kg/s}$ with $D_{eq} = 1.846 < 2$.

Figure 3.11: Recirculation at O-Rotor tip at 14 000 RPM and 50 % span.

Figure 3.12: The Radiver compressor stage (Ziegler *et al.*, 2003*c*).

3.3.1 Geometric Information and Operating Conditions

The diffuser vanes were independently adjustable regarding the vane angle and the radial gap between the impeller tip and vane leading edge. Ziegler *et al.* (2003*c*) placed emphasis on investigating the radial gap to determine the impeller-diffuser interaction intensity.

Results for steady state probe measurements and detailed time resolving laser-2-focus (L2F) measurements are provided by Ziegler *et al.* (2003*a*) and Ziegler *et al.* (2003*b*) respectively. The probe measurements were conducted with a vaneless diffuser (with cylindrical spacers in the place of the diffuser vane adjustment mechanism) and with the diffuser vanes at two different vane angles, each combined with a selection of radial gaps.

The thick black lines in Figures 3.13 and 3.14 show where the measurements were taken in the meridional view and along the diffuser respectively. Ziegler (2003) recommend using measuring plane 7M for comparisons with CFD results due to low Mach numbers with possible backflow regions in the wake of the thick diffuser vane trailing edges at measuring plane 8M. Another recommendation, regarding the L2F measurements, is to be careful when comparing the results on the 5M plane with the CFD results. Reflection of the laser light from the rear wall and vane surfaces was experienced and the results were therefore not of the same quality as the 2M', 2M and 4M plane measurements.

According to Ziegler (2003), the flow angles reported for the 2M plane (α_{2M}) using the probe measurements and measured mass flow rate in the flow nozzle are about 2° more tangential than the values of the averaged L2F mea-

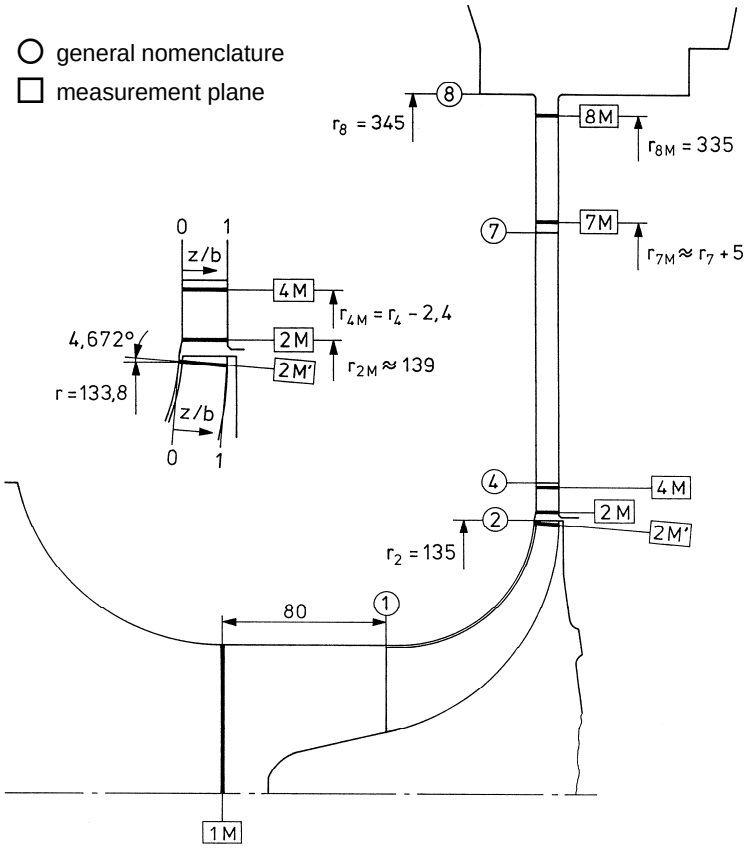

Figure 3.13: Measurement planes of the Radiver compressor in the meridional view (Ziegler *et al.*, 2003*c*).

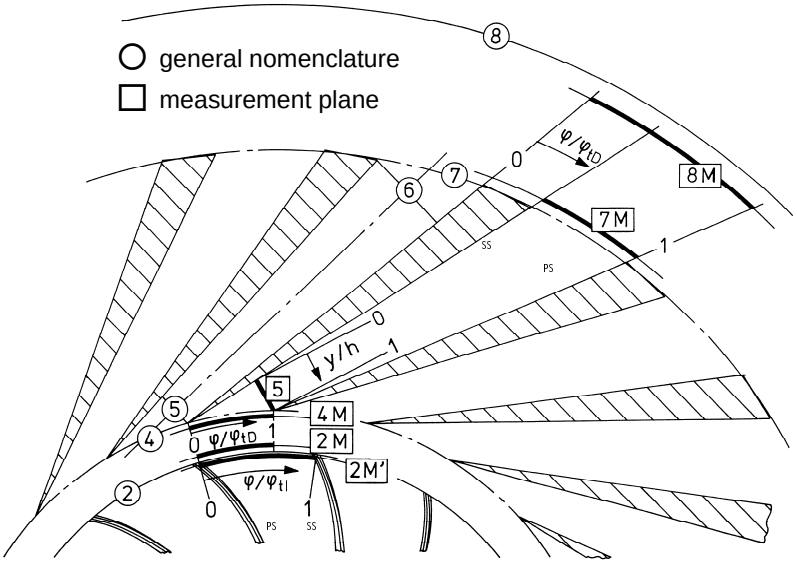

Figure 3.14: Measurement planes of the Radiver compressor along the diffuser (Ziegler *et al.*, 2003*c*).

Table 3.6: Test summary of the Radiver test case (Ziegler, 2003).

β_3	r_3/r_2	Probes			L2F	Compressor map	Dye injection
		2M	7M	8M			
19.8075°	1.04	x	x	x	x	60 – 100 %	x
	1.06		x	x		80 %	
	1.10		x	x		80 %	
	1.14		x	x	x	60 – 100 %	x
	1.18	x		x		80 %	
15.8075°	1.06		x	x		80 %	
	1.10		x	x		80 %	
	1.14		x	x		80 %	
	1.18		x	x		80 %	
Vaneless		x		x	x	60 – 100 %	x

surements. This was due to the integration method implemented for estimation by the probe measurements. But Ziegler (2003) note this difference to be quite small and that the values measured by the L2F may be used for CFD flow field comparison and the probe measurements for comparison of the flow angles in different operating points. Thus when comparing averaged α_{2M} results, the probe measurements may be used by taking the 2° difference into account.

Ziegler *et al.* (2003*a*) did not perform all of the measurements for all of the vane angles and radial gap configurations, but Ziegler (2003) supplied the summary of the test programme shown in Table 3.6. The vane angles were originally measured between the suction surface and tangent of the vane, but keeping with the convention of this thesis, the representative vane leading edge camberline angle (β_3) is supplied.

The decision to only investigate one vane angle ($\beta_3 = 19.8075°$) and radial gap ($r_3/r_2 = 1.14$) was based on the available experimental data. A larger vane angle was preferred as this would ensure a higher quality 3-D mesh with respect to cell orthogonality. Therefore, for a vane angle of $\beta_3 = 19.8075°$, extensive data is provided for two radial gap measurements, namely $r_3/r_2 = 1.04$ and $r_3/r_2 = 1.14$. The smaller gap of $r_3/r_2 = 1.04$ equates to $r_3 - r_2 = 5.4\,\text{mm}$, compared to $r_3 - r_2 = 18.9\,\text{mm}$ for a ratio of $r_3/r_2 = 1.14$. Ziegler (2003) recommend that both radial gaps be used for CFD investigation.

When attempting to model such a small gap (5.4 mm) using FINE™/Turbo, the manual (FINE™/Turbo Manual, 2010) suggests using the *"Non Reflecting 1D"* approach for the rotor-stator (R-S) interface. This is not an ideal solution as it cannot be used when the flow perpendicular to the interface is supersonic (FINE™/Turbo Manual, 2010), which might have been the case with the DEEP prototype.

Although the $\beta_3 = 19.8075°$ and $r_3/r_2 = 1.14$ combination does not include steady probe measurements at 2M, the only other available radial gap was

$r_3/r_2 = 1.18$, which provides much less experimental data. Steady probe measurements for $r_3/r_2 = 1.18$ at 2M can be used for comparison, keeping in mind that the 1-D theory uses a marching method in solving the vaneless annular passage, thus 1-D results are not influenced by the radial gap. The chosen radial gap of $r_3 - r_2 = 18.9\,\text{mm}$ is also similar to the 19 mm of the DEEP prototype.

Grid convergence for the radial length of the 1-D vaneless annular passage analysis again indicated that a CV length of 10 µm in both vaneless passages showed little difference compared to smaller CV lengths.

The 3-D hub, shroud and blade geometry was supplied on the test case CD-ROM in a text file with 11 spanwise sections. The bell-mouth inlet and volute sections were not modelled and the outlet was lengthened and pinched. Meshing results using AutoGrid5™ v8.7-2 can be viewed in Appendix C.2. The resulting mesh contained 2 204 864 grid points of which 997 865 grid points were in the impeller and 1 206 999 grid points were in the diffuser section. Even though the data set of $\beta_3 = 19.8075°$ and $r_3/r_2 = 1.14$ was chosen to avoid using the *"Non Reflecting 1D"* approach at the R-S interface, convergence difficulties were experienced using other R-S interface approaches. Thus the *"Non Reflecting 1D"* R-S interface was used and the results were inspected for supersonic flow at the R-S interface. The absolute and relative Mach numbers were below unity.

The information needed for 1-D modelling of the Radiver test case is supplied in Tables 3.7 and 3.8. The vaned diffuser throat area (A_{th}) is 4.405×10^3 mm^2, the perimeter (peri_{th}) is 1.304 m, the throat width (h_{th}) is 17.25 mm, the vane length (L_B) is 183.69 mm and the diffuser contained 23 vanes (z_D).

Ziegler *et al.* (2003*c*) tested the compressor in a closed loop system which allowed for a variation in inlet pressure and temperature. Air was used as flow medium. Ziegler (2003) provide observations and recommendations for a CFD analysis of the test case, of which one is that the inlet pressure and temperature during testing was lower than the standard inlet conditions of $T_{INA} = 288.15\,\text{K}$ and $p_{INA} = 1.013\,\text{bar}$. The results were scaled, similar to the O-Rotor, from the measured $T_{t,1} \approx 296\,\text{K}$ and $p_{t,1} \approx 0.6\,\text{bar}$ to the standard inlet conditions. More exact values are provided in the L2F data sets included in the Radiver CD-ROM, but Ziegler (2003) recommend using the above mentioned values consistently for all calculations.

These lower values should also be used as proposed by Ziegler (2003) to account for the Reynolds number effect discussed in Section 2.3.4. All modelling results should then be scaled using Equations (3.3.1) to (3.3.5) (Ziegler *et al.*, 2003*c*) as the same was done for the experimental results. No correction needs to be applied for the values of Ma, α, s, C_p and κ.

$$p_{t,corr} = p_t \frac{p_{INA}}{p_{t,1}} \quad \text{and} \quad p_{corr} = p \frac{p_{INA}}{p_{t,1}} \quad \text{for pressure} \tag{3.3.1}$$

Table 3.7: Impeller geometry of the Radiver test case (Ziegler *et al.*, 2003*c*).

	Inlet	Throat	Tip
r_h (mm)	30		
b (mm)	42.9		11.1
r (mm)	55.74	55.74	135
β_h	62.42°		
β	41.36°	50.04°	53.36°
β_s	33.85°		
α_C	2.46°		88.28°
κ_m (rad/m)	6.22		
t_b (mm)	0.92		1.68
A (mm^2)		9.4372×10^3	
peri (m)		1.701	
z	15		15
		Overall	
L_B (mm)		139.19	
L_{FB} (mm)		122.77	
s_{CL} and s_D (mm)		0.585	

Table 3.8: Vaned diffuser geometry of the Radiver test case (Ziegler *et al.*, 2003*c*).

	r (mm)	b (mm)	β	t_b (mm)
Inlet	135	11.1	19.97°	0.45
Discharge	277.62	11.1	58.35°	24.69

$$T_{t,corr} = T_t \frac{T_{INA}}{T_{t,1}} \quad \text{and} \quad T_{corr} = T \frac{T_{INA}}{T_{t,1}} \quad \text{for temperature} \tag{3.3.2}$$

$$\rho_{corr} = \rho \frac{p_{INA}}{p_{t,1}} \frac{T_{t,1}}{T_{INA}} \quad \text{for density} \tag{3.3.3}$$

$$C_{corr} = C \sqrt{\frac{T_{INA}}{T_{t,1}}} \quad \text{for velocity} \tag{3.3.4}$$

$$h_{t,corr} = h_t \frac{T_{INA}}{T_{t,1}} \quad \text{and} \quad h_{corr} = h \frac{T_{INA}}{T_{t,1}} \quad \text{for enthalpy} \tag{3.3.5}$$

With a deviation in inlet conditions, the mass flow rate and rotational speed need to be scaled as well using Equations (3.3.6) and (3.3.7) (Ziegler *et al.*, 2003*c*). According to Ziegler *et al.* (2003*c*), the corrected rotational speed (ω_{corr}) is always in relation to the maximum test speed ($\omega_{max} = 35\,200$ RPM) in the form $\omega_{corr}/\omega_{max}$.

$$\dot{m}_{corr} = \dot{m}\frac{p_{INA}}{p_{t,1}}\sqrt{\frac{T_{t,1}}{T_{INA}}} \quad \text{for mass flow} \tag{3.3.6}$$

$$\omega_{corr} = \omega\sqrt{\frac{T_{INA}}{T_{t,1}}} \quad \text{for rotational speed} \tag{3.3.7}$$

With the inlet conditions fixed, Ziegler (2003) recommend a rotational speed of 80 % of the maximum tested speed, i.e. $\omega_{corr}/\omega_{max} = 0.8$. Most of the measurements were conducted at this speed and after scaling this equates to $\omega = 28\,541$ RPM.

The measured mass flow rates and impeller rotational speed was used for the 1-D analysis. The 3-D modelled corrected mass flow rate range was $1.763\,\text{kg/s} \leq \dot{m}_{corr} \leq 2.1626\,\text{kg/s}$ and this was obtained by imposing the static pressure on the outlet in the range of $118\,\text{kPa} \leq p \leq 155\,\text{kPa}$. Convergence difficulties were experienced in the 3-D model when imposing the mass flow rate. This could be attributed to the occurrence of separation on the diffuser vane trailing edge, even though the outlet was pinched.

3.3.2 Modelling Results and Discussion

Ziegler *et al.* (2003*c*) report $\dot{m}_{corr} = 1.822\,\text{kg/s}$ (point P1) as the best operating point of the compressor, but notes that it is close to the observed stall limit. The choke limit is reached at $\dot{m}_{corr} = 2.164\,\text{kg/s}$ (point S2). The static-to-static pressure ratio of the diffuser stage ($PR_{SS,2M-7M}$) is shown in Figure 3.15 and the compressor total-to-total efficiency ($\eta_{TT,1M-8M}$) is shown in Figure 3.16. The calculation of $\eta_{TT,1M-8M}$ is identical to that of Equation (3.2.2) (Eckardt, 1975).

The 1-D results for $PR_{SS,2M-7M}$ show good agreement closer to S2, but a plateau is reached from P1 up to $\pm 2\,\text{kg/s}$. At P1, the error in the 1-D result is 3.78 % which is regarded as good despite the plateau. 3-D results for $PR_{SS,2M-7M}$ show good agreement with the experimental results, following the trend well. Underestimation of results for a greater part of the curve is found and the error in the 3-D results at P1 is 0.49 %.

Both the 1-D and 3-D results for $\eta_{TT,1M-8M}$ show good correlation with the experimental results. The 1-D results diverge less than the 3-D results at point S2, with the 3-D results following the experimental trend better than the 1-D results. At P1, the 1-D model underestimates $\eta_{TT,1M-8M}$ by 1.72 % and the 3-D model overestimates $\eta_{TT,1M-8M}$ by 0.69 %. With close correlation in the region $P1 \lesssim \dot{m}_{corr} \lesssim 1.95\,\text{kg/s}$, divergence closer to S2 is of lesser importance.

Static pressure results at measuring plane 2M (p_{2M}) are given in Figure 3.17. Both the 1-D and 3-D models show fair agreement with the experimental results, with the 3-D predictions following the experimental trend well. The 1-D model has a smaller error at P1 of 1.2 % (2.35 kPa) than the 3-D

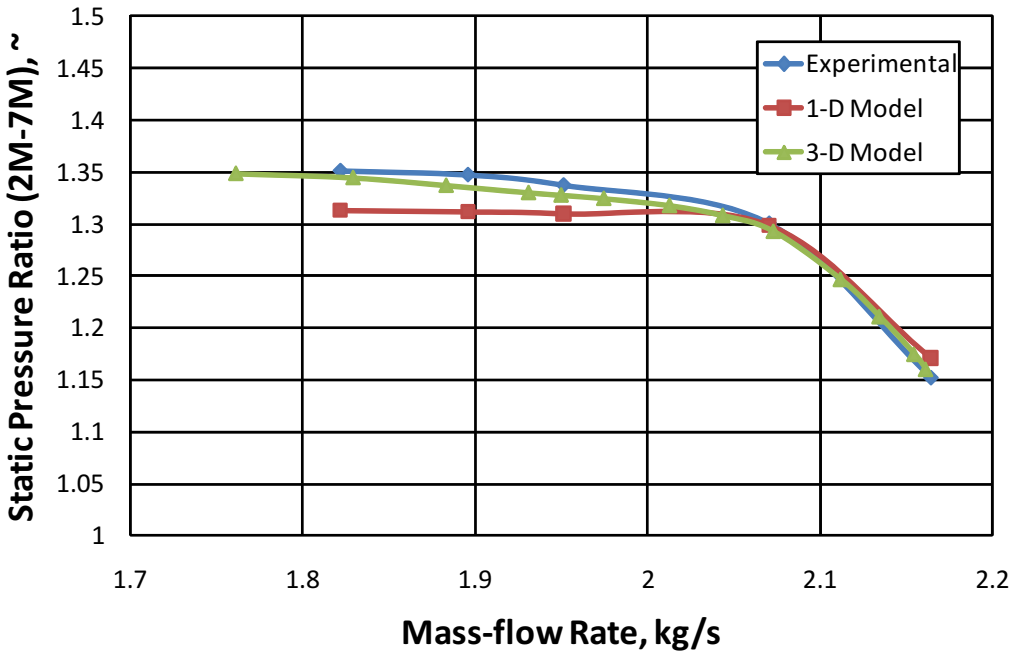

Figure 3.15: Diffuser static-to-static pressure ratio of the Radiver test case (Ziegler *et al.*, 2003*c*).

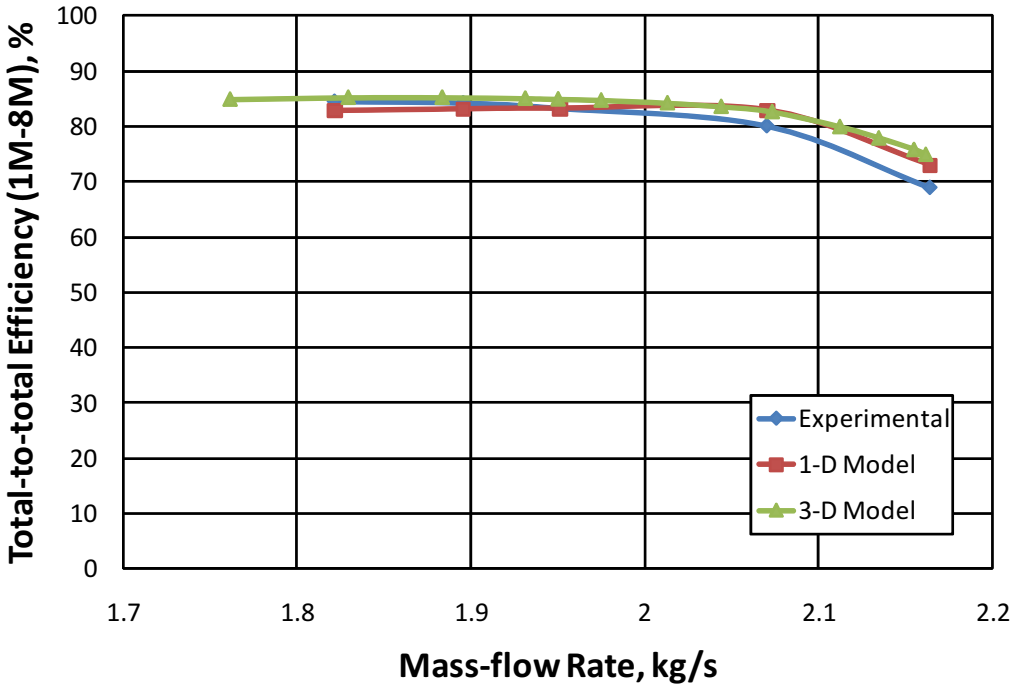

Figure 3.16: Compressor total-to-total efficiency of the Radiver test case (Ziegler *et al.*, 2003*c*).

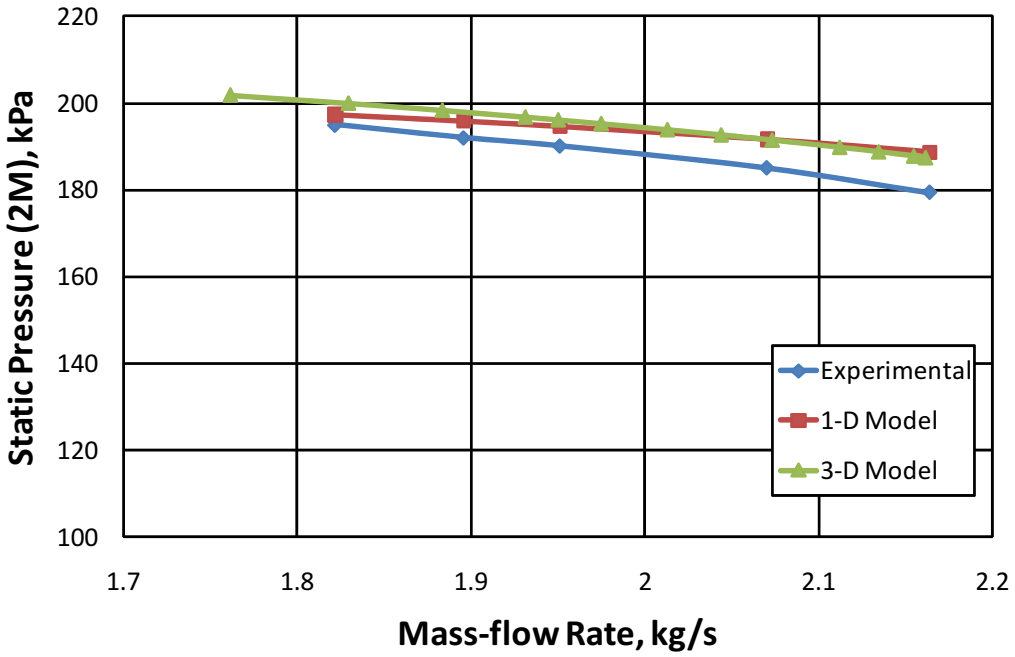

Figure 3.17: Static pressure at 2M of the Radiver test case (Ziegler *et al.*, 2003*c*).

model, which has an error of 2.56 % (4.99 kPa). Both models diverge closer to point S2 where the error in the 1-D result is 5.2 % (9.34 kPa) and the error in the 3-D result is 4.47 % (8.02 kPa).

Even though Ziegler *et al.* (2003*c*) did not take total pressure measurements at measurement plane 2M ($p_{t,2M}$) for $\beta_3 = 19.8075°$ and $r_3/r_2 = 1.14$, probe measurements were taken for $r_3/r_2 = 1.04$ and 1.18. Due to the 1-D theory using a marching step method in the vaneless annular passage analysis, the value of r_3/r_2 does not play a role when considering upstream results. Thus, comments can be made regarding results for $p_{t,2M}$, which are shown in Figure 3.18.

Both the 1-D and 3-D results show close correlation with the experimental results. The 3-D model results follow the experimental trend well and the 1-D model results show better agreement with a small divergence closer to the choke limit. The error in 1-D results when compared to the averaged results for $r_3/r_2 = 1.04$ and 1.18 at P1 is 0.398 % (1.14 kPa) and the error in 3-D results is 1.72 % (4.92 kPa).

Similar to the $p_{t,2M}$ measurements, Ziegler *et al.* (2003*c*) did not take absolute flow angle measurements at measurement plane 2M (α_{2M}) for $\beta_3 = 19.8075°$ and $r_3/r_2 = 1.14$, but for $r_3/r_2 = 1.04$ and 1.18. Due to the marching step method of the 1-D theory, comments can also be made of results for α_{2M}, which are shown in Figure 3.19.

Results for $r_3/r_2 = 1.04$ and 1.18 are near identical, suggesting that the

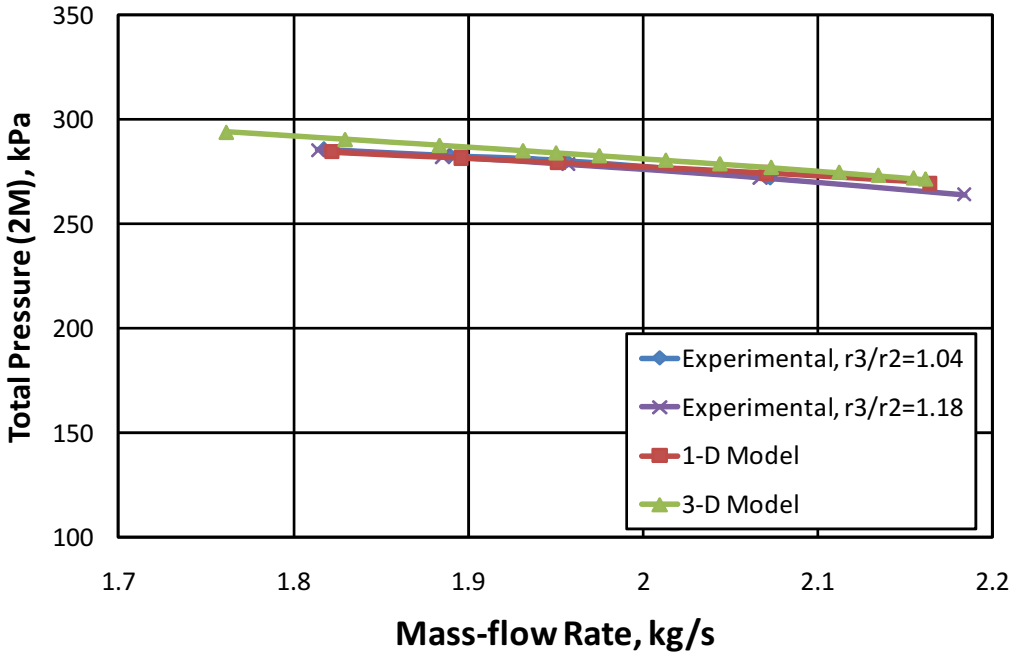

Figure 3.18: Total pressure at 2M of the Radiver test case (Ziegler *et al.*, 2003*c*).

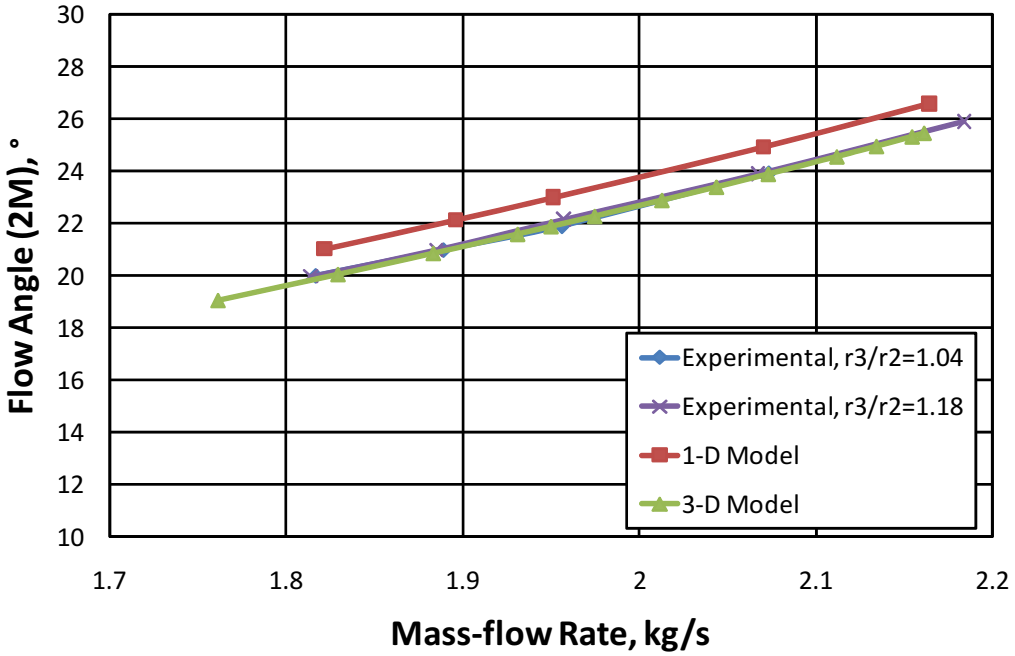

Figure 3.19: Flow angle at 2M of the Radiver test case (Ziegler *et al.*, 2003*c*).

radius ratio does not influence upstream results significantly. The 3-D model does seem to provide better results by underestimating with a difference at P1 of 0.05° compared to the 1-D model with an overestimated difference of 1.04° (when compared to the averaged results for $r_3/r_2 = 1.04$ and 1.18). But as previously mentioned, the probe measurement results tended to be more tangential than the L2F measurements by roughly 2°. Taking this error into account, the 1-D model provides better results by underestimating with a difference of 0.96° compared by the 3-D model underestimating by 1.95°. But results of both models are considered good.

During meshing of the 3-D model, the R-S interface in AutoGrid5™ was specified at the radius of measuring plane 2M to simplify post-processing, as flow conditions at the R-S interface are readily accessible through a text file created during simulation. This was not the best solution, due to the averaging method applied at the R-S interface during simulation having an influence on the results. A better solution would be to place the R-S interface slightly downstream of 2M and creating a cutting plane on the radius of 2M for averaging.

Absolute Mach number results at measuring plane 7M (Ma_{7M}) are shown in Figure 3.20. The 1-D model largely underestimates the results over the entire mass flow rate range and the difference at P1 is 0.04. The 3-D prediction does not follow the experimental trend but still provides good correlation, with a small difference of 0.01. The difference in 1-D result at S2 is 0.16, with the 3-D result difference being 0.03.

The larger error in Ma_{7M} of the 1-D results can be attributed to the vane discharge thickness playing a too large role in determining the change in flow area from the vane discharge to the first CV of the 1-D vaneless annular passage theory. With a sudden increase in area, mathematically the meridional velocity (C_m) decreases just as rapidly. With a decrease in C_m, the absolute velocity and hence absolute Mach number decreases. But the full flow area is not utilised in reality, with separation at the discharge decreasing the effective flow area.

In the vaneless annular passage after the vaned diffuser, the 1-D analysis for S2 shows a sudden decrease in Ma_{7M} from 0.26 to 0.21, a difference of 0.05, for the first CV. If this difference is added to Figure 3.20, the difference in the 1-D result at S2 reduces to 0.11. If the same argument is followed for P1, the decrease over the first CV is 0.03. This decreases the difference in the 1-D result to 0.01, which is a significant improvement.

Total pressure results at measuring station 7M ($p_{t,7M}$) are shown in Figure 3.21 and both models show good correlation with the experimental results. The 1-D model underestimates the experimental result at P1 by 2.62 % (7.08 kPa) and the 3-D model overestimates by 2.48 % (6.71 kPa), following the experimental trend better than the 1-D model.

The 1-D analysis did not report flow abnormalities in the impeller or vaneless annular passage and this was confirmed by inspection of the 3-D results

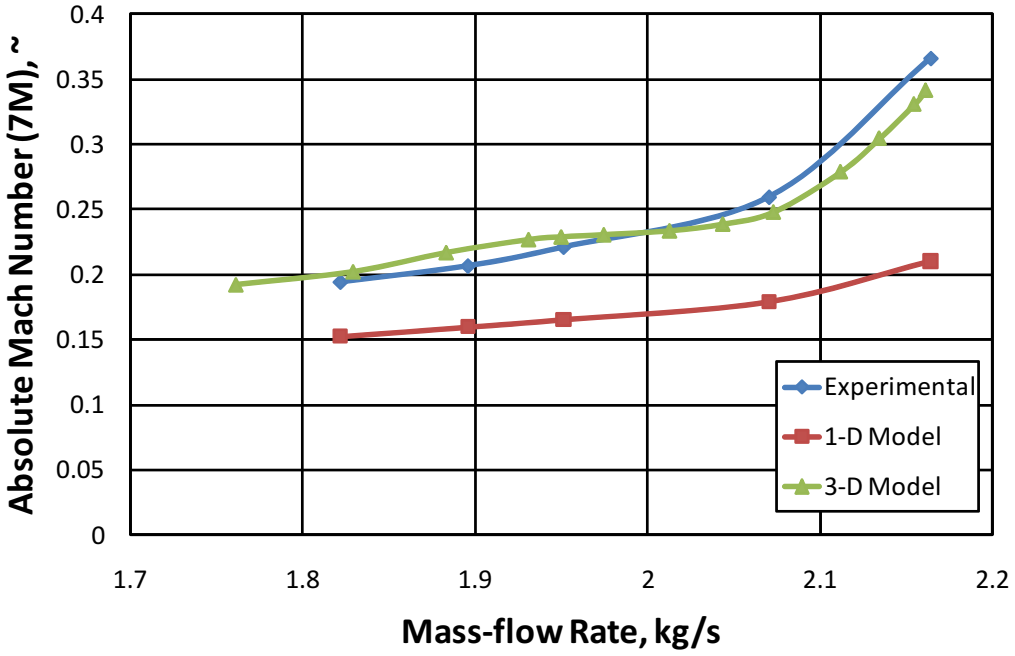

Figure 3.20: Absolute Mach number at 7M of the Radiver test case (Ziegler *et al.*, 2003*c*).

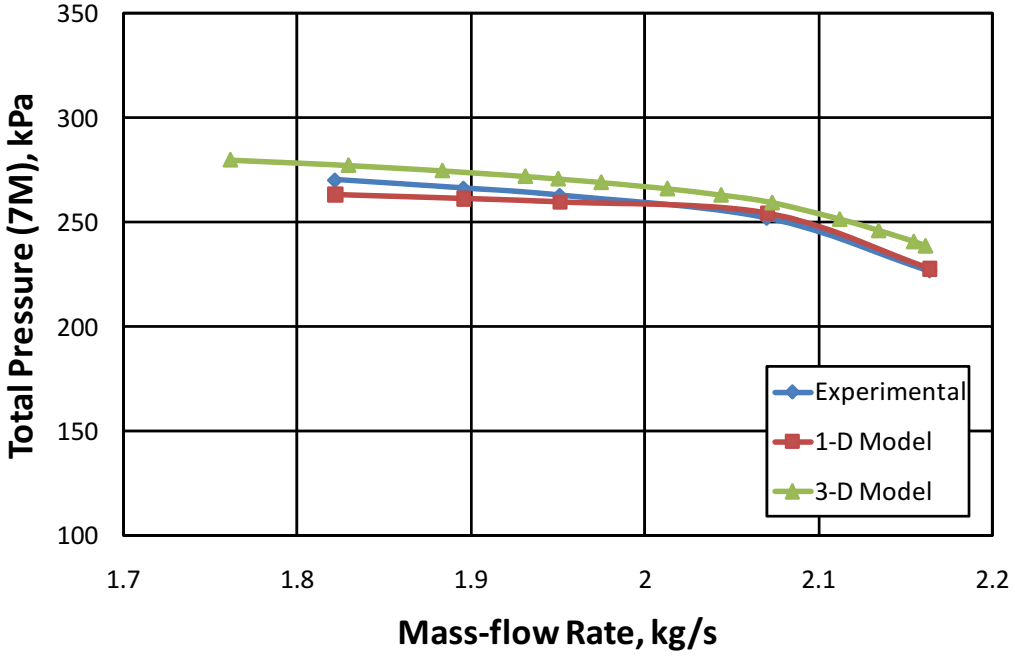

Figure 3.21: Total pressure at 7M of the Radiver test case (Ziegler *et al.*, 2003*c*).

using CFView™. Separation in the vaned diffuser was predicted for the two higher mass flow rates, $\dot{m}_{corr} = 2.07\,\text{kg/s}$ and $2.164\,\text{kg/s}$. Separation is expected when $C_4 \geq C_{SEP}$ where C_{SEP} is determined in Equation (B.2.19) using the absolute inlet velocity (C_3) and indirectly using the diffuser divergence angle ($2\theta_C$). Visually this occurrence is represented by a low absolute velocity region along the diffuser vane surface, resulting in a smaller effective flow area.

CFView™ was used to investigate separation along the diffuser vane of the 3-D model and the results are shown in Figure 3.22. Some separation is observable in Figure 3.22a (at approximately point P1) and the 1-D analysis reports absence of separation with $C_{SEP} = 84.5\,\text{m/s}$ and $C_4 = 76.4\,\text{m/s}$. For Figure 3.22b, the 1-D analysis returned $C_{SEP} = 83.88\,\text{m/s}$ and $C_4 = 82.6\,\text{m/s}$, which just avoids the separation criterion. This could explain the observation of the onset of separation along the vane suction surface.

Even though some separation is observable in Figure 3.22a, the thickness of the separation layer at the vane discharge is smaller than that of Figure 3.22b. Separation is visible in Figure 3.22c with a significant reduction in effective flow area at the vane discharge, observable with a region of high absolute velocity magnitude ($180\,\text{m/s} < C < 260\,\text{m/s}$) on the vane pressure side near the discharge. Separation at the vane leading edge is also observable. The 1-D analysis returned $C_4 = 104.13\,\text{m/s}$ and C_{SEP} was $82.91\,\text{m/s}$, which is significantly lower than C_4.

3.4 Discussion of the Modelling Methods

The 1-D analysis method consists of three sub-routines, namely one each for the impeller, vaneless annular passage and the vaned diffuser. The analysis was performed sequentially from impeller inlet to volute inlet and results obtained from downstream components can not affect the upstream component results using the 1-D approach. The inverse is true, where if erroneous results were obtained from upstream components, the error is transferred to the subsequent component analysis which then ultimately has a negative impact on the overall performance prediction results. The 3-D method suffers less from this phenomenon as the entire discretised domain is solved, with adjacent cells influencing each other, until satisfactory convergence is achieved.

Both test case compressors can be described as "smooth running", with the exception of impeller blade and inducer stall on the O-Rotor test case and vane separation occurring in the vaned diffuser of the Radiver test case. Focusing on the impeller 1-D theory, when applied on the O-Rotor test case, the degree of impeller blade stall was minimal even though it occurred over a larger portion of the operating range, as depicted in Figure 3.11. The effect of separation is reflected in the overall performance results in Figures 3.5 and 3.6, where divergence from the experimental results by the 1-D results closer to the stall limit is observed. In these same figures, the 3-D model results show good

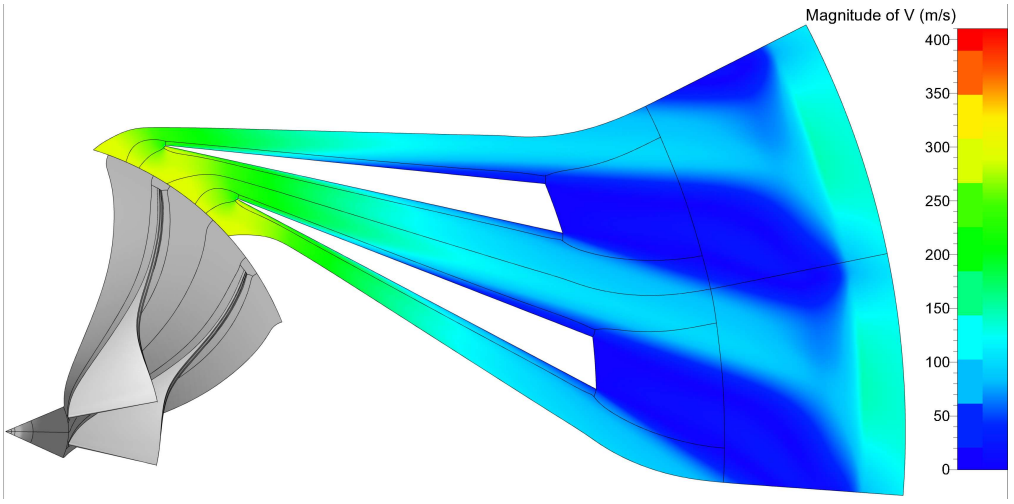

(a) $\dot{m}_{corr} = \pm 1.83\,\mathrm{kg/s}$ with $C_4 < C_{SEP}$.

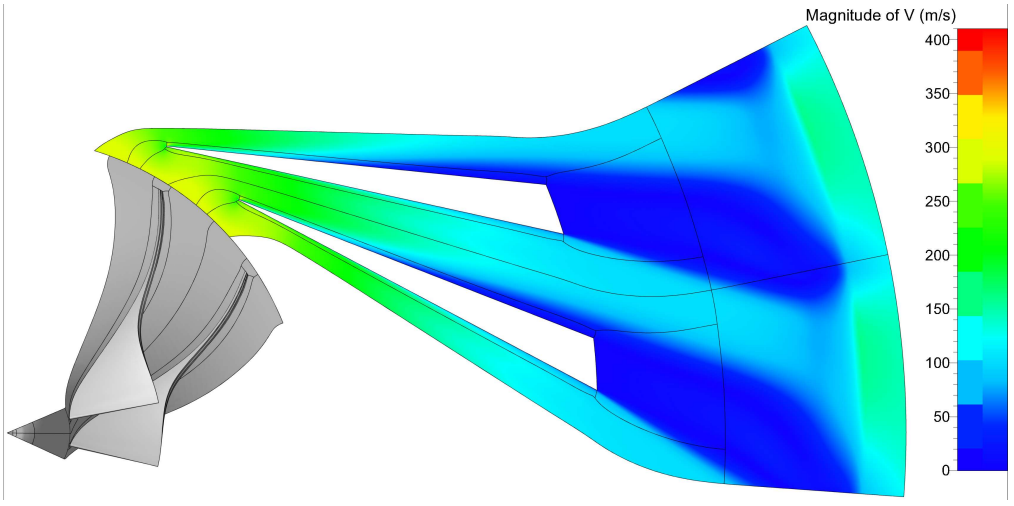

(b) $\dot{m}_{corr} = \pm 1.95\,\mathrm{kg/s}$ with $C_4 \approx C_{SEP}$.

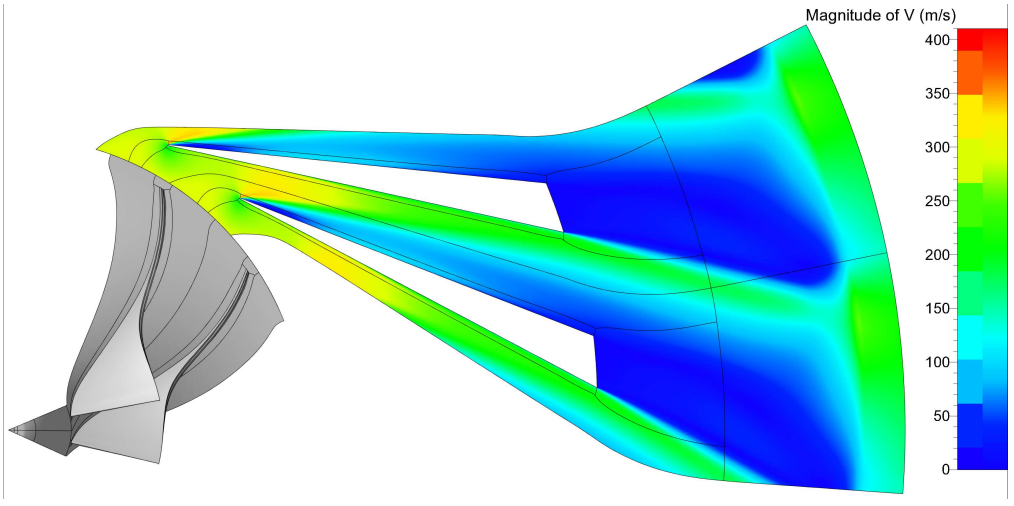

(c) $\dot{m}_{corr} = \pm 2.161\,\mathrm{kg/s}$ with $C_4 > C_{SEP}$.

Figure 3.22: Absolute velocity magnitude along the Radiver diffuser vane at $\omega_{corr}/\omega_{max} = 0.8$ and 50 % span.

agreement with the experimental results. Impeller tip 1-D and 3-D results at the operating point (where minimal impeller blade stall is predicted by the 1-D theory) in Table 3.5 are regarded as very good with a low error.

When the impeller 1-D theory was applied to the Radiver test case, no flow abnormalities were predicted. The impeller tip 1-D static pressure range shown in Figure 3.17 shows fair correlation with divergence closer to the choke limit. The 3-D model results follow the experimental trend better with fair correlation. Impeller tip total pressure results of both the 1-D and 3-D models shown in Figure 3.18 indicate good correlation with the experimental results. Furthermore, 1-D and 3-D impeller tip flow angle results in Figure 3.19 show good and excellent agreement with the experimental results respectively.

Considering the impeller results obtained for the two test cases, the conclusion can be drawn that the 1-D impeller theory provides adequate results whilst the impeller is in a stable operating environment. Once stall or choke is predicted, the impeller loss coefficients do not capture the detrimental effects on performance effectively. In comparison, the 3-D modelling method provides better correlation with the experimental results in instances where the 1-D model predicts stall or choke.

Examining results obtained from the 1-D vaneless annular passage theory, the total and static pressure results obtained for the O-Rotor in Figure 3.7 show a larger error than the 3-D results. Both the 1-D and 3-D theory results follow the total pressure experimental trend with the 1-D static pressure diverging from the experimental results closer to the discharge. This error can be attributed to the control volume (CV) length used in the 1-D vaneless annular passage theory being too small. No suggestion on a preferred CV length could be found in the relevant literature [Johnston and Dean (1966), Aungier (1993) and Aungier (2000)], thus the author chose to decrease the CV length until the discharge values showed little change compared to the previous CV length results. This led to a CV length of 10 µm, resulting in 20 000 cells for the vaneless annular passage in the O-Rotor.

Initial 1-D simulation results of the O-Rotor 1-D vaneless annular passage with a rough grid, i.e. 10 cells, showed better correlation with the experimental results. With an increase in the number of CVs, the overall error increased until grid convergence was achieved. The marching step method can transfer any inherent error in 1-D results of an upstream CV to a downstream CV. Taking into account that the original theory by Johnston and Dean was published in 1966, implemented by Aungier in 1993 and that the theory by Aungier (2000) was meant to be implemented on a personal computer at the time, a CV length of 10 µm would be unrealistically small and computationally too intensive.

The O-Rotor vaneless annular passage 3-D model results showed better correlation with the experimental results of Figures 3.7 and 3.8. From this it can be deduced that the 3-D modelling method does not suffer from the same phenomenon of transferring the error downstream as found with the

1-D vaneless annular passage theory. This can be attributed to the entire discretised 3-D domain being solved until satisfactory convergence is achieved.

Vaned diffuser experimental results are limited to the Radiver test case only. When the 1-D vaned diffuser theory was applied to the Radiver test case, vaned diffuser separation was predicted from $\dot{m}_{corr} = 2.07\,\text{kg/s}$ to $2.164\,\text{kg/s}$. The degree of separation is noticeable close to the choke margin according to the decision criterion, as shown in Figure 3.22. As discussed previously, the visual 3-D results regarding vane separation correlates with the 1-D theory predictions. Successful prediction of vaned diffuser stall is required to investigate the DEEP prototype's suspected underperforming diffuser.

Conclusions regarding the vaned diffuser 1-D theory has to take into account that errors in upstream results influence the vaned diffuser theory results. Thus the vaned diffuser 1-D results preferably needs to be assessed between the vane leading edge and discharge. Such an example is the diffuser static pressure ratio shown in Figure 3.15, where the 1-D results show good correlation with the experimental results. Excellent correlation is found closer to the choke margin where vaned stall is predicted. This is also the region where the impeller 1-D theory tip static pressure results are observed to diverge from the experimental results. The 3-D model shows better correlation with the experimental results than the 1-D theory, but both models perform well.

The Radiver test case includes a second vaneless annular passage after the vaned diffuser. As mentioned previously, the sudden increase in flow area due to the vane thickness at the discharge is not accounted for by the 1-D theory. This is represented by the lower absolute Mach number at measurement station 7M shown in Figure 3.20. Total pressure 1-D results in Figure 3.21 show good correlation with the experimental results, but this can be attributed to the total pressure mainly being influenced by friction losses which in turn is influenced by the Reynolds number. Thus the 1-D total pressure results are not influenced directly by the sudden increase in flow area. The 3-D model provides similar good results in the vaneless annular passage after the vaned diffuser.

Overall compressor performance results for the Radiver test case are given in Figure 3.16, which shows the compressor total-to-total efficiency. Both the 1-D and 3-D modelling methods provide similarly good results with a deviation in the impeller 1-D results close to the choke margin being observed.

Taking the preceding discussions into account, the 1-D and 3-D modelling methods provide good results for the test cases and is fit for investigating the DEEP prototype. The 1-D theory provides the best results when the compressor is in a stable operating range, with the 3-D modelling method still providing good results even if outside the stable operating range. The 1-D model provides a quick solution, but the results should be investigated once stall or choke is predicted. The vaneless annular passage 1-D results should also be investigated if implemented over a long diffuser.

Chapter 4

DEEP Prototype Information and Modelling Results

The prototype compressor developed during the DEEP project is discussed and analysed in this section. A photo of the manufactured prototype impeller is shown in Figure 4.1, but a photo of the vaned diffuser was not available.

Van der Spuy (2003) designed two prototypes using Concepts NREC's COMPAL™ and CCAD™ software, of which the first prototype was sent to Concepts NREC for review. Technical feedback was to consider a wedge type diffuser, that the impeller exducer was overloaded and the inducer underloaded. Geometric modifications regarding the blade geometry (introduce

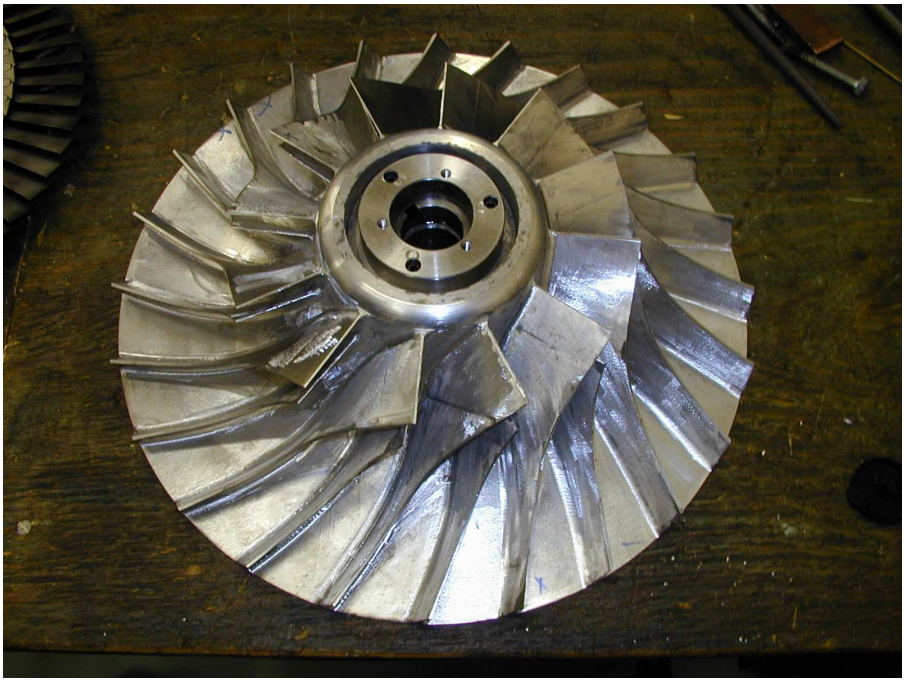

Figure 4.1: The DEEP impeller (Van der Spuy, 2003).

blade tip backsweep and include blade lean and splitter blades) was proposed and that the vaneless annular passage be parallel-walled and not diverging. Inserting a short vaneless annular passage between the vaned diffuser and volute should also be considered.

Taking this advice into account, Van der Spuy (2003) elected to use the second prototype. The DEEP prototype impeller included splitter blades in the design and the blades were backswept at the tip. A short, converging (the hub profile has a constant axial coordinate) vaneless annular passage connected the impeller tip and vaned diffuser inlet. The vaned diffuser implemented a patented Concepts ETI™ flat plate vane (CETI (FP) 06) and the shroud end-wall resulted in a diverging vaned diffuser up to the vane discharge. A short, parallel-walled vaneless annular passage connected the vaned diffuser discharge to the existing dual-exit volute, visible in Figure 2.4.

Deviation from the advice provided by Concepts NREC included the diffuser vane profile and the vaned diffuser end-walls. Van der Spuy (2003) conducted numerous analyses with wedge and "NACA" profiles, but the widest operating range (stall to choke margins) was predicted by the CETI profile. Furthermore, Van der Spuy (2003) found that a limited amount of wall divergence in the vaned diffuser section aided matching of the re-designed diffuser section to the existing volute.

4.1 Geometry and Known Performance Characteristics

A 3-D IGES computer model of the compressor impeller and diffuser sections was included on a CD-ROM which was obtained from the DEEP authors (Van der Spuy, 2003). This model was used to extract the hub and shroud curves as well as hub-to-shroud sections for meshing with AutoGrid5™ v8.7-2. The dual-exit volute was not included in the 3-D model and the outlet was again lengthened and pinched. The resulting mesh contained 2 634 405 grid points of which 1 544 451 grid points were in the impeller and 1 089 954 grid points were in the diffuser. Meshing results of the DEEP prototype are supplied in Appendix C.3. A *"Full Non Matching Mixing Plane"* was used at the R-S interface. This interface approach respects an exact conservation of mass flow, momentum and energy through the R-S interface, but has relaxed constraints on the interface geometry (FINE™/Turbo Manual, 2010).

Measurement stations for comparison between the 1-D and 3-D results were chosen along the fluid path in the compressor, namely the impeller blade leading edge (station A) and tip (station B), the vaned diffuser vane leading edge (station C) and the vaneless annular passage discharge to the volute (station D). To visualise the DEEP prototype with measurement stations, the unmeshed 3-D model is supplied in Figure 4.2 and the AutoGrid5™ meridional

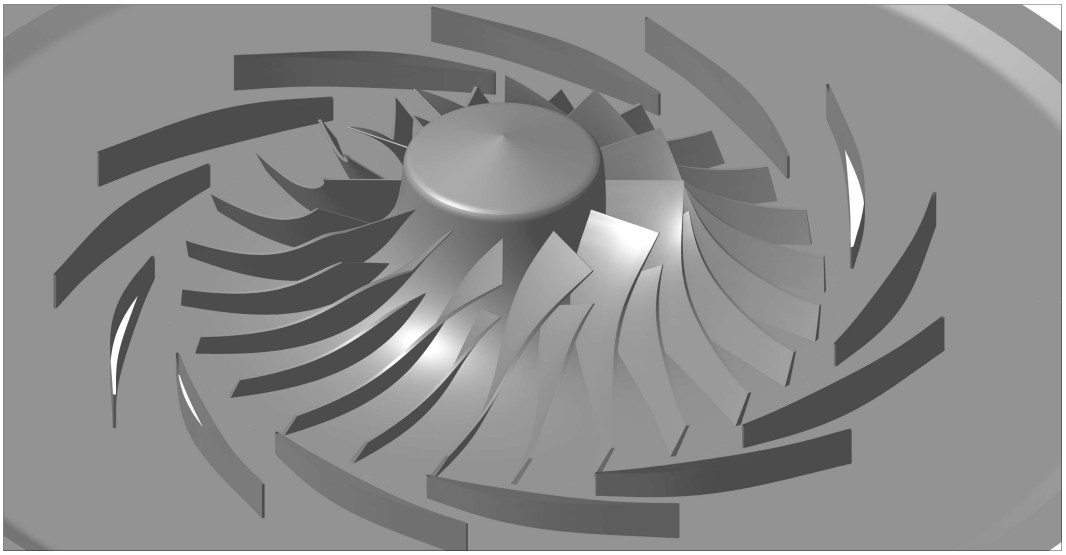

Figure 4.2: Unmeshed 3-D model of the DEEP compressor.

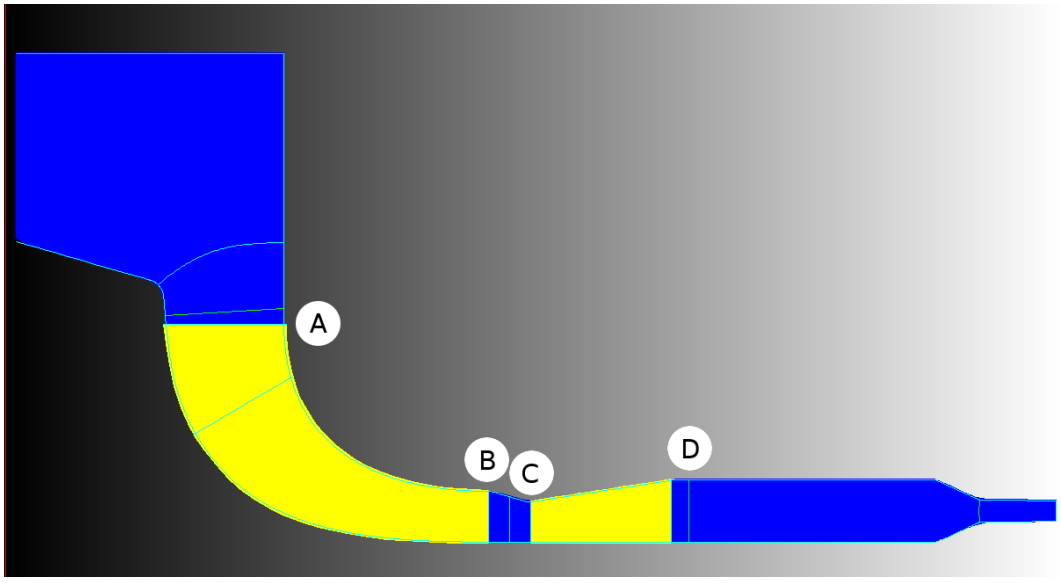

Figure 4.3: AutoGrid5™ meridional view of the DEEP compressor.

view in Figure 4.3.

The necessary 1-D geometric information was extracted from the 3-D model using IGG™ and is shown in Tables 4.1 and 4.2. The vaned diffuser throat area (A_{th}) is $10.544 \times 10^3\,\text{mm}^2$, the perimeter ($\text{peri}_{th}$) is 1.562 m, the throat width (h_{th}) is 39.31 mm, the vane length (L_B) is 176.51 mm and the diffuser contained 13 vanes (z_D). The parallel-walled vaneless annular passage after the vane discharge reached the volute at $r_5 = 313\,\text{mm}$ (station D).

Similar to the O-Rotor and Radiver test cases, grid convergence for the

Table 4.1: Impeller geometry of the DEEP prototype (Van der Spuy, 2003).

	Inlet	Throat	Tip
r_h (mm)	68		
b (mm)	54		23
r (mm)	98.76	98.76	215
β_h	49.94°		
β	42.82°	49.14°	70.45°
β_s	33.44°		
α_C	1.15°		89.9°
κ_m (rad/m)	-9.63		
t_b (mm)	1.14		3.08
A (mm^2)		23.4146×10^3	
peri (m)		2.145	
z	12		24
		Overall	
L_B (mm)		190.43	
L_{FB} (mm)		165.66	
L_{SB} (mm)		129.31	
s_{CL} and s_D (mm)		1.27	

Table 4.2: Vaned diffuser geometry of the DEEP prototype (Van der Spuy, 2003).

	r (mm)	b (mm)	β	t_b (mm)
Inlet	234	18	14.35°	2.47
Discharge	300	28	29.47°	2.0

radial length of the 1-D vaneless annular passage analysis yielded a CV length of 10 µm in both vaneless passages with satisfactory difference in final output compared to smaller CV lengths.

Van der Spuy (2003) chose the compressor design point as 4.7 kg/s at 19 210 RPM with a predicted total-to-total pressure ratio (PR_{TT}) of 3.25 and total-to-total efficiency (η_{TT}) of 78 %. At compressor inlet conditions of $p_{t,1} =$ 101 kPa and $T_{t,1} = 298$ K at 19 210 RPM, the predicted mass flow range was $3.63\,\text{kg/s} \lesssim \dot{m} \lesssim 7.12\,\text{kg/s}$. Unlike the Radiver test case, the analysis results do not need to be scaled as the provided inlet conditions are those measured during testing.

The above mentioned inlet conditions and impeller speed was used for the 3-D analysis and the mass flow rate was specified at the outlet boundary with velocity scaling. The results showed that the mass flow range was between 4.25 kg/s and 5.32 kg/s, with the design point closer to the stall margin. Lower mass flow rates were calculated, but showed significant differences

between the inlet and outlet boundary mass flow rates ($\dot{m}_{inlet} = 4.8099\,\text{kg/s}$ and $\dot{m}_{outlet} = 4.25\,\text{kg/s}$; $\dot{m}_{inlet} = 4.5562\,\text{kg/s}$ and $\dot{m}_{outlet} = 4.3\,\text{kg/s}$). The differences suggested that the 3-D results of these lower mass flow rates are unreliable and were therefore excluded from the report. The 1-D analysis evaluated the compressor at the mass flow rates originally simulated in the 3-D analysis.

4.2 Modelling Results

After testing of the DEEP prototype compressor, Van der Spuy (2003) notes that the turbocharger speeds were not measured, thus a direct comparison between the experimental and theoretical results was not possible. The experimental results used the engine throttle notches as reference. Thus comments in this thesis are drawn using the 1-D and 3-D results taking the prototype geometry into account.

Van der Spuy (2003) also comments on the inception of stall at the lower than expected boost pressure. Additional testing at the time indicated that the observed stall is not taking place in the impeller inducer. The authors indicated that a possible area of concern is the diffuser section. Software used at the time of the DEEP project did not provide an indication of possible stall problems, but a large variation in predicted operating range between the flat plate and wedge diffuser blade profiles raised doubt regarding the accuracy of the software predictions.

Focusing on the DEEP prototype impeller 1-D analysis, impeller blade stall was predicted across the entire operating range of $4.25\,\text{kg/s} \leq \dot{m} \leq 5.32\,\text{kg/s}$ and inducer stall was predicted from $4.25\,\text{kg/s} \leq \dot{m} \leq 4.7\,\text{kg/s}$. Visual inspection of the 3-D results at the operating point with CFView™ confirms blade stall at the impeller blade tip, as shown in Figure 4.4. The stall criterion ($D_{eq} > 2$) was satisfied over the operating range with values for D_{eq} ranging from 2.455 to 2.67. Low relative velocity regions were also identified over approximately 50 % of the splitter blade suction surface as shown in Figure 4.5.

Leading to the vaneless annular passage after the impeller tip, the 3-D analysis predicted high absolute Mach number flow between the vane leading edge and diffuser throat suction surface at the operating point. This is shown in Figure 4.6 and was originally not suspected to be present during the DEEP project. Roughly 40 % of station C is occupied by a supersonic region with lower Mach number flow occupying the remainder of the inlet.

Area averaged absolute Mach number results at station C for the DEEP operating range are presented in Figure 4.7. The 1-D and 3-D results correlate well and follow a similar trend, with a difference at the operating point of $M_3 = 0.035$, but none of the models predict supersonic flow. The loss of information from the CFView™ 1-D results at the leading edge due to averaging is noticeable, with the averaged result at the operating point being $M_3 = 0.785$

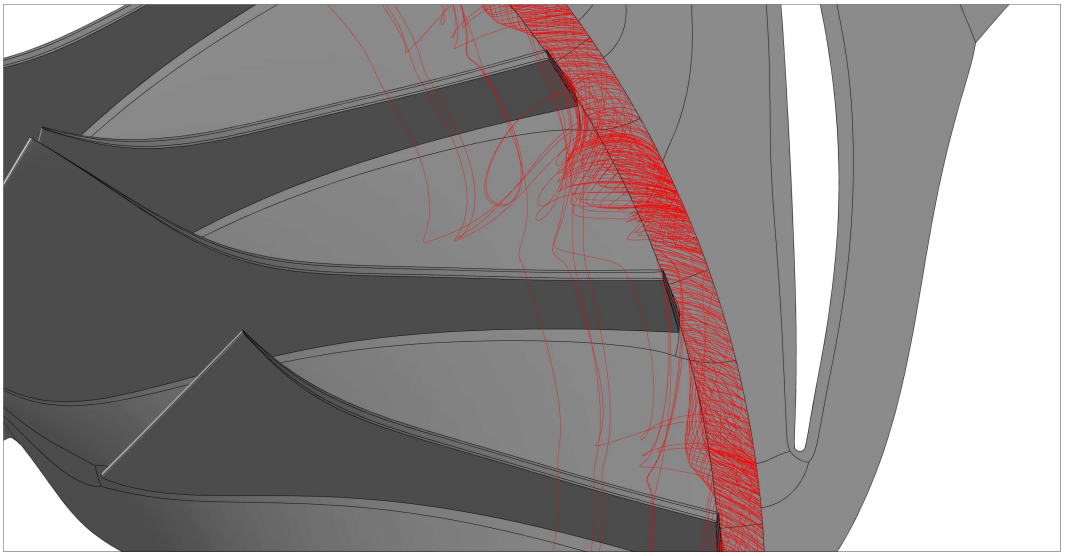

Figure 4.4: Recirculating flow ($D_{eq} = 2.573 > 2$) at the impeller tip of the DEEP prototype at 50 % span and the operating point.

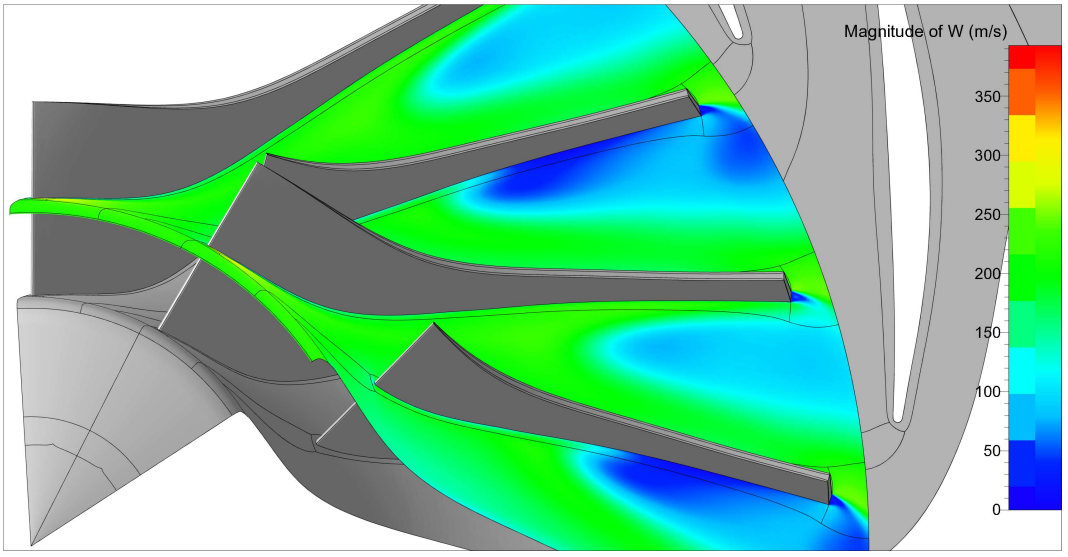

Figure 4.5: Low relative velocity regions in the DEEP prototype impeller at 50 % span and the operating point.

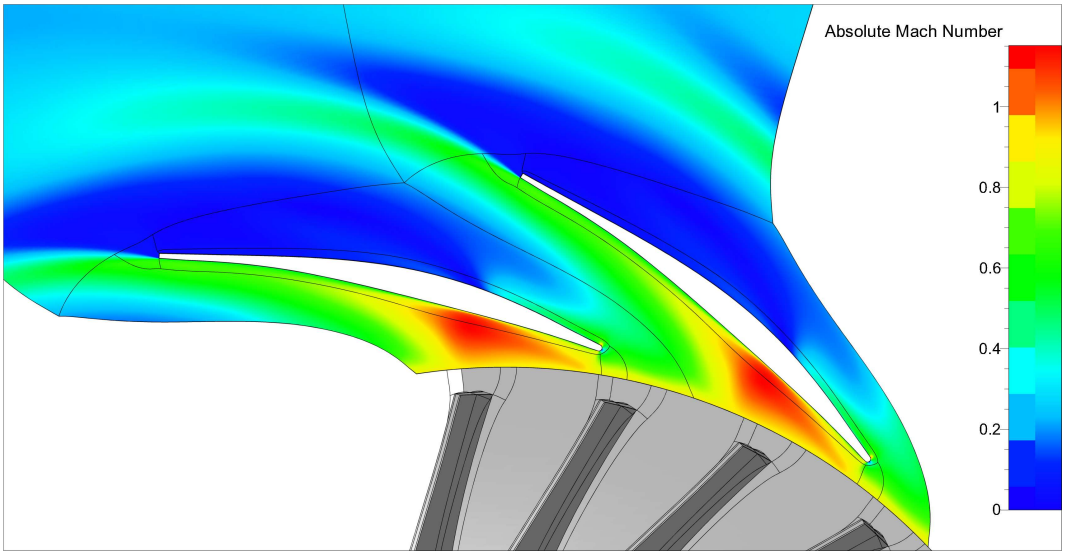

Figure 4.6: High Mach number flow between the DEEP prototype diffuser inlet and throat at 50 % span and the operating point.

and not indicating a possible high Mach number region. The 1-D results similarly will not warn about high Mach number flow between the vaned diffuser inlet and throat. This is due to the vaned diffuser analysis not examining a supersonic shock loss such as found in the impeller analysis.

The vaned diffuser 1-D analysis predicted separation over the entire DEEP operating range with the separation criterion ($C_4 > C_{SEP}$) being satisfied. Values for C_4 ranged from 74.91 m/s to 89.55 m/s and similarly for C_{SEP}, from 57.62 m/s to 57.69 m/s. 3-D results from CFView™ at the operating point show recirculation in the vector field along the vaned diffuser vane suction surface of Figure 4.8. To emphasise the degree of recirculation and separation, the absolute flow angle of the diffuser is shown in Figure 4.9.

Absolute flow angle results at station C from the 1-D and 3-D analysis across the operating range are shown in Figure 4.10. Aungier (2000) recommends a vane incidence angle (i_3) of $-1°$. To match the existing prototype impeller and vaneless annular passage leading to the vaned diffuser at the operating point, the vane leading edge angle (β_3) should be 12.2° according to the 1-D analysis and 13.9° according to the 3-D analysis, which is less than the prototype design of 14.35°. This leads to a shallower vane angle, leading to more separation on the suction surface. With this in mind, the separation might be associated with a non-optimal vane profile.

The vaned diffuser 1-D analysis furthermore gave warning of deterioration in diffuser performance due to L being larger than 1/3 and $2\theta_C$ being larger than 11°. Refer to Appendix B.2 for a description of L and $2\theta_C$. The parameter $2\theta_C > 11°$ is an indirect result of the diverging shroud in the vaned diffuser section. The non-optimal vane design is directly related to the dis-

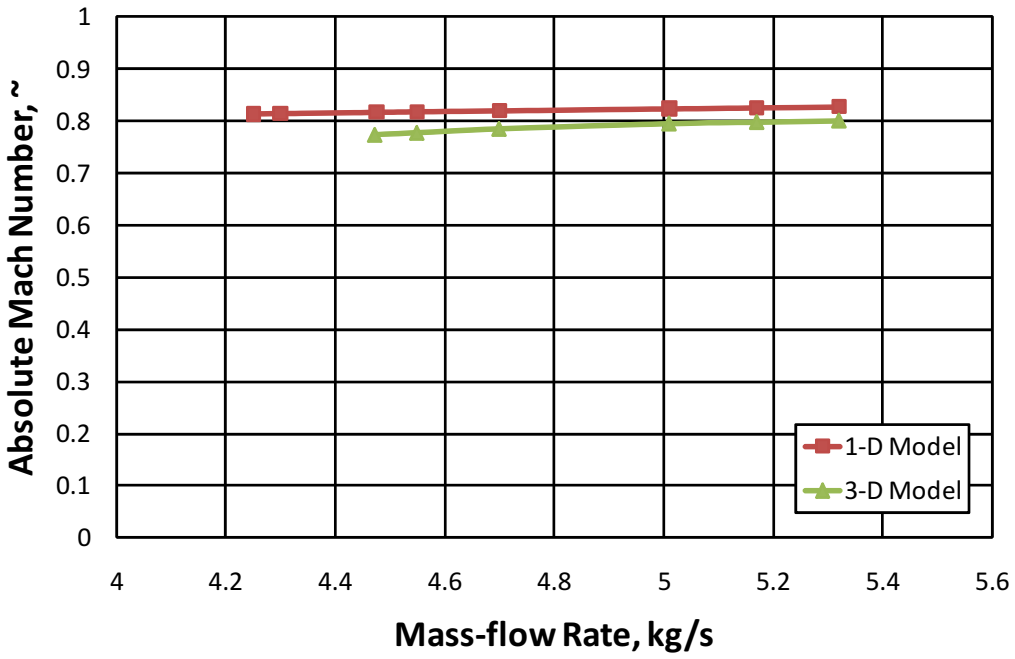

Figure 4.7: Absolute Mach Number at station C of the DEEP prototype.

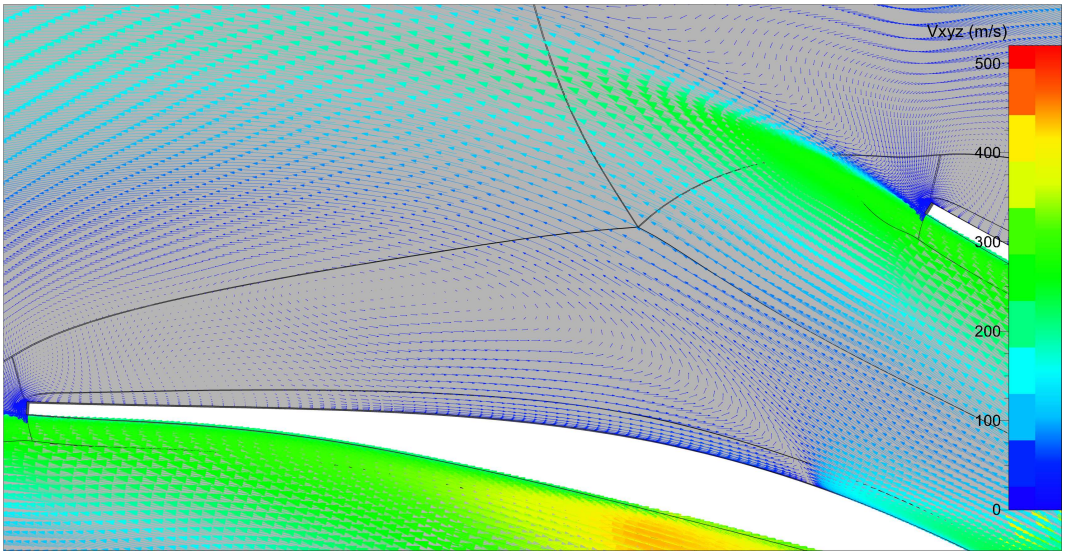

Figure 4.8: Absolute velocity flow vectors showing recirculation on the DEEP prototype diffuser vane suction surface at 50 % span and the operating point.

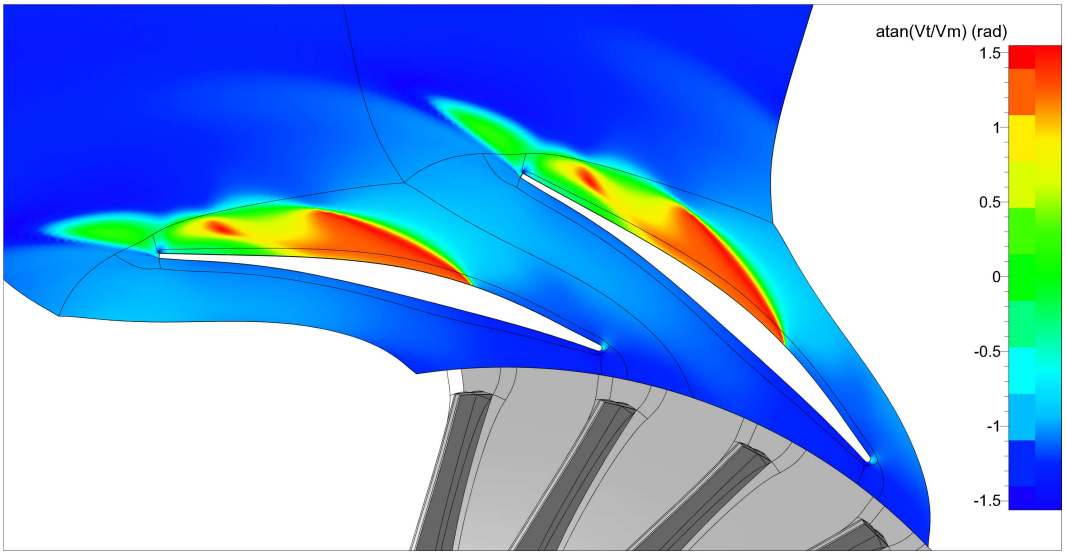

Figure 4.9: Absolute flow angle showing separation across the DEEP prototype diffuser vane at 50 % span and the operating point.

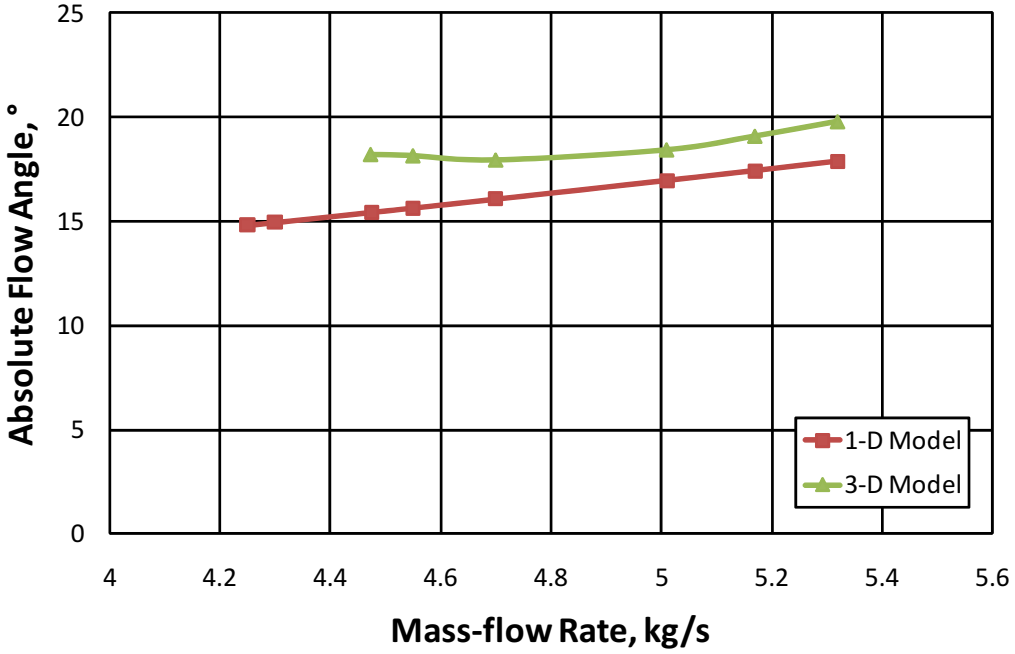

Figure 4.10: Absolute flow angle at station C of the DEEP prototype.

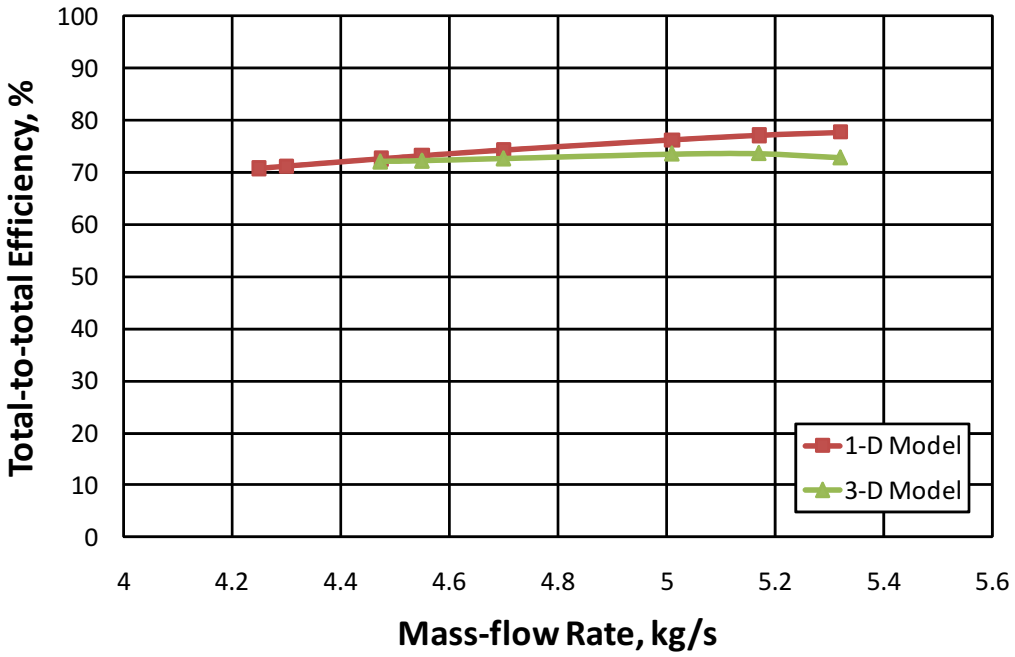

Figure 4.11: Total-to-total efficiency between stations A and D of the DEEP prototype.

charge vane angle (β_4), which also contributes to $2\theta_C$ in the formulation of the vane-to-vane arc length (w, Equation (B.2.12)). Hence, the non-optimal vane profile contributes to the deterioration in diffuser performance according to Equation (B.2.12).

Overall performance results of the DEEP compressor between point A and D are shown in Figures 4.11 and 4.12. The 1-D and 3-D modelling methods provide similar results for the total-to-total efficiency ($\eta_{TT,A-D}$), with a difference of 1.63 % at the operating point. The trends diverge closer to the choke margin, which is where the 3-D modelling method is argued to capture the choking effect better than the 1-D model.

Predictions of the total-to-total pressure ratio ($PR_{TT,A-D}$) by the 1-D and 3-D models show a similar flat trend, but with a large difference of 0.288 at the operating point. This difference can be attributed to the 1-D separation loss coefficients in the impeller and vaned diffuser not fully capturing the loss in pressure once separation is predicted. This phenomenon is discussed in Section 3.4.

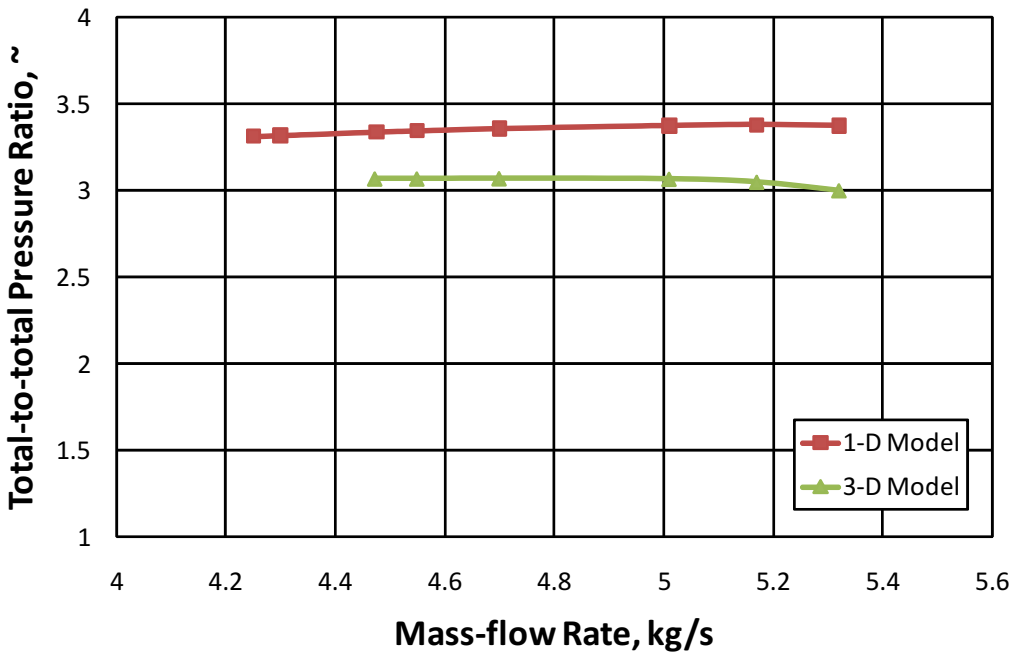

Figure 4.12: Total-to-total pressure ratio between stations A and D of the DEEP prototype.

Chapter 5

Conclusions and Recommendations

5.1 Conclusions

The 1-D model, which is based on the theory of Aungier (2000), delivers good overall compressor results as shown in Figures 3.5 and 3.6 for the O-Rotor and Figures 3.15 and 3.16 for the Radiver test case. However, the overall prediction accuracy is influenced by the compressor sub-component theory results as discussed in Section 3.4. The implemented sub-component theories are of the impeller, vaneless annular passage and a vaned diffuser.

The 1-D impeller theory provides excellent results, as shown with the O-Rotor impeller tip results in Table 3.5 and the Radiver results at station 2M in Figures 3.17 to 3.19. The 1-D impeller theory also successfully predicted recirculation at the O-Rotor impeller tip as shown in Figure 3.11, which correlates with the 3-D findings. Prediction accuracy of the 1-D impeller theory does however deteriorate once stall or choking is encountered, where the loss coefficients do not capture the effects on performance adequately.

The 1-D vaneless annular passage theory underestimates the static and total pressures when applied to the O-Rotor case, as shown in Figures 3.7 and 3.9. An explanation for this error is provided in Section 3.4, where it is argued that the CV length is much smaller than is believed to be originally intended by Aungier (2000). Small errors in CV results are passed onto the next CV in the marching step method, which results in the error increasing as the CV moves further away from the passage inlet. Results of the Radiver vaneless annular passage after the vaned diffuser discharge indicate that the sudden increase in flow area at the passage inlet is not correctly accounted for. This is shown in the lower absolute Mach number found in Figure 3.20.

Results of the 1-D vaned diffuser theory when applied to the Radiver test case were concluded to be adequate. The prediction of vane separation in the Radiver diffuser by the 1-D theory compared satisfactorily with the 3-D

results as shown in Figure 3.22. 1-D theory results of the Radiver diffuser static pressure ratio showed good correlation with the experimental results as shown in Figure 3.15. The 1-D vaned diffuser theory does not suffer from the same error in predictions once stall or choking is predicted such as found with the 1-D impeller theory. Further benchmarking of the vaned diffuser theory is recommended, as only one case was available.

The 3-D results obtained by FINE™/Turbo are satisfactory and outperforms the 1-D theory, specifically in the stall and choking regions. Overall 3-D results of the O-Rotor correlate better than 1-D results as shown in Figures 3.5 and 3.6. Overall results of the Radiver test case by FINE™/Turbo also correlate better than the 1-D theory as shown in Figures 3.15 and 3.16. Pressure and flow angle 3-D results of the O-Rotor shown in Figures 3.7 and 3.8 show excellent correlation with the experimental results. Further excellent correlation of 3-D results with the Radiver impeller tip results are shown in Figures 3.18 and 3.19 and of the vaned diffuser discharge in Figures 3.20 and 3.21. FINE™/Turbo specifically correlates better than the 1-D theory in predicting the absolute Mach number in Figure 3.20. Using Figure 3.22, the effective flow area at the vaned diffuser discharge can be compared to the entire flow area as implemented by the 1-D model. As discussed in Section 3.3.2, using the entire flow area at the vaned diffuser discharge in the 1-D model contributes to the error in 1-D results in Figure 3.20.

When applying the 1-D theory to the DEEP prototype, impeller blade stall was predicted over the entire operating flow range. The stall criterion ($D_{eq} > 2$) was satisfied with values for D_{eq} ranging from 2.455 to 2.67. This was verified by the 3-D model, where flow re-entering the impeller tip at the operating point is shown in Figure 4.4. The 3-D model also predicted a high Mach number region at the vaned diffuser inlet (see Figure 4.6), but this could not be verified by the 1-D model as previously discussed in Section 4.2. Diffuser vane separation over the entire operating range was predicted by the 1-D analysis, where $C_4 > C_{SEP}$ as discussed in Section 4.2. Separation was once again confirmed by the 3-D model as shown in Figures 4.8 and 4.9. As discussed previously in Section 4.2, the separation can be attributed to a non-optimal vane profile rather than an incorrect vane leading edge angle. This non-optimal vane profile also adds to diffuser performance deterioration.

5.2 Recommendations

Recommendations regarding the 1-D impeller code is to include the omitted inlet shock pressure loss coefficient formulation. The present omission is justified, as no supersonic flow was present at the impeller inlet of any of the thesis compressor cases, but it needs to be included for future work. Furthermore, the relevant loss coefficients can be investigated to provide better performance results once stall or choking is predicted.

A recommendation for the 1-D vaneless annular passage theory is to determine the originally intended control volume length. If the prescribed length cannot be determined, the theory should be revised to produce better results once grid convergence has been achieved. The error due to a sudden increase in flow area after a wedge-type vaned diffuser should also be investigated. Taking into account that the effective flow area is minimised, introducing a suitable area factor for the passage analysis might prove to be a solution.

If FINE™/Turbo is to be used for future centrifugal compressor projects, an additional software code to process the *.geomTurbo* file of the impeller to obtain the 1-D geometry information is recommended. The data that was used in conjunction with IGG™ to obtain the 1-D geometry as used in this thesis, is available in a standard *.geomTurbo* file. The same applies for obtaining the 1-D geometry for the vaned diffuser analysis. A further recommendation is to include academically recognised real gas tables to source the working medium properties, making it possible to import properties of different gasses in the future.

The 1-D program is currently segmented into three MATLAB® codes. Creating a governing MATLAB® code which uses the current codes as functions will be advantageous. The functions can then be used in a modular manner and will aid in obtaining results of different compressor configurations. Determining the choke and stall margins will be easier if the governing code reports warning states from the functions during the analysis. For instance, the impeller could be performing well according to the current impeller code (indicating a wide operating range) but choking could be present in the vaned diffuser throat. This smaller operating range will only be found once the vaned diffuser MATLAB® code is executed after the impeller code.

Benchmarking of the 1-D theory and FINE™/Turbo should be performed on smaller scale compressors such as found in micro gas turbines. The 1-D code should especially be benchmarked as the theory was originally intended for larger commercial compressors.

Taking the preceding discussion into account, a redesign of the entire diffuser section of the DEEP prototype is recommended. Emphasis is placed on the non-optimal vane profile and the diverging shroud contour. Considering the impeller blade and inducer stall, the author recommends a redesign of the impeller as well. Compressor stability will be improved by addressing the diffuser only, but might not produce a compressor that meets the original DEEP project performance requirements.

Appendices

Appendix A

Air Properties and Characteristics

Various air properties and characteristics were used repeatedly during the 1-D centrifugal compressor analysis and the relevant information is supplied in this section.

A.1 Air Properties

Three air properties, density (ρ), specific heat (C_p) and dynamic viscosity (μ), were used during the 1-D centrifugal compressor analysis and are determined using the static thermodynamic conditions. Equation (A.1.1) (White, 2003) shows the well-known perfect gas equation. The specific heat and dynamic viscosity correlations shown in Equations (A.1.2) and (A.1.3) (Kröger, 2004) are dependent on the static temperature only, assuming the static pressure is 1 bar.

$$p = \rho R T \tag{A.1.1}$$

$$\begin{aligned} C_p &= 1.045356 \times 10^{3} - 3.161783 \times 10^{-1} T \\ &\quad + 7.083814 \times 10^{-4} T^{2} - 2.705209 \times 10^{-7} T^{3} \end{aligned} \tag{A.1.2}$$

$$\begin{aligned} \mu &= 2.287973 \times 10^{-6} + 6.259793 \times 10^{-8} T \\ &\quad - 3.131956 \times 10^{-11} T^{2} + 8.15038 \times 10^{-15} T^{3} \end{aligned} \tag{A.1.3}$$

A.2 Critical Values at the Sonic Point

The phenomenon of aerodynamic choking is evaluated at the throat of both the impeller and diffuser stage and implements the flow area resulting in sonic conditions. Sonic, or critical, conditions occur when the Mach number (relative for the impeller and absolute for the diffuser) of the flow medium at the given operating conditions equals one ($M = 1$). Another viewpoint for the occurance

of choke is when the aerodynamic throat area is smaller than the area needed for a sonic velocity at the current static conditions and mass flow rate. This sonic flow area can be determined from Equation (A.2.1) (Aungier, 2000).

$$A^* = \frac{\dot{m}}{\rho^* V^*} \tag{A.2.1}$$

The needed critical density (ρ^*), temperature (T^*) and velocity (V^*) can be determined from Equations (A.2.2) through (A.2.4) (White, 2003) and are based on the total thermodynamic conditions.

$$\rho^* = \rho_t \left(\frac{2}{\gamma+1}\right)^{1/(\gamma-1)} \tag{A.2.2}$$

$$T^* = T_t \left(\frac{2}{\gamma+1}\right) \tag{A.2.3}$$

$$\begin{aligned} V^* = a^* &= \sqrt{\gamma R T^*} \\ &= \sqrt{\frac{2\gamma}{\gamma+1} R T_t} \end{aligned} \tag{A.2.4}$$

A.3 Skin Friction Coefficient

The effects of skin friction were evident in all of the centrifugal compressor stage components in the 1-D theory and a general formulation was needed to accomodate the wide range of operating conditions of centrifugal compressors. The formulation needed to include laminar and turbulent flow regimes as well as the influence of surface finish according to Aungier (2000).

Aungier (2000) suggests three well-established models (Haaland, 1983) for this purpose. The coefficients are correlated as a function of the peak-to-valley surface roughness (e) and Reynolds number (Re_d). The Reynolds number is based on the pipe diameter (d) and is supplied in Equation (A.3.1) (Aungier, 2000).

$$Re_d = \frac{\rho V d}{\mu} \tag{A.3.1}$$

The relevant velocity (absolute or relative depending on the stage being analysed) is represented by V and when applying the Reynolds number to general passages, the conventional practice is to replace d with the hydraulic diameter (d_H) shown in Equation (A.3.2) (Aungier, 2000).

$$d_H = 4(\text{cross-sectional area})/(\text{wetted perimeter}) \tag{A.3.2}$$

As mentioned, three models were used. Firstly, for laminar flow, $Re_d < 2000$, implement Equation (A.3.3) (Aungier, 2000).

$$c_{f,l} = 16/Re_d \tag{A.3.3}$$

Secondly, for turbulent flow, $Re_d > 4000$, within a smooth-walled pipe Aungier (2000) suggests using Equation (A.3.4).

$$\frac{1}{\sqrt{4c_{f,t,s}}} = -2\log_{10}\left[\frac{2.51}{Re_d\sqrt{4c_{f,t,s}}}\right] \tag{A.3.4}$$

Equation (A.3.4) does not supply an explicit solution for $c_{f,t,s}$ but Haaland (1983) offers a simplification in Equation (A.3.5), of which the roughness term has been omitted.

$$\frac{1}{\sqrt{4c_{f,t,s}}} = -1.8\log_{10}\left(\frac{6.9}{Re_d}\right) \tag{A.3.5}$$

For turbulent flow over a fully rough surface Aungier (2000) suggests using Equation (A.3.6), where d is again replaced by the hydraulic diameter from Equation (A.3.2).

$$\frac{1}{\sqrt{4c_{f,t,r}}} = -2\log_{10}\left[\frac{e}{3.71d}\right] \tag{A.3.6}$$

The surface finish is implemented using the root-mean-square (RMS) value. Aungier (2000) suggests that a reasonable method of converting these peak-to-valley values is to assume a sine wave form, as shown in Equation (A.3.7).

$$e = 2e_{RMS}/0.707 = e_{RMS}/0.3535 \tag{A.3.7}$$

When the flow is in transition between laminar and turbulent or smooth and rough zones, the skin friction coefficient is modeled as weigthed averages of

Equations (A.3.5) and (A.3.6). The surface roughness only becomes significant when the condition in Equation (A.3.8) (Aungier, 2000) is met.

$$Re_e = (Re_d - 2000)e/d > 60 \tag{A.3.8}$$

With this information the turbulent skin friction coefficient is weighted as shown in Equation (A.3.9) (Aungier, 2000).

$$\begin{aligned} c_{f,t} &= c_{f,t,s} \quad \text{for} \quad Re_e < 60 \\ c_{f,t} &= c_{f,t,s} + (c_{f,t,r} - c_{f,t,s})\,(1 - 60/Re_e) \quad \text{for} \quad Re_e \geq 60 \end{aligned} \tag{A.3.9}$$

Haaland (1983) does not recommend using a weighted average but rather supplies a single term for the turbulent skin friction coefficient which is shown in Equation (A.3.10), from which the simplification of Equation (A.3.5) was derived.

$$\frac{1}{\sqrt{4c_{f,t}}} = -1.8 \log_{10}\left[\frac{6.9}{Re_d} + \left(\frac{e}{3.71d}\right)^{10/9}\right] \tag{A.3.10}$$

Lastly, when the flow is in transition between laminar and turbulent phases, $2000 \leq Re_d \leq 4000$, the friction coefficient is a weigthed average of Equations (A.3.3) and (A.3.9) (or (A.3.10)) according to Equation (A.3.11) (Aungier, 2000).

$$c_f = c_{f,l} + (c_{f,t} - c_{f,l})(Re_d/2000 - 1) \tag{A.3.11}$$

The reader can apply discretion to use the weighted average supplied in Equation (A.3.9) or the single term in Equation (A.3.10) for the turbulent skin friction coefficient. White (2003) also comments that no reliable friction factors exist in the transition phase estimated by Equation (A.3.11).

For the current application the surface roughness terms are omitted due to the exact values of the thesis compressors being unknown, but it must be noted that the validation case studies used milled components (implying a good surface finish). Thus, a combination of Equations (A.3.3), (A.3.5) and (A.3.11) are used in the MATLAB® code after evaluating Re_d.

A.4 Boundary Layer Thickness

Flat-plate theory is used in the vaneless annular passage and vaned diffuser analysis and the boundary layer thickness (δ) is required for both.

Aungier (2000) suggests using a simple flat-plate boundary layer thickness for a vaneless annular passage analysis preceded by an impeller analysis. He does however note that a high degree of accuracy in specifying δ is not required. For the vaned diffuser analysis, Aungier (2000) supplies a simple flat-plate boundary layer approximation estimated at the midpassage as shown in Equation (A.3.1). This approximation was also used for determining δ of the impeller.

$$\delta = \frac{5.142}{2} c_f L_B \tag{A.4.1}$$

As discussed in Section 2.2.4, the hydraulic diameter is an average of the throat and discharge values but a limit is imposed, namely $2\delta/d_H \leq 1$.

Appendix B

1-D Centrifugal Compressor Theory Loss Coefficients

Loss and work coefficients ($\overline{\omega}_i$ and I_i respectively) omitted in Section 2.2 are supplied here, supplemented by a brief description of each loss coefficient. These coefficients are found in the impeller performance (Section 2.2.2) and vaned diffuser performance (Section 2.2.4) theories.

B.1 Impeller Performance

The blade input work coefficient (I_B) is the first to be determined. As mentioned previously, the slip factor (σ) implemented by Aungier (2000) is the approximated Busemann slip factor at zero flow by Wiesner (1967) and is shown in Equation (B.1.1).

$$\sigma = 1 - \frac{\sqrt{\sin \beta_2} \sin \alpha_{C,2}}{z^{0.7}} \tag{B.1.1}$$

This σ can be treated as constant up to the limiting radius ratio (ϵ_{LIM}) shown in Equation (B.1.2) (Aungier, 2000).

$$\begin{aligned} \epsilon_{LIM} &= \frac{\sigma - \sigma^*}{1 - \sigma^*} \\ \sigma^* &= \sin(19^\circ + 0.2\beta_2) \end{aligned} \tag{B.1.2}$$

If this limit is exceeded by the impeller meanline radius ratio ($\epsilon = r_1/r_2$), σ is corrected to σ_{corr} using Equation (B.1.3) (Aungier, 2000).

$$\sigma_{corr} = \sigma \left[1 - \left(\frac{\epsilon - \epsilon_{LIM}}{1 - \epsilon_{LIM}} \right)^{\sqrt{\beta_2/10}} \right] \tag{B.1.3}$$

To determine I_B, the wall skin friction loss coefficient ($\overline{\omega}_{SF}$) must be calculated using Equation (B.1.4) (Aungier, 2000). The skin friction coefficient (c_f) is calculated using the method explained in Appendix A.3 and the average of the throat and tip values are used to calculate the hydraulic diameter, relevant velocity $[(W_{th} + W_2)/2]$ and air properties. The tip area is $A_2 \sin\beta_2$, which is normal to the direction of flow.

$$\begin{aligned} \overline{\omega}_{SF} &= 4c_f \frac{\overline{W}^2 L_B}{W_1^2 d_H} \\ \overline{W}^2 &= \left(W_1^2 + W_2^2\right)/2 \\ \overline{W}^2 &\geq \left(W_{th}^2 + W_2^2\right)/2 \end{aligned} \tag{B.1.4}$$

Computing the wall skin friction loss utilises an averaged relative velocity ($\overline{W}^2$) which needs to be evaluated for both the throat-to-tip values and inlet-to-tip values. The higher value is used for the analysis.

With $\overline{\omega}_{SF}$ known, the tip blockage (B_2) can be determined from the model presented by Aungier (2000) as shown in Equation (B.1.5), where A_R follows from Equation (2.2.2).

$$B_2 = \overline{\omega}_{SF} \frac{p_{v,1}}{p_{v,2}} \sqrt{\frac{W_1 d_H}{W_2 b_2}} + \left[0.3 + \frac{b_2^2}{L_B^2}\right] \frac{A_R^2 \rho_2 b_2}{\rho_1 L_B} + \frac{s_{CL}}{2b_2} \tag{B.1.5}$$

With the tip blockage known, the work input from the impeller blades can be calculated using Equation (B.1.6). This equation was adapted by Aungier (2000) from Equation (B.1.7) to include slip. The tip distortion factor (λ_2) follows from Equation (B.1.8).

$$\begin{aligned} I_B &= \sigma\left(1 - \lambda_2 \phi_2 \cot\beta_2\right) - U_1 C_{U,1}/U_2^2 \\ \phi_2 &= \dot{m}/\left(\rho_2 A_2 U_2\right) \end{aligned} \tag{B.1.6}$$

$$I_B = C_{U,2}/U_2 - U_1 C_{U,1}/U_2^2 \tag{B.1.7}$$

$$\lambda_2 = 1/\left(1 - B_2\right) \tag{B.1.8}$$

Aungier (2000) provides different clearance gap flow work models for open and closed impeller designs. All of the impellers relevant to the project are of the open type design, thus only the relevant equations for open impellers were implemented. A pressure difference is present between the pressure and suction surfaces of an open impeller blade and due to the clearance gap some leakage throughflow from the pressure to suction surfaces will take place. This pressure difference creates the force required to balance the impeller torque given in Equation (B.1.9) (Aungier, 2000).

$$\tau = \dot{m}\left[r_2 C_{U2} - r_1 C_{U1}\right] \tag{B.1.9}$$

From this the average pressure difference across the blade in the clearance gap can be estimated from the change in fluid angular momentum through the impeller as given by Aungier (2000) in Equation (B.1.10).

$$\begin{aligned} \Delta p_{CL} &= \frac{\dot{m}\left(r_2 C_{U2} - r_1 C_{U1}\right)}{z\bar{r}\bar{b}L} \\ \bar{r} &= \left(r_1 + r_2\right)/2 \\ \bar{b} &= \left(b_1 + b_2\right)/2 \end{aligned} \tag{B.1.10}$$

Aungier (2000) uses Equation (B.1.11) to calculate the velocity of the clearance gap leakage flow, where the coefficient of 0.816 accounts for the abrupt contraction loss when the leakage flow enters the clearance gap, followed by an abrupt expansion loss as the leakage flow leaves the clearance gap. As can be seen, ρ_2 is used and is considered to be constant throughout the entire blade length.

$$U_{CL} = 0.816\sqrt{2\Delta p_{CL}/\rho_2} \tag{B.1.11}$$

Using the throughflow velocity, flow area and again ρ_2, the blade clearance gap leakage mass flow rate for all of the blades can be determined from Equation (B.1.12) and in turn the leakage work in Equation (B.1.13) (Aungier, 2000).

$$\dot{m}_{CL} = \rho_2 U_{CL}\left(z s_{CL} L_{FB}\right) \tag{B.1.12}$$

$$I_L = \frac{\dot{m}_{CL} U_{CL}}{2\dot{m} U_2} \tag{B.1.13}$$

Windage and disk friction work is a result of friction between the impeller disk and compressor housing. Aungier (2000) proposes the equation by Daily and Nece (1960a and 1960b) to determine windage and disk friction losses of rotating smooth and rough disks in housings. The disk torque coefficient is defined by Equation (B.1.14).

$$C_M = \frac{2\tau}{\rho\omega^2 r^5} \tag{B.1.14}$$

Daily and Nece (1960a and 1960b) consider four different flow regimes provided by the torque coefficients in Equations (B.1.15) to (B.1.18). All four coefficients must be calculated and the largest value of C_{M1-4} represents the correct flow regime, C_{M0}.

$$C_{M1} = \frac{2\pi}{\left(s_D/r_2\right) Re_{CM}} \quad \text{for laminar, merged boundary layers} \tag{B.1.15}$$

$$C_{M2} = \frac{3.7\left(s_D/r_2\right)^{0.1}}{\sqrt{Re_{CM}}} \quad \text{for laminar, separate boundary layers} \tag{B.1.16}$$

$$C_{M3} = \frac{0.08}{(s_D/r_2)^{1/6}\, Re_{CM}^{1/4}} \quad \text{for turbulent, merged boundary layers} \tag{B.1.17}$$

$$C_{M4} = \frac{0.102\,(s_D/r_2)^{0.1}}{Re_{CM}^{0.2}} \quad \text{for turbulent, separate boundary layers} \tag{B.1.18}$$

The Reynolds number in Equations (B.1.15) to (B.1.18) is determined by Equation (B.1.19).

$$Re_{CM} = \frac{\rho_2 \omega_2 r_2^2}{\mu_2} \tag{B.1.19}$$

Surface roughness was not deemed relevant for the thesis as the impellers were CNC machined and no roughness information was available. Thus the surface finish is assumed to be smooth. Aungier (1995) furthermore applies some empirical corrections to the ideal disk torque coefficients of Equations (B.1.15) to (B.1.18) using Equation (B.1.20).

$$C_M = C_{M0}\,(1-K)^2 \,/\, (1-K_0)^2 \tag{B.1.20}$$

K_0 and K are determined from Equation (B.1.21) (Aungier, 2000).

$$\begin{aligned} K &= C_{U,2}/U_2 \\ K_0 &= 0.46/\,(1 + 2s_D/d_2) \end{aligned} \tag{B.1.21}$$

The impeller disk friction torque coefficient is computed separately for the disk and cover (if one is included in the design) and the results are corrected according to Equation (B.1.22). For the test cases investigated during the thesis, the impellers are of the uncovered design and hence C_{MC} does not apply.

$$\begin{aligned} C_{MD} &= 0.75 C_M \\ C_{MC} &= 0.75 L_{FB} C_M \left[1 - (d_{1,s}/d_2)^5\right] / \,(r_2 - r_1) \end{aligned} \tag{B.1.22}$$

From this, the energy consumed by windage and disk friction is $\omega\tau$ and the work input is calculated using Equation (B.1.23).

$$I_{DF} = (C_{MD} + C_{MC})\,\rho_2 U_2 r_2^2 / \,(2\dot{m}) \tag{B.1.23}$$

At low mass flow rates a pronounced increase in work input can be observed. It is believed to be associated with flow recirculating back into the tip of the impeller. Aungier (2000) notes that this is common for impellers with a very high head coefficient with excessive blade loading and low tip relative flow angles. Aungier (1995) generalised the axial compressor equivalent diffusion factor by Lieblein (1959) to radial and mixed flow blades to evaluate the blade

loading. An average blade velocity difference (ΔW) is computed as shown in Equation (B.1.24).

$$\Delta W = 2\pi d_2 U_2 I_B / (z L_B) \tag{B.1.24}$$

From this, the diffusion factor (D_{eq}) can be determined according to Equation (B.1.25).

$$\begin{aligned} W_{max} &= (W_1 + W_2 + \Delta W)/2 \\ D_{eq} &= W_{max}/W_2 \end{aligned} \tag{B.1.25}$$

Blade stall can be expected when $D_{eq} > 2$ according to Lieblein (1959) and Aungier (2000) found this to be an appropriate stall limit for impellers as well. When $D_{eq} > 2$, the work input coefficient associated with recirculation is computed from Equation (B.1.26). It has been observed that the $I_R \geq 0$ constraint might result in $I_R = 0$ even if $D_{eq} > 2$ for most impellers.

$$\begin{aligned} I_R &= (D_{eq}/2 - 1)(W_{U,2}/C_{m,2} - 2\cot\beta_2) \\ I_R &\geq 0 \end{aligned} \tag{B.1.26}$$

With all of the work coefficients known, I is calculated using Equation (2.2.12). As discussed in Section 2.2.2, an iterated T_2 is then determined. Determining the remainder of the loss coefficients ($\overline{\omega}_i$) needed by Equation (2.2.13), is discussed in the following paragraphs.

Aungier mentions a shock pressure loss ($\overline{\omega}_{sh}$) in the event of the resulting entrance velocities exceeding sonic conditions and is computed using normal shock relations. No specific formulation can be found for $\overline{\omega}_{sh}$ in Aungier (2000) nor Aungier (1995) and was therefore not included in the MATLAB® code. $\overline{\omega}_{sh}$ is only applicable when the inlet flow is supersonic, which is not found in any of the thesis compressor cases. Thus the author did not enquire further.

An incidence loss is observed when the actual inlet flow has to adjust to the blade angle and can be computed from Equation (B.1.27) (Aungier, 2000). This equation is applied at the hub, mean and shroud stream surfaces. A weighted average of the hub, mean and shroud values defines the overall incidence loss coefficient, where the mean stream surface value is weighted 10 times heavier than the hub and shroud values.

$$\overline{\omega}_{inc} = 0.8\left[1 - \frac{C_{m,1}}{W_1 \sin\beta_1}\right]^2 + \left[\frac{z_{FB} t_{b,1}}{2\pi r_1 \sin\beta_1}\right]^2 \tag{B.1.27}$$

To compute the hub and shroud values, Equation (B.1.28) (Aungier, 2000) and Figure 2.7 is used by substituting "1" in Figure 2.7 with the relevant stream surface value. The absolute meridional velocity components ($C_{m,1,*}$) are calculated using Equation (B.1.28) and the absolute tangential velocity

components equal the mean stream surface value ($C_{U,1} = C_{U,1,h} = C_{U,1,s}$) if pre-whirl is present. The blade velocity is evaluated at the relevant stream surface ($U_{1,*}$) and with the help of Figure 2.7, the relative velocity component ($W_{1,*}$) is determined.

$$\begin{aligned} C_{m,1,h} &= C_{m,1}\left[1 + \kappa_{m,1} b_1/2\right] \\ C_{m,1,s} &= C_{m,1}\left[1 - \kappa_{m,1} b_1/2\right] \end{aligned} \tag{B.1.28}$$

The curvature term in Equation (B.1.28) is computed from Equation (B.1.29) using the reference system of Aungier (2000).

$$\kappa_m = -\frac{\partial \alpha_C}{\partial m} \tag{B.1.29}$$

Aungier (2000) notes that the loss due to diffusion between the impeller blade leading edge and the throat has been found to be more significant than the incidence loss. The corresponding entrance diffusion loss coefficient ($\overline{\omega}_{DIF}$) is calculated from Equation (B.1.30). During the test case investigations, the diffusion loss was found to be negative for some mass flow rates. In this case the constraint in Equation (B.1.30) returns $\overline{\omega}_{DIF} = 0$.

$$\overline{\omega}_{DIF} = 0.8\left[1 - W_{th}/W_1\right]^2 - \overline{\omega}_{inc} \quad \text{where } \overline{\omega}_{DIF} \geq 0 \text{ is required} \tag{B.1.30}$$

Pronounced stall in the inducer has been observed by Aungier (2000) at lower flow rates, which can prevent stable operation of the compressor due to surge. Flow diffusion between the inlet and throat is a good indicator of inducer stall and Aungier (2000) proposes the stall criterion in Equation (B.1.31).

$$W_{1,s}/W_{th} \geq 1.75 \tag{B.1.31}$$

In the event of inducer stall being predicted, the diffusion loss coefficient is limited by Equation (B.1.32).

$$\overline{\omega}_{DIF} \geq \left(\frac{W_{1,s} - 1.75 W_{th}}{W_1}\right)^2 - \overline{\omega}_{inc} \tag{B.1.32}$$

At higher mass flow rates the onset of supersonic flow will be observed and a corresponding choking loss coefficient is calculated from Equation (B.1.33) (Aungier, 2000). The area required at the assigned mass flow rate to yield a sonic velocity is denoted as A^* and is determined by using Equations (A.2.1) to (A.2.4). To determine the onset of choking in the impeller throat, the contracted throat area needs to be smaller than the sonic flow area, i.e. choking is observed when $C_r A_{th} \leq A^*$.

$$
\begin{aligned}
X &= 11 - 10 C_r A_{th}/A^* \\
\overline{\omega}_{CH} &= 0 && \text{if } X \leq 0 \\
\overline{\omega}_{CH} &= 0.5\left(0.05X + X^7\right) && \text{if } X > 0
\end{aligned} \tag{B.1.33}
$$

During the verification studies, the MATLAB® code was found to be very sensitive to variations in the throat area value. This is due to the use of X^7 in Equation (B.1.33) which results in divergence if A^* is even slightly larger than $C_r A_{th}$, thus if X is slightly larger than 1.

When high blade-to-blade (B2B) pressure gradients are present, secondary flows might be produced which may lead to blade stall. The blade loading loss coefficient associated with this phenomenon can be calculated using Equation (B.1.34) from Aungier (2000). The definition for ΔW has been provided in Equation (B.1.24).

$$
\overline{\omega}_{BL} = \frac{1}{24}\left(\frac{\Delta W}{W_1}\right)^2 \tag{B.1.34}
$$

Similar to the B2B loading loss, a loading loss in the hub-to-shroud (H2S) direction can be computed from Equation (B.1.35). Aungier (2000) reports that severe flow separation might occur when the B2B and H2S pressure gradients become large compared to the velocity head.

$$
\begin{aligned}
\overline{\omega}_{H2S} &= \frac{1}{6}\left(\frac{\overline{\kappa_m}\,\overline{b}\,\overline{W}}{W_1}\right)^2 \\
\overline{\kappa_m} &= \left(\alpha_{C,2} - \alpha_{C,1}\right)/L_{FB} \\
\overline{b} &= \left(b_1 + b_2\right)/2 \\
\overline{W} &= \left(W_1 + W_2\right)/2
\end{aligned} \tag{B.1.35}
$$

The abrupt expansion loss model by Aungier (2000) uses λ_2, provided in Equation (B.1.8), to determine the abrupt expansion loss coefficient supplied in Equation (B.1.36). Aungier (2000) notes that results from this equation proves almost equal to that of the well-known abrupt expansion loss by Benedict *et al.* (1966).

$$
\overline{\omega}_{\lambda} = \left[\frac{\left(\lambda_2 - 1\right) C_{m,2}}{W_1}\right]^2 \tag{B.1.36}
$$

Similar to the abrupt expansion loss, a loss associated with blade wake mixing can be determined. The velocity at which separation occurs (W_{SEP}) needs to be estimated in order to estimate the magnitude of the wake. D_{eq}, defined in Equation (B.1.25), is used to estimate W_{SEP} (Aungier, 2000).

$$\begin{aligned} W_{SEP} &= W_2 && \text{if } D_{eq} \leq 2 \\ W_{SEP} &= W_2 D_{eq}/2 && \text{if } D_{eq} > 2 \end{aligned} \tag{B.1.37}$$

Due to wake mixing occurring after the impeller where blade forces are not present, conservation of angular momentum controls the tangential velocity. This results in only the meridional velocity component being involved in calculating the wake mixing loss coefficient. By assuming the gas density to be approximately constant and using conservation of mass and the value of W_{SEP}, the meridional velocity components before and after mixing can be estimated from Equation (B.1.38) (Aungier, 2000).

$$\begin{aligned} C_{m,wake} &= \sqrt{W_{SEP}^2 - W_{U,2}^2} \\ C_{m,mix} &= \frac{C_{m,2} A_2}{\pi d_2 b_2} \end{aligned} \tag{B.1.38}$$

The wake mixing loss coefficient is then provided by Aungier (2000) in Equation (B.1.39).

$$\overline{\omega}_{mix} = \left(\frac{C_{m,wake} - C_{m,mix}}{W_1} \right)^2 \tag{B.1.39}$$

The B2B pressure difference and clearance gap leakage associated with open impellers in Equations (B.1.10) and (B.1.12) can be implemented to determine the clearance gap leakage loss coefficient provided in Equation (B.1.40) (Aungier, 2000).

$$\overline{\omega}_{CL} = \frac{2 \dot{m}_{CL} \Delta p_{CL}}{\dot{m} \rho_1 W_1^2} \tag{B.1.40}$$

Aungier (2000) mentions a supercritical Mach number loss coefficient associated with supersonic flow at the midpassage. The local sonic velocity (W^*) at the midpassage can be calculated using the relative thermodynamic conditions from the average of the inlet and tip values. From this, the inlet critical Mach number indicating the onset of supersonic flow at the midpassage suction surface is estimated by Equation (B.1.41). The equation supplied by Aungier (2000) differs from that of Aungier (1995) regarding the use of M_1 instead of M_1'. The author chose to use M_1' due to the loss coefficient being examined at the midpassage, hence in the impeller's rotating frame of reference.

$$M_{CR}' = M_1' W^* / W_{max} \tag{B.1.41}$$

W_{max} is computed using Equation (B.1.25). Shocks will form when the blade suction surface velocity is supersonic at the midpassage and will likely

induce boundary layer separation. If this occurs, a supercritical Mach number loss coefficient is estimated using Equation (B.1.42) (Aungier, 2000).

$$\overline{\omega}_{CR} = 0.4 \left[\frac{(M_1' - M_{CR}')\, W_{max}}{W_1} \right]^2 \tag{B.1.42}$$

All of the relevant pressure loss coefficients ($\overline{\omega}_i$) have been determined. With these known, $p_{t,2}'$ is determined using Equation (2.2.13) and as discussed in Section 2.2.2, iterated values of p_2 and $p_{t,2}$ are determined. A new ρ_2 is calculated using the perfect gas equation and new values for $C_{m,2}$, $C_{U,2}$ and C_2 follow from conservation of mass, Equation 2.2.17 and the velocity triangle in Figure 2.10 respectively. The impeller analysis is then repeated until ρ_2 converges.

B.2 Vaned Diffuser Performance

As previously mentioned, the throat contraction ratio supplied in Equation (2.2.34) accounts for the sudden change in flow area from inlet to throat. Similar to the impeller analysis, choking is observed when $C_r A_{th} \leq A^*$, where A^* is determined using Equations (A.2.1) to (A.2.4). Aungier (1990) includes a choking loss coefficient, which is similar to that of the impeller analysis, and is supplied in Equation (B.2.1).

$$\begin{aligned} X &= 11 - 10 C_r A_{th}/A^* \\ \overline{\omega}_{CH} &= 0 && \text{if} \quad X \leq 0 \\ \overline{\omega}_{CH} &= 0.5\left(0.05X + X^7\right) && \text{if} \quad X > 0 \end{aligned} \tag{B.2.1}$$

Stall in the vaned diffuser is based on the parameter K provided by Aungier (2000) in Equation (B.2.2). This parameter is evaluated between the inlet and throat and an average value is approximated by Equation (B.2.3) where h_{th} is the throat width.

$$K = -r \frac{\partial \cos\alpha}{\partial r} \tag{B.2.2}$$

$$K = \frac{r_3}{h_{th}} \left(\frac{\cos\alpha_3}{\cos\alpha_{th}} - 1 \right) \quad \text{where} \quad \alpha_{th} = \arcsin\left(A_{th}/A_3\right) \tag{B.2.3}$$

Aungier (2000) notes that these specific approximations are significant and were applied to develop the stall criterion from experimental data. He also notes that a high Mach number has a significant effect on the onset of stall in a vaned diffuser. As the Mach number increases, K will approach infinity, even in a vaneless space. Aungier (2000) defines this "unguided" value of K as K_0 in Equation (B.2.4).

$$K_0 = \frac{M_3^2 \sin^2 \beta_3 \cos \beta_3}{1 - M_3^2 \sin^2 \beta_3} \tag{B.2.4}$$

Aungier (2000) derived this equation from the basic fluid dynamic equation of motion in a radial, vaneless space with constant width and the flow angle set equal to the vane inlet angle. After comparison with experimental stall limits, Aungier (2000) found that stall in vaned diffusers is well approximated by the criterion in Equation (B.2.5).

$$K + K_0 = 0.39 \tag{B.2.5}$$

Aungier (2000) then uses this criterion to determine the inlet flow angle corresponding to vaned diffuser stall ($\alpha_{3,S}$), defined in Equation (B.2.6).

$$\alpha_{3,S} = \arccos \left[\cos \alpha_{th} \left(\frac{h_{th}(0.39 - K_0)}{r_3} + 1 \right) \right] \tag{B.2.6}$$

To determine the skin friction loss coefficient, Aungier (2000) provides the model in Equation (B.2.7). The average of the throat and discharge values are used to determine the hydraulic diameter (d_H) from Equation (A.3.2) and friction coefficient (c_f) from Appendix A.3.

$$\begin{aligned} \overline{\omega}_{SF} &= 4c_f \left(\frac{\overline{C}}{C_3} \right)^2 \frac{L_B}{d_H} \left(\frac{d_H}{2\delta} \right)^{0.25} \\ \overline{C}^2 &= \left(C_3^2 + C_4^2 \right)/2 \\ \overline{C}^2 &\geq \left(C_{th}^2 + C_4^2 \right)/2 \end{aligned} \tag{B.2.7}$$

The $2\delta/d_H$ term in Equation (B.2.7) is to correct the skin friction coefficient from the fully-developed flow model according to Aungier (2000). This is due to boundary layers in diffusers usually not being merged into fully-developed flow profiles. The boundary layer thickness (δ) is again estimated at midpassage from the simple flat-plate approximation in Equation (A.4.1).

Aungier (2000) defines the optimum or minimum-loss incidence angle (α_3^*) in Equation (B.2.8). This condition approximately balances the flow adjustments required to match the vane angle and the throat area. Aungier (2000) states that for typical vanes, the optimum condition corresponds to a modest negative incidence angle. C_3^* is an entrance velocity defined by α_3^*.

$$\begin{aligned} \alpha_3^* &= \arcsin \left(C_{m,3}/C_3^* \right) \\ C_3^* &= \frac{C_{m,3}}{\sqrt{\sin \beta_3 \sin \alpha_{th}}} \end{aligned} \tag{B.2.8}$$

This optimum incidence angle corresponds to a minimum incidence loss, supplied in Equation (B.2.9) (Aungier, 2000). The first term of this equation

can be recognised as 80% of the abrupt expansion loss by Benedict *et al.* (1966), defined between C_3^* and C_{th}. Aungier (2000) notes that the second term accounts for the abrupt contraction in flow area at the leading edge due to the possibility of thick vanes.

$$\overline{\omega}_{inc0} = 0.8\left(\frac{C_3^* - C_{th}}{C_3}\right)^2 + \left(\frac{z_D t_{b,3}}{2\pi r_3}\right)^2 \tag{B.2.9}$$

To account for off-design incidence losses, Aungier (2000) again implements part of the abrupt expansion loss by Benedict *et al.* (1966), which is referenced to C_3^* and the velocity corresponding to the stall incidence, $C_{3,S} = C_{m,3}/\sin\alpha_{3,S}$. When $C_3 \leq C_{3,S}$, the off-design incidence loss is calculated using Equation (B.2.10).

$$\overline{\omega}_{inc} = 0.8\left(\frac{C_3 - C_3^*}{C_3}\right)^2 \tag{B.2.10}$$

When $C_3 > C_{3,S}$, Aungier (2000) assumes that 80% of the ideal pressure recovery is lost, as shown in Equation (B.2.11). Both the terms $\overline{\omega}_{inc0}$ and $\overline{\omega}_{inc}$ are included in the sum of Equation (2.2.36).

$$\overline{\omega}_{inc} = 0.8\left[\left(\frac{C_{th}}{C_{3,S}}\right)^2 - \left(\frac{C_{th}}{C_3}\right)^2 + \left(\frac{C_{3,S} - C_3^*}{C_{3,S}}\right)^2\right] \tag{B.2.11}$$

To model blockage at the vaned diffuser discharge, Aungier (2000) used the effective correlation by Aungier (1988) as the basis for a blockage loss coefficient. He then modified it to permit application to thick vanes and variations in end wall height (b). This final model employs two basic design parameters, the diffuser divergence angle (θ_C) and the vane loading parameter (L) defined in Equations (B.2.12) and (B.2.13).

$$2\theta_C = 2\arctan\left(\frac{b_4\left(w_4 - t_{b,4}\right) - b_3\left(w_3 - t_{b,3}\right)}{2L_B b_3}\right)$$

$$\text{where} \quad w = \frac{2\pi r}{z_D}\sin\beta \tag{B.2.12}$$

$$L = \Delta C/\left(C_3 - C_4\right) \tag{B.2.13}$$

The average B2B loading velocity difference (ΔC) is defined by Aungier (2000) in Equation (B.2.14).

$$\Delta C = \frac{2\pi\left(r_3 C_{U,3} - r_4 C_{U,4}\right)}{z_D L_B} \tag{B.2.14}$$

Aungier (2000) observed an abrupt deterioration in vaned diffuser performance when $L > 1/3$ or when $2\theta_C > 11°$. Correction coefficients are then defined accordingly by Equation (B.2.15).

$$\begin{aligned} 1 \leq C_\theta \geq 2\theta_C/11^\circ \\ 1 \leq C_L \geq 3L \end{aligned} \tag{B.2.15}$$

The discharge area blockage is then defined by Aungier (2000) in Equation (B.2.16).

$$B_4 = \frac{L_B}{w_4}\left[K_1 + K_2\left(\overline{C}_R^2 - 1\right)\right] \tag{B.2.16}$$

The additional terms for Equation (B.2.16) are supplied in Equation (B.2.17).

$$\begin{aligned} \overline{C}_R &= \frac{1}{2}\left[\frac{C_{m,3}\sin\beta_4}{C_{m,4}\sin\beta_3} + 1\right] \\ K_1 &= 0.2\left[1 - \frac{1}{C_L C_\theta}\right] \\ K_2 &= \frac{2\theta_C}{125 C_\theta}\left[1 - \frac{2\theta_C}{22 C_\theta}\right] \end{aligned} \tag{B.2.17}$$

Aungier (1988) supplies a blockage loss coefficient using the abrupt expansion loss by Benedict *et al.* (1966) in Equation (B.2.18), which is similar to the model used by the impeller analysis.

$$\begin{aligned} \overline{\omega}_\lambda &= \left[\left(\lambda_4 - 1\right) C_{m,4}/C_3\right]^2 \\ \lambda_4 &= 1/\left(1 - B_4\right) \end{aligned} \tag{B.2.18}$$

To account for excessive streamwise diffusion and vane discharge metal thickness, Aungier (2000) includes a wake mixing loss similar to the impeller analysis. Separation of flow is assumed to occur when the velocity value defined by Equation (B.2.19) is reached.

$$\begin{aligned} C_{SEP} &= C_3/\left(1 + 2C_\theta\right) \\ C_{SEP} &\geq C_4 \quad \text{required} \end{aligned} \tag{B.2.19}$$

Similar to the impeller analysis, only $C_{m,4}$ is involved in the wake mixing process. The discharge tangential velocity ($C_{U,4}$) is governed by conservation of angular momentum when no vane forces are present. The meridional velocities before and after mixing are calculated by Aungier (2000) using Equation (B.2.20).

$$\begin{aligned} C_{m,wake} &= \sqrt{C_{SEP}^2 - C_{U,4}^2} \\ C_{m,mix} &= \frac{A_4}{2\pi r_4 b_4} C_{m,4} \end{aligned} \tag{B.2.20}$$

The wake mixing loss is then determined using Equation (B.2.21) (Aungier, 2000).

$$\overline{\omega}_{mix} = \left(\frac{C_{m,wake} - C_{m,mix}}{C_3} \right)^2 \tag{B.2.21}$$

The determined loss coefficients are summed and implemented in Equation (2.2.36) to determine the iterated total discharge pressure ($p_{t,4}$).

As previously mentioned, Aungier (2000) determines the vane discharge flow angle using axial-flow compressor correlations transformed to the radial plane. The minimum-loss deviation angle (δ^*) by Howell (1947) is provided in Equation (B.2.22).

$$\delta^* = \frac{\theta \left[0.92 \left(a/c \right)^2 + 0.02 \left(90° - \beta_4 \right) \right]}{\sqrt{\sigma} - 0.02\theta} \tag{B.2.22}$$

The location of the point of maximum camber (a/c), solidity (σ) and camber angle (θ) is supplied in Equation (B.2.23) (Aungier, 2000).

$$\begin{aligned} a/c &= \left[2 - \left(\overline{\beta} - \beta_3 \right) / \theta \right] / 3 \\ \sigma &= z_D \frac{r_4 - r_3}{2\pi r_3 \sin \overline{\beta}} \\ \theta &= \beta_4 - \beta_3 \\ \overline{\beta} &= \left(\beta_3 + \beta_4 \right) / 2 \end{aligned} \tag{B.2.23}$$

Aungier (2000) models the variation of the deviation angle with incidence by an empirical correlation of graphical data presented by Johnsen and Bullock (1965) as shown in Equation (B.2.24).

$$\frac{\partial \delta}{\partial i} = e^{\sigma \left[(1.5 - \beta_3/60°)^2 - 3.3 \right]} \tag{B.2.24}$$

The discharge flow angle (α_4) of the vaned diffuser is then calculated using the above parameters in Equation (2.2.37) (Aungier, 2000).

As previously mentioned, C_4 is calculated from $C_{m,4}$ (which followed from conservation of mass) using Figure 2.17 and α_4. The static enthalpy (h_4) is then determined from $h_{t,4}$ using Equation (2.2.7) and C_4. The discharge static temperature (T_4) follows from Equation (2.2.6) and the discharge static pressure (p_4) follows from the isentropic relation in Equation (2.2.8) using the total discharge conditions as reference. Using the perfect gas equation (Appendix A.1), the iterated discharge density (ρ_4) is determined and the analysis is repeated until $C_{m,4}$ converges.

Appendix C

AutoGrid5™ Meshes of the Thesis Compressors

The AutoGrid5™ mesh configurations and quality summaries of the thesis compressors are provided in this section. Default configuration settings were used for all of the compressors unless otherwise stated.

C.1 The Eckardt O-Rotor

As mentioned in Section 3.2, two shroud contours for the O-Rotor were investigated using FINE™/Turbo v8.4-3. The mesh was originally configured for the linear tapered shroud and generated using AutoGrid5™ v8.4-3. Subsequently, the mesh setup was copied and the shroud contour in the *".geomTurbo"* file was replaced with that of the hyperbolic profile, followed by regeneration of the mesh. Thus two meshes, with identical parameter setups but having slightly different diffuser mesh qualities, were used.

A comparison of the hyperbolic contoured and linear tapered meridional views are provided in Figure C.1. 61 Flow paths were used of which 17 were in the shroud gap and layer control was applied at 1 % intervals. For the flow paths distribution from hub-to-shroud (H2S), 60 % of the mid-flow paths were chosen as constant. Similarly for the shroud gap, 33 % were chosen. The shroud gap width at both the leading and trailing edge was set to 0.3722 mm following a linear interpolation of the values provided by Eckardt (1976) at the given rotational speed.

The default (O4H) topology configuration with matching periodicity was chosen for the *"B2B Topology"*. A summary of the impeller blade-to-blade (B2B) grid points can be viewed in Figure C.2. The appropriate cell width at all of the walls (except for the blade trailing edge) was found to be 4.45 μm in order to achieve acceptable y^+ values. This is supported by the y^+ values in Appendix E.1.

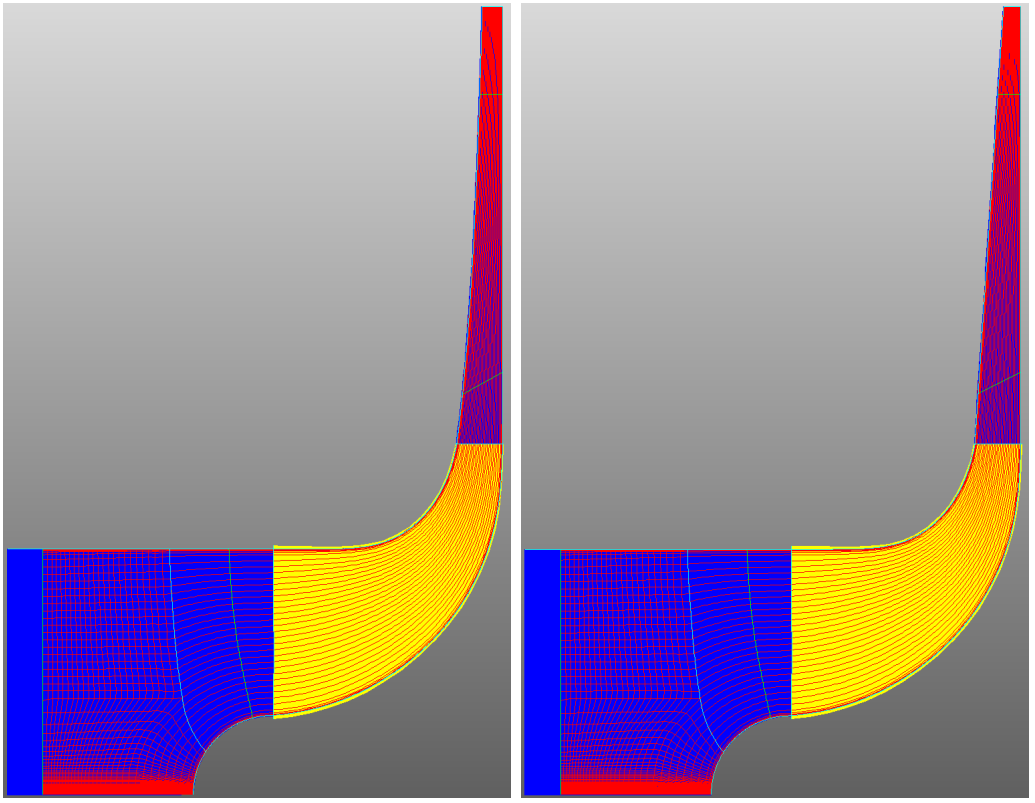

(a) Hyperbolic contoured. (b) Linear tapered.

Figure C.1: Meridional (Z-r) views of the O-Rotor.

The impeller blade surface cell width expansion ratio was set to 1.5 and the cell width at the blade trailing edge was chosen as the default value of -1.0 to increase the mesh quality considerably. No indication is given of what the exact value is in the user manual (AutoGrid5™ Manual, 2010), but lowering the cell width to match the value used for the other walls severely affected the orthogonality at the trailing edge. Using -1.0 is acceptable in cases where the blade is very thin and the influence on accuracy resulting from incorrect y^+ values at the tip are regarded as negligible.

No expert parameters were set in the *"Optimization Properties"* window but 760 B2B mesh optimization steps and 130 gap optimization steps were found to provide the best B2B mesh.

Due to the rounded inlet bulb, a singular line was not chosen for the *"Bulb Topology"* and this results in a butterfly type mesh at zero radius. Using a butterfly type mesh limits the orthogonality in the bulb to $360°/(z_{FB} + z_{SB})$. An additional *"Z-Constant"* line was added upstream (25 streamwise points) of the blade leading edge and two lines downstream (37 and 17 streamwise points respectively) of the trailing edge to improve the mesh. *"Fixed Geometry"* was disabled for all of the lines.

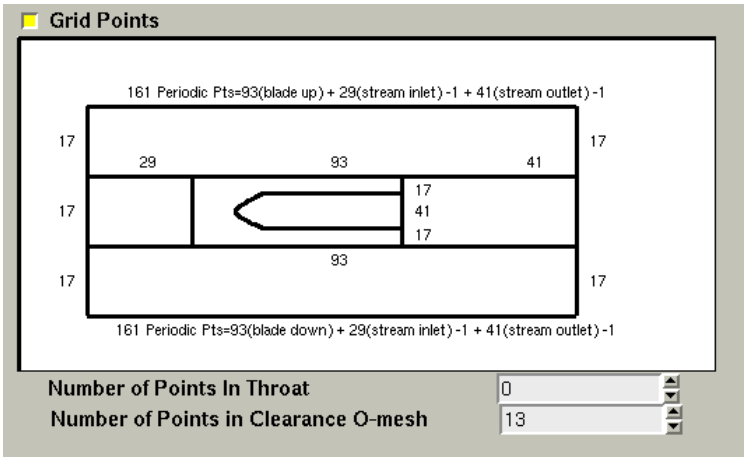

Figure C.2: O-Rotor impeller grid points summary.

Table C.1: Hyperbolic contoured O-Rotor B2B mesh quality.

	Orthogonality	Aspect Ratio	Expansion Ratio
Hub	35.92°	1495.82	2.39
Shroud	22.259°	2445.7	2.475

Samples of the impeller leading and trailing edge B2B meshes at the hub and shroud can be viewed in Figures C.3 and C.4 respectively.

The resulting mesh contained 1 366 070 grid points and a quality summary of the hyperbolic contoured case is supplied in Table C.1. The orthogonality represents the minimum values obtained. The aspect and expansion ratios represent the maximum values at the respective spanwise position as discussed in Section 2.3.3. Due to the linear tapered shroud case using the same mesh setup, the results were near identical and thus omitted. The reader can view a sample of the AutoGrid5™ block wire mesh in Figure C.5.

C.2 The Radiver Test Case

AutoGrid5™ v8.7-2 was used to generate the 3-D mesh of the Radiver test case and a meridional view of the compressor is provided in Figure C.6. For the impeller, 57 flow paths were used of which 17 were in the shroud gap and layer control was set to the default value of 0 %. This optimises the mesh on all of the layers. For the flow paths distribution from H2S, 50 % of the mid-flow paths were chosen as constant and for the shroud gap, 33 % were chosen. The shroud gap width at the leading and trailing edge was set to 0.6887 mm and 0.4813 mm respectively following the tip-clearance relation provided by Ziegler *et al.* (2003*c*) at the given rotational speed.

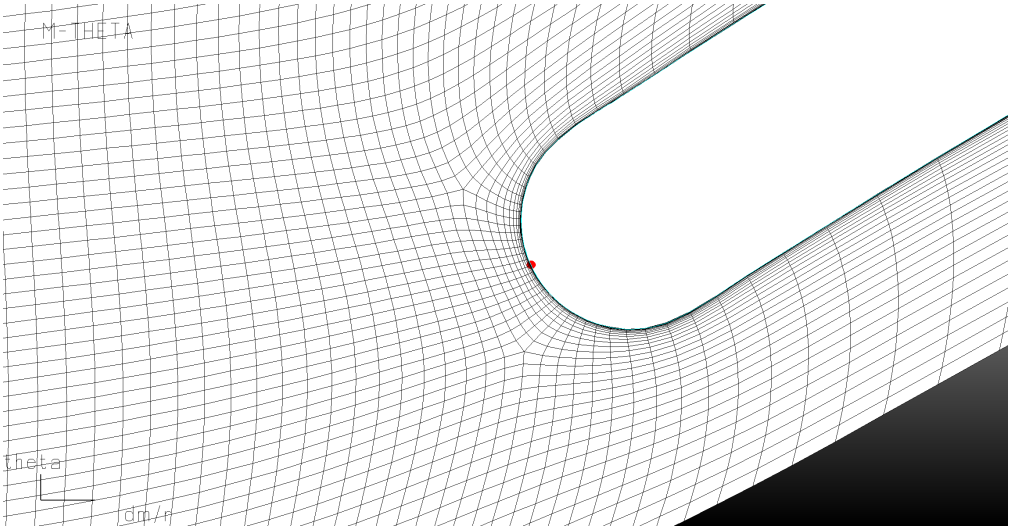

(a) Leading edge.

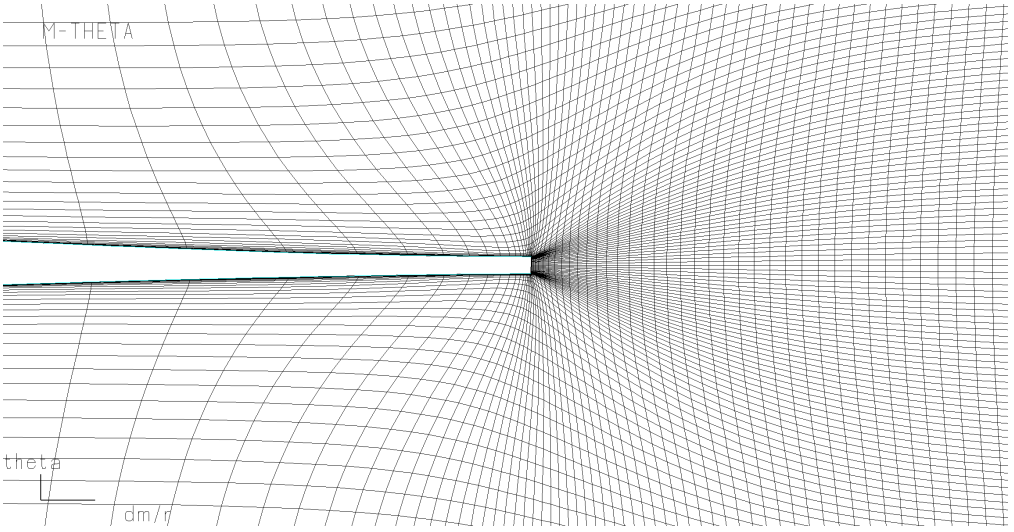

(b) Trailing edge.

Figure C.3: Hub B2B mesh views of the O-Rotor impeller.

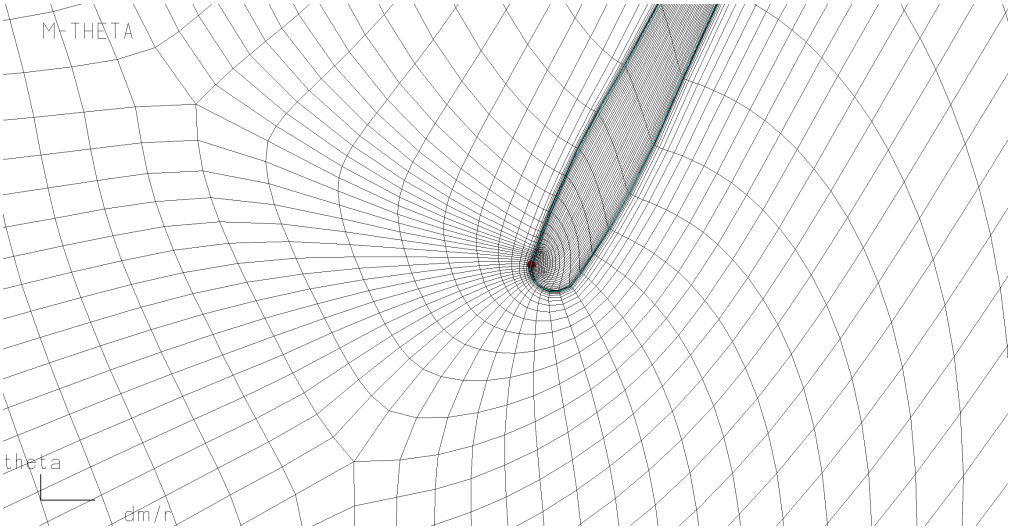

(a) Leading edge.

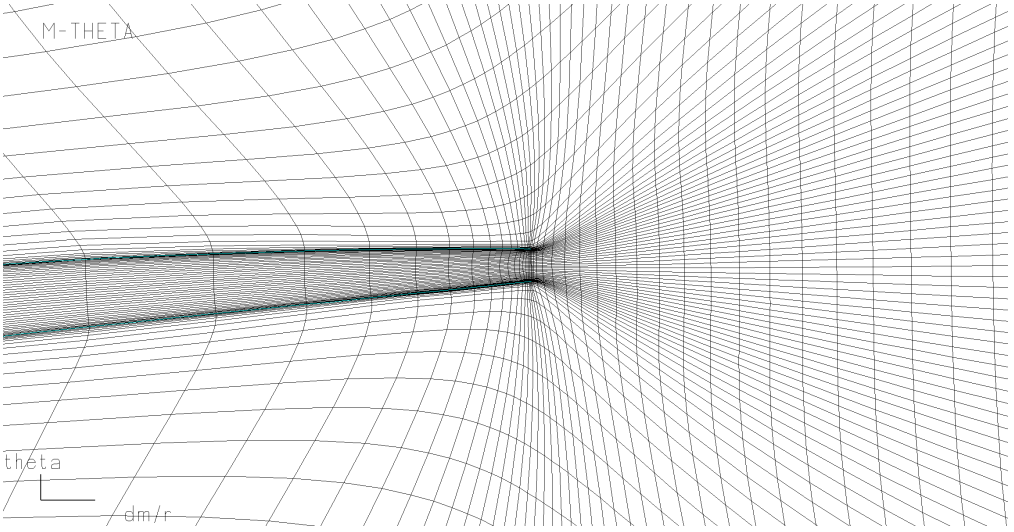

(b) Trailing edge.

Figure C.4: Shroud B2B views of the O-Rotor.

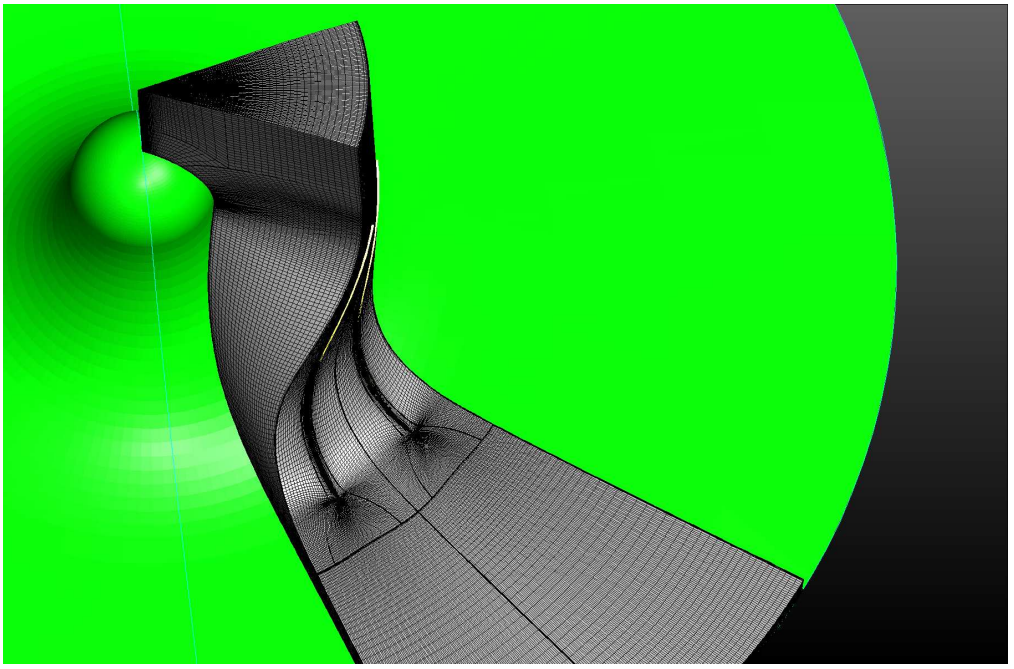

Figure C.5: Block wire mesh of the hyperbolic contoured O-Rotor.

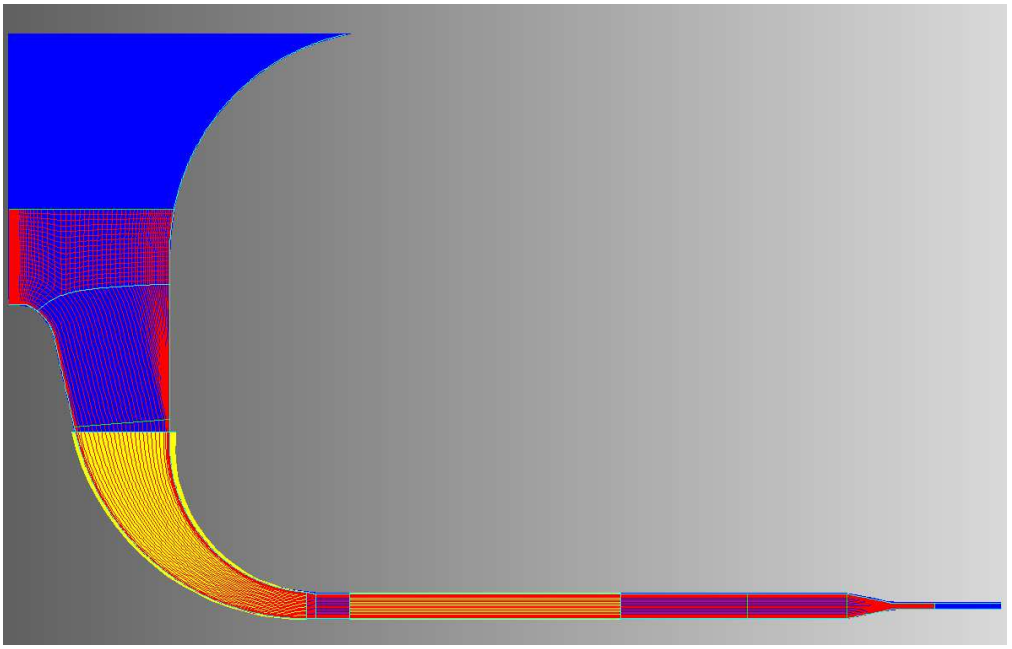

Figure C.6: Meridional (r-Z) view of the Radiver test case.

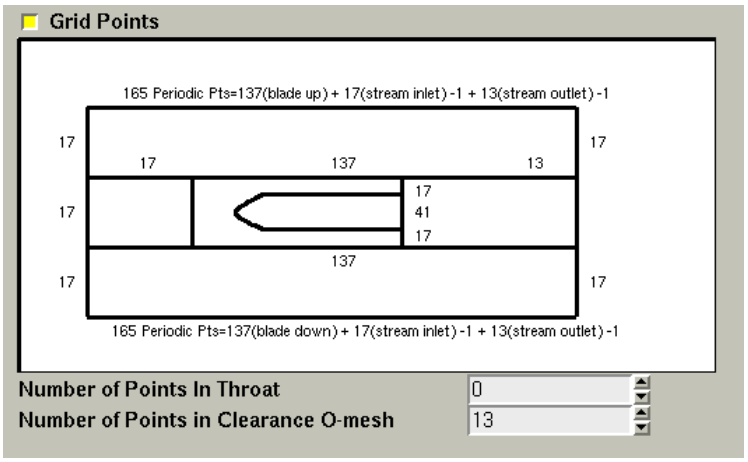

Figure C.7: Radiver test case impeller grid points summary.

The default (O4H) topology configuration with matching periodicity was chosen for the *"B2B Topology"*. A summary of the impeller B2B grid points can be viewed in Figure C.7. The appropriate cell width at all of the walls (except for the blade trailing edge where the default value of -1.0 was chosen again) was found to be 4.5 μm in order to achieve acceptable y^+ values (view Appendix E.2). The impeller blade surface cell width expansion ratio was set to 1.374. The default *"Optimization Properties"* for the impeller (100 B2B mesh optimization steps and 100 gap optimization steps) provided the best B2B mesh.

A butterfly type mesh at zero radius was chosen for the *"Bulb Topology"*. An additional *"Z-Constant"* line was added upstream (37 streamwise points) of the blade leading edge and *"Fixed Geometry"* was disabled. Samples of the impeller leading and trailing edge B2B meshes at the hub can be viewed in Figure C.8. Similar meshes for the impeller shroud can be viewed in Figure C.9.

For the diffuser section, 41 flow paths were used and the default layer control of 0 % (optimisation performed on every layer) was chosen. 33 % of the mid-flow paths were chosen as constant from H2S. The default (O4H) topology configuration with matching periodicity was chosen again for the *"B2B Topology"*. A summary of the diffuser B2B grid points can be viewed in Figure C.10. The appropriate cell width at the hub, shroud and vane walls were found to be 5 μm. The vane leading and trailing edge wall cell widths were chosen as 3.5 μm and 7 μm respectively to achieve acceptable y^+ values. Appendix E.2 provides proof of the y^+ values. The vane surface cell width expansion ratio was chosen as 1.4. The default *"Optimization Properties"* for the diffuser were chosen again to provide the best B2B mesh.

Two additional *"Z-Constant"* lines were added downstream (21 and 45 streamwise points respectively) of the trailing edge to improve the mesh. The last *"Z-Constant"* line was added at the beginning of the pinch to accommodate the change in direction of the end-walls. *"Fixed Geometry"* was disabled

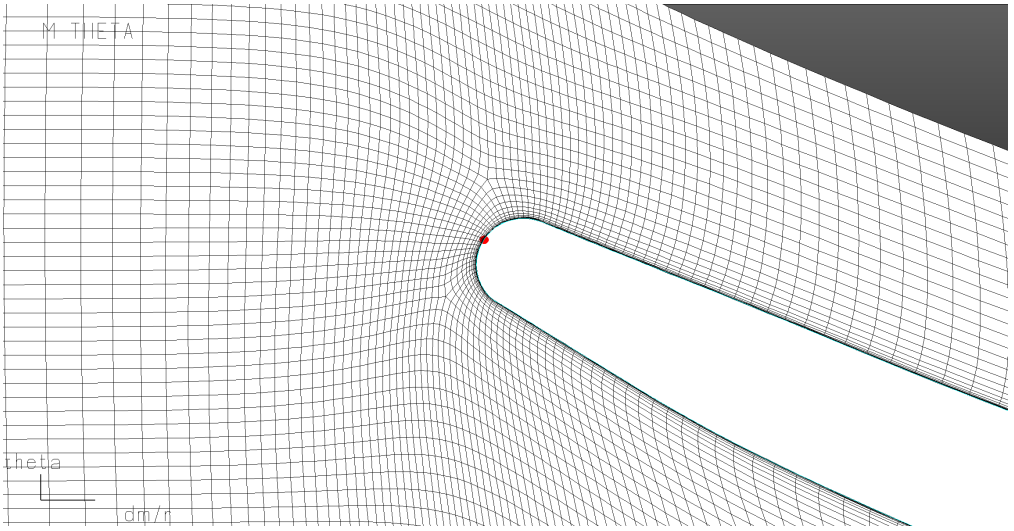

(a) Leading edge.

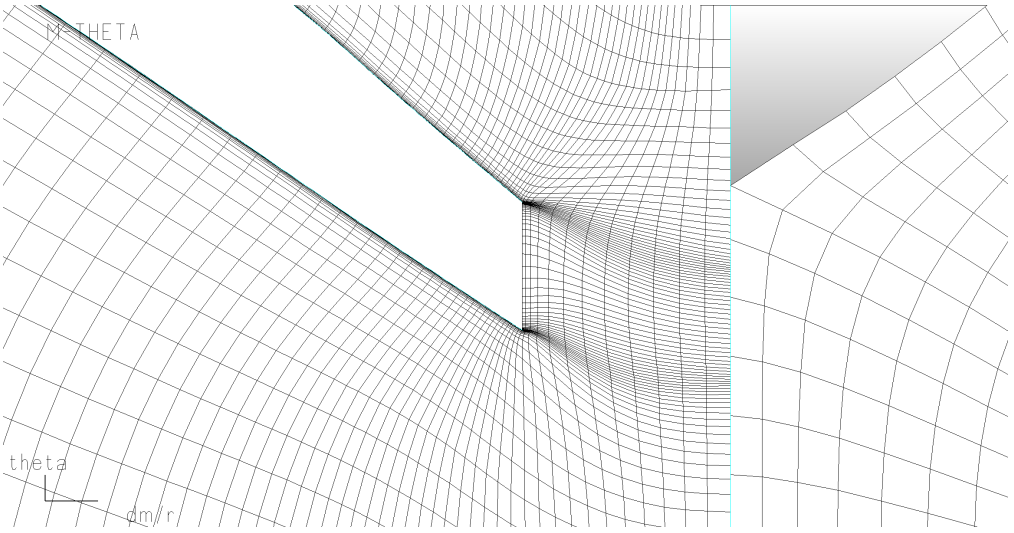

(b) Trailing edge.

Figure C.8: Hub B2B mesh views of the Radiver test case impeller.

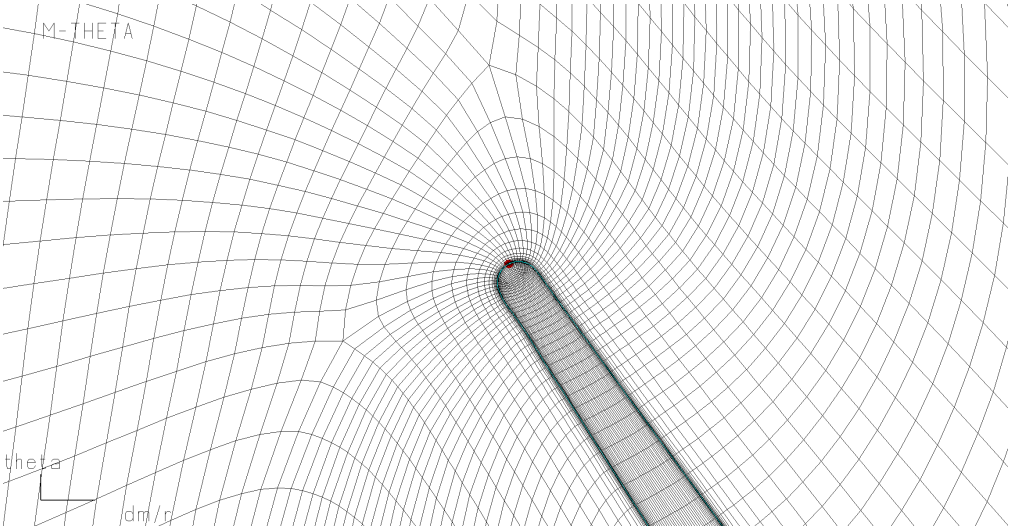

(a) Leading edge.

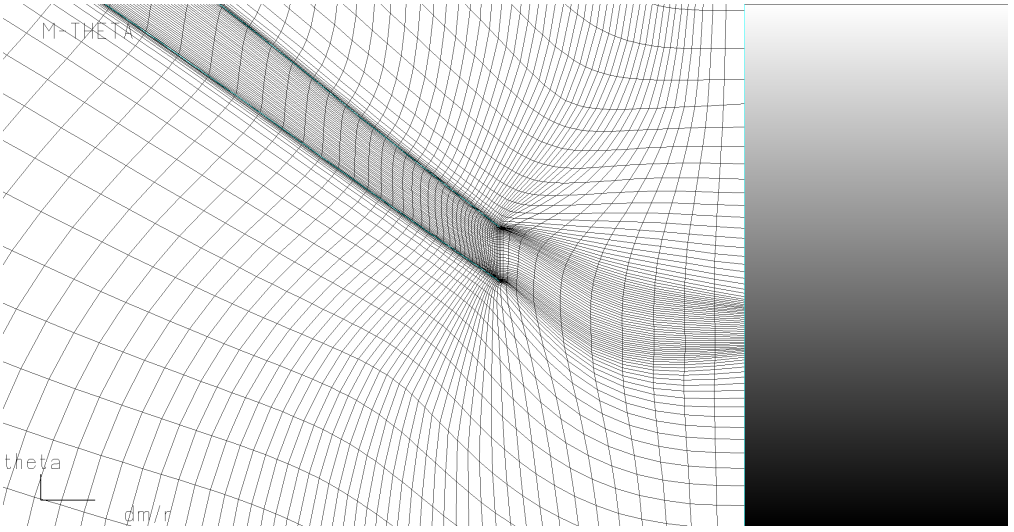

(b) Trailing edge.

Figure C.9: Shroud B2B mesh views of the Radiver test case impeller.

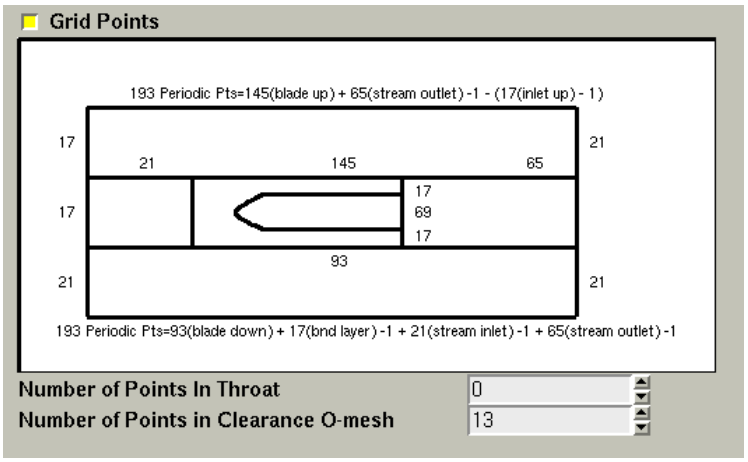

Figure C.10: Radiver test case diffuser grid points summary.

Table C.2: Radiver test case B2B mesh quality.

	Orthogonality	Aspect Ratio	Expansion Ratio
		Impeller	
Hub	34.37°	1442.3	2.39
Shroud	21.01°	925.03	3.49
		Diffuser	
Hub and Shroud	24.48°	729.88	3.22

for both lines. Samples of the diffuser leading and trailing B2B meshes at the hub can be viewed in Figure C.11. Due to the vertical vane walls, the shroud mesh is nearly identical to the hub mesh and is thus excluded.

The resulting mesh contained 2 204 864 grid points of which 997 865 grid points were in the impeller and 1 206 999 grid points were in the diffuser. A B2B quality summary of the entire compressor is provided in Table C.2. An AutoGrid5™ block wire mesh is provided in Figure C.12.

C.3 The DEEP Prototype

A meridional view of the DEEP prototype compressor is provided in Figure C.13 and AutoGrid5™ v8.7-2 was used to generate the 3-D mesh. For the impeller, 57 flow paths were used with 17 flow paths in the shroud gap. Layer control was set to 1 %. For the flow paths distribution from H2S, 60 % of the mid-flow paths were set as constant and 33 % were set as constant for the shroud gap. The shroud gap width at the leading and trailing edge was set to 1.3 mm and 1.8 mm respectively and was obtained from shroud casing modifications provided by Van der Spuy (2003).

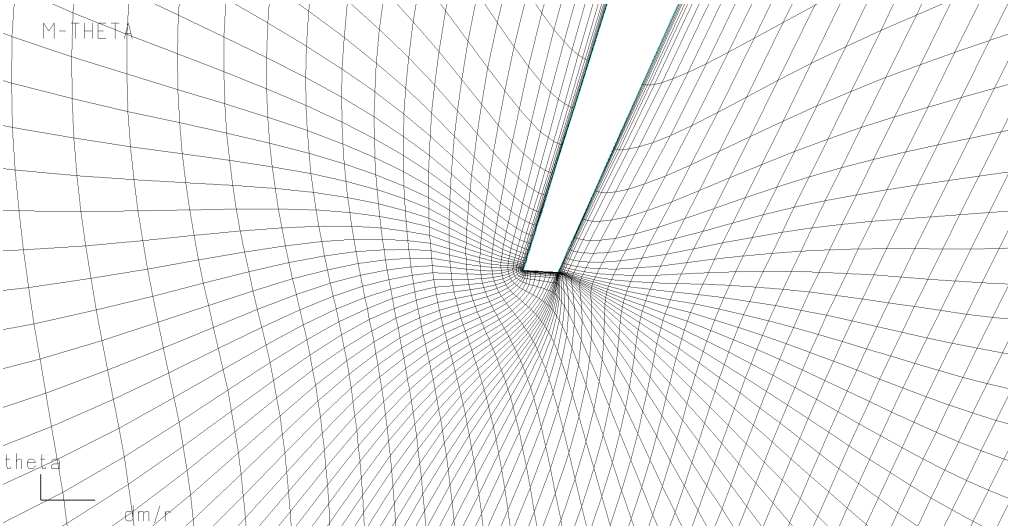

(a) Leading edge.

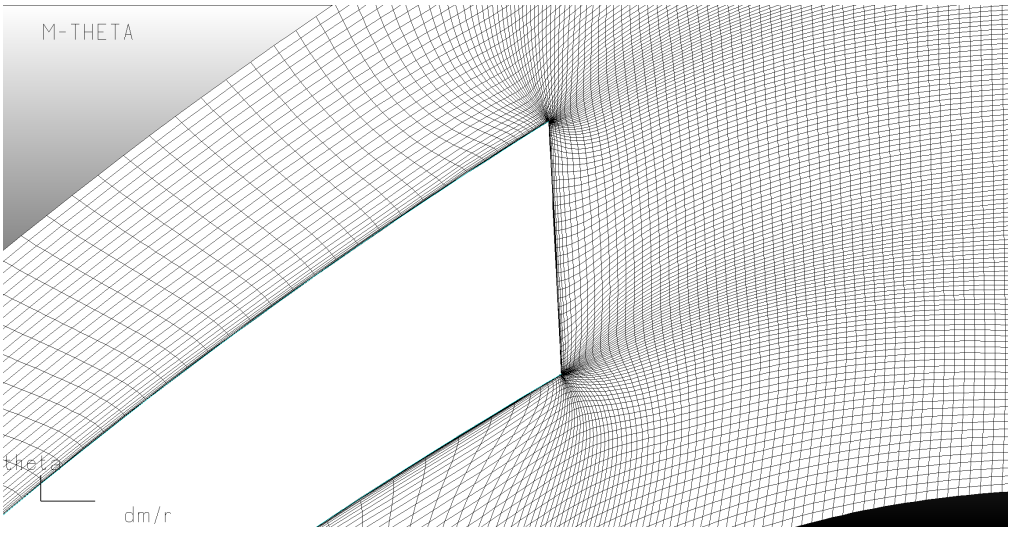

(b) Trailing edge.

Figure C.11: Hub B2B mesh views of the Radiver test case diffuser.

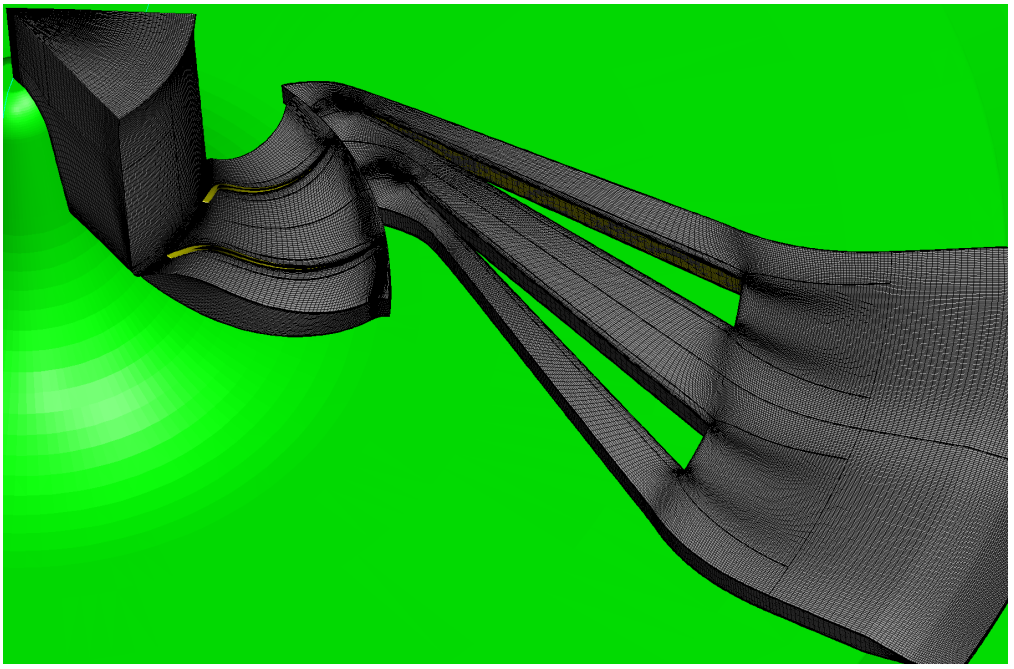

Figure C.12: Block wire mesh of the Radiver test case.

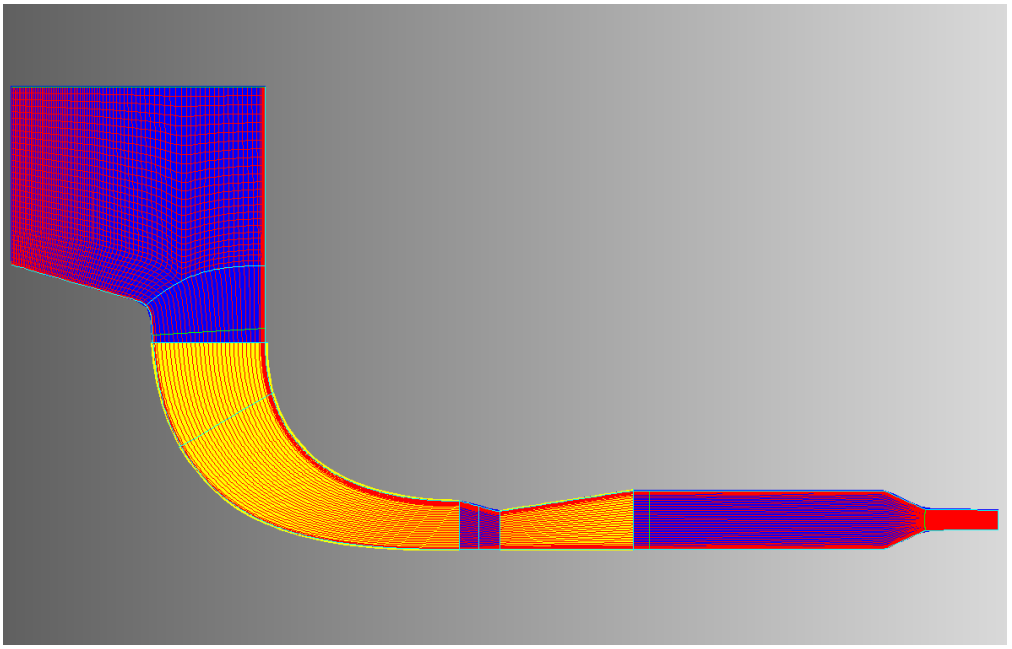

Figure C.13: Meridional (r-Z) view of the DEEP prototype.

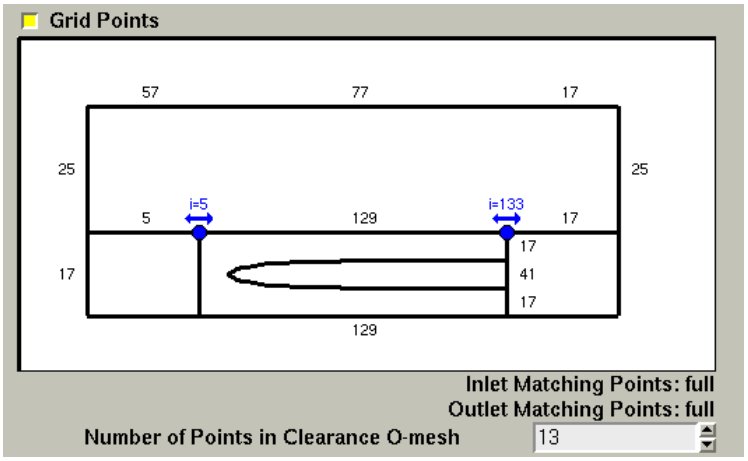

(a) Main blade.

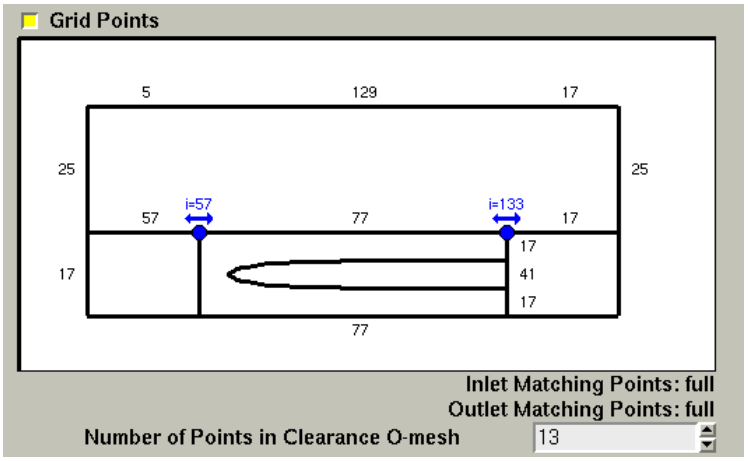

(b) Splitter blade.

Figure C.14: DEEP prototype impeller grid points summary.

The H&I topology configuration with matching periodicity was chosen for the *"B2B Topology"*. This topology provides a better grid where splitter blades are present (AutoGrid5™ Manual, 2010), which was confirmed after initially using the default (O4H) topology for the DEEP prototype. Summaries of the impeller main and splitter blade B2B grid points are provided in Figure C.14. Adherence to match the main and splitter blade meshes can be seen in the number of grid points of the B2B topologies.

The appropriate cell width at the hub was found to be 3.5 μm with 3.8 μm at the shroud and 3.0 μm at the main and splitter blade walls. The cell width at the main and splitter blade trailing edges was again set to the default of -1.0. These cell widths produced acceptable y^+ values as seen in Appendix E.3. The impeller blade surface cell width expansion ratio was set to 1.45. 310 B2B mesh optimization steps and 50 gap optimization steps for the impeller's *"Optimization Properties"* provided the best B2B mesh.

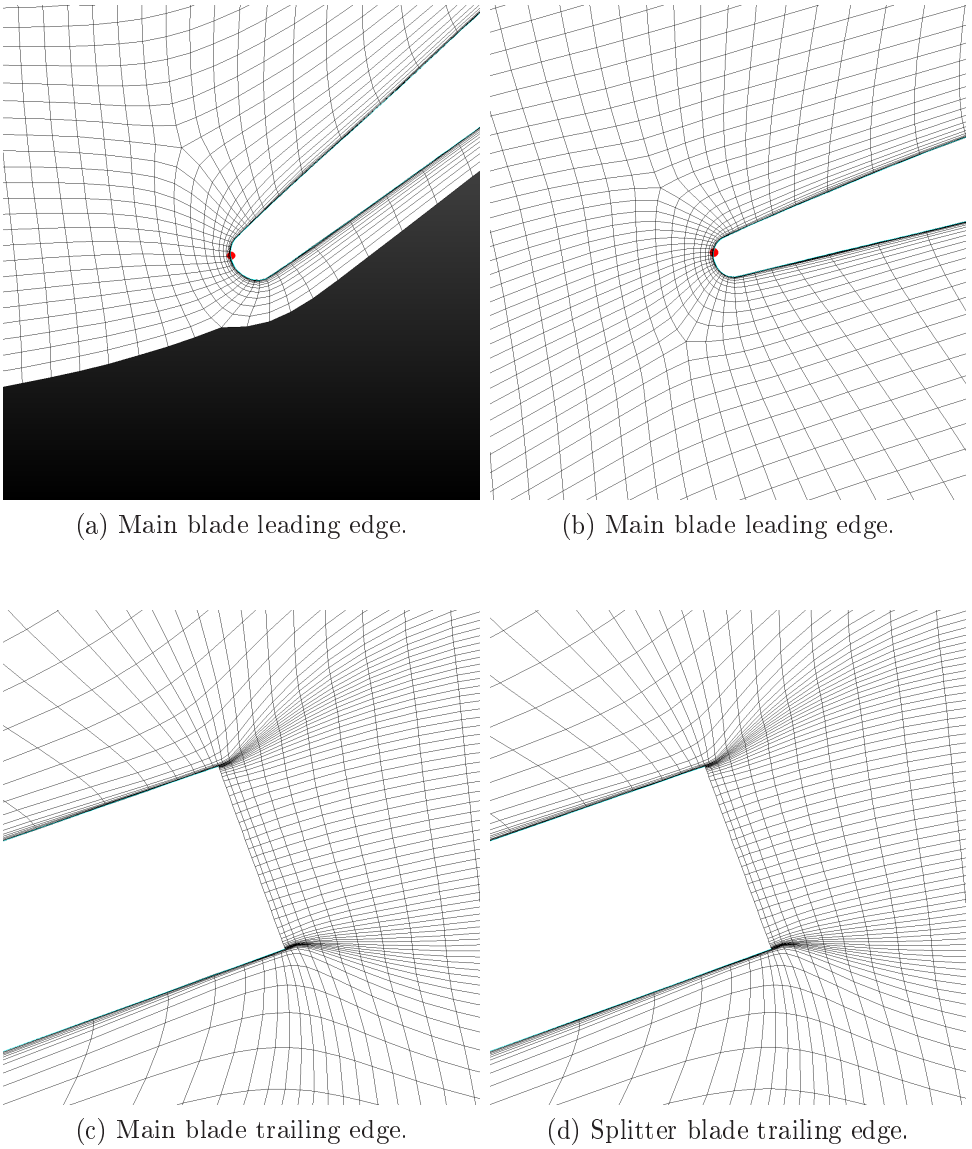

(a) Main blade leading edge.

(b) Main blade leading edge.

(c) Main blade trailing edge.

(d) Splitter blade trailing edge.

Figure C.15: Hub B2B views of the DEEP prototype impeller.

A butterfly type mesh at zero radius was chosen for the *"Bulb Topology"*. An additional *"Z-Constant"* line was added upstream (17 streamwise points) of the blade leading edge and *"Fixed Geometry"* was disabled. Samples of the impeller leading and trailing edge B2B meshes at the hub can be viewed in Figure C.15 with impeller shroud meshes provided in Figure C.16.

For the diffuser section, 57 flow paths were used and layer control was applied at 1 % intervals. 33 % of the H2S mid-flow paths were chosen as constant. The default topology configuration with matching periodicity was chosen for the diffuser's *"B2B Topology"*. A summary of the B2B grid points can be viewed in Figure C.17. The hub wall cell width was set to 3.5 μm, the shroud

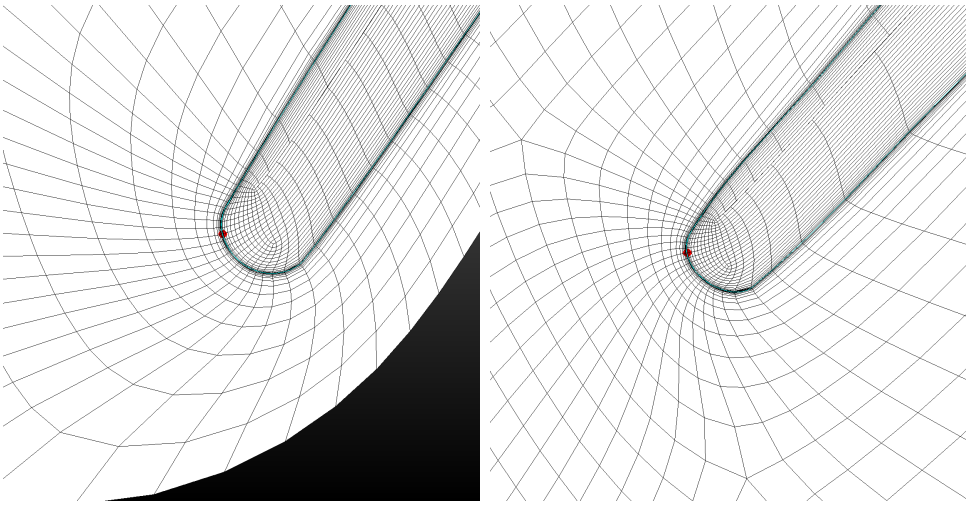

(a) Main blade leading edge. (b) Splitter blade leading edge.

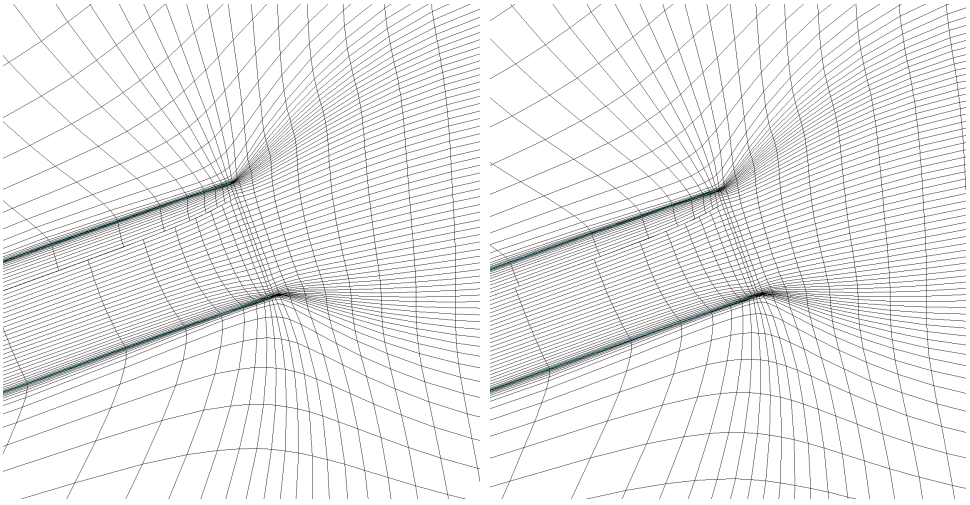

(c) Main blade trailing edge. (d) Splitter blade trailing edge.

Figure C.16: Shroud B2B views of the DEEP prototype impeller.

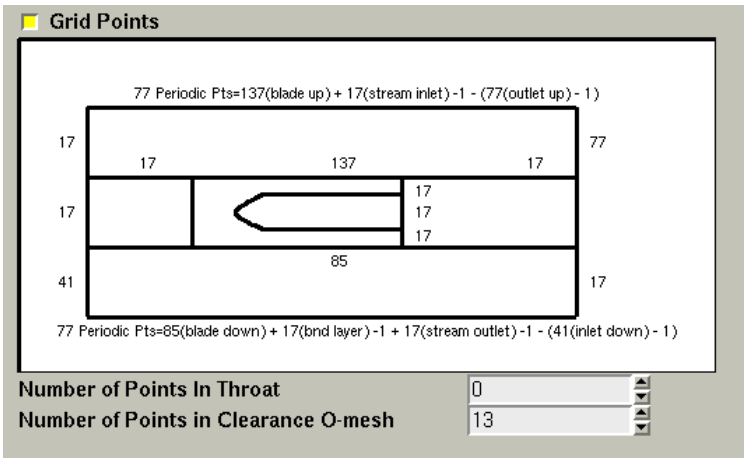

Figure C.17: DEEP prototype diffuser grid points summary.

wall cell width to 3.8 μm and the vane wall cell width to 3.0 μm. For the vane trailing edge wall cell width, the default value of -1.0 was chosen again. These wall cell widths provided acceptable y^+ values as shown in Appendix E.3. The vane surface cell width expansion ratio was chosen as 1.4. For the diffuser's *"Optimization Properties"*, 210 B2B mesh optimization steps and 100 gap optimization steps provided the best B2B mesh.

Two additional *"Z-Constant"* lines were added downstream of the trailing edge, with 53 and 21 streamwise points respectively, to improve the mesh. The last *"Z-Constant"* line was again added at the beginning of the pinch to accommodate the change in direction of the end-walls. *"Fixed Geometry"* was disabled for the first line and enabled for the second line to avoid distortion of the cells in the pinching region. Samples of the diffuser leading and trailing B2B meshes at the hub can be viewed in Figure C.18, with the nearly identical shroud mesh being excluded again.

The resulting mesh consisted of 2 634 405 grid points of which 1 544 451 grid points were in the impeller and 1 089 954 grid points were in the diffuser. A B2B quality summary of the entire compressor is provided in Table C.2. Figure C.19 shows an AutoGrid5™ block wire mesh of the DEEP prototype compressor.

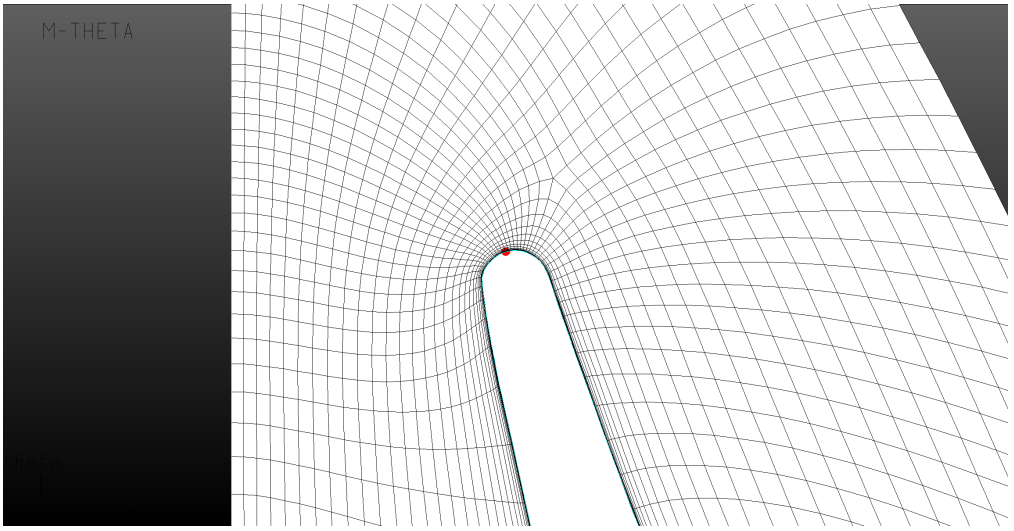

(a) Leading edge.

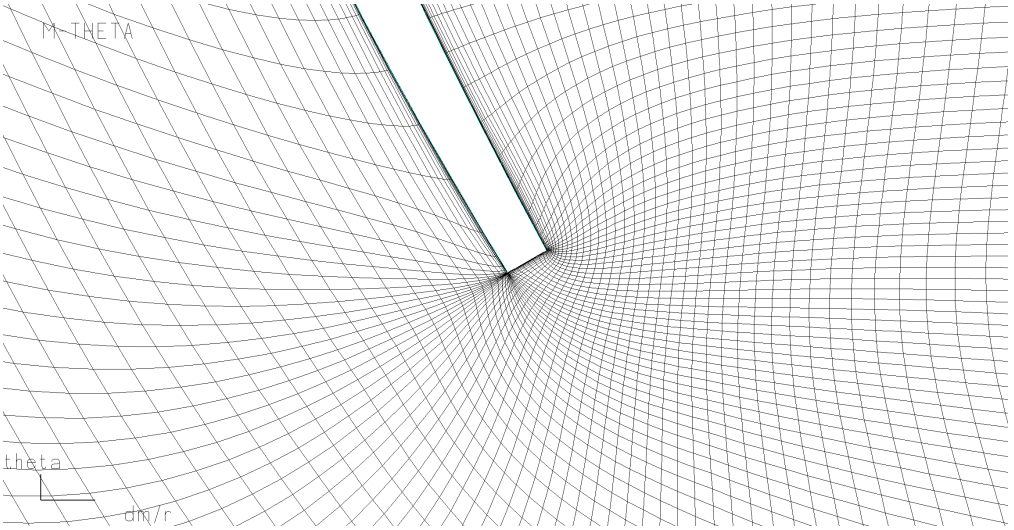

(b) Trailing edge.

Figure C.18: Hub B2B views of the DEEP prototype diffuser.

Table C.3: DEEP prototype B2B mesh quality.

	Orthogonality	Aspect Ratio	Expansion Ratio
		Impeller	
Hub	41.2°	1297.95	3.07
Shroud	35.94°	1029.26	3.05
		Diffuser	
Hub	34.36°	913.68	3.24
Shroud	34.39°	914.68	3.24

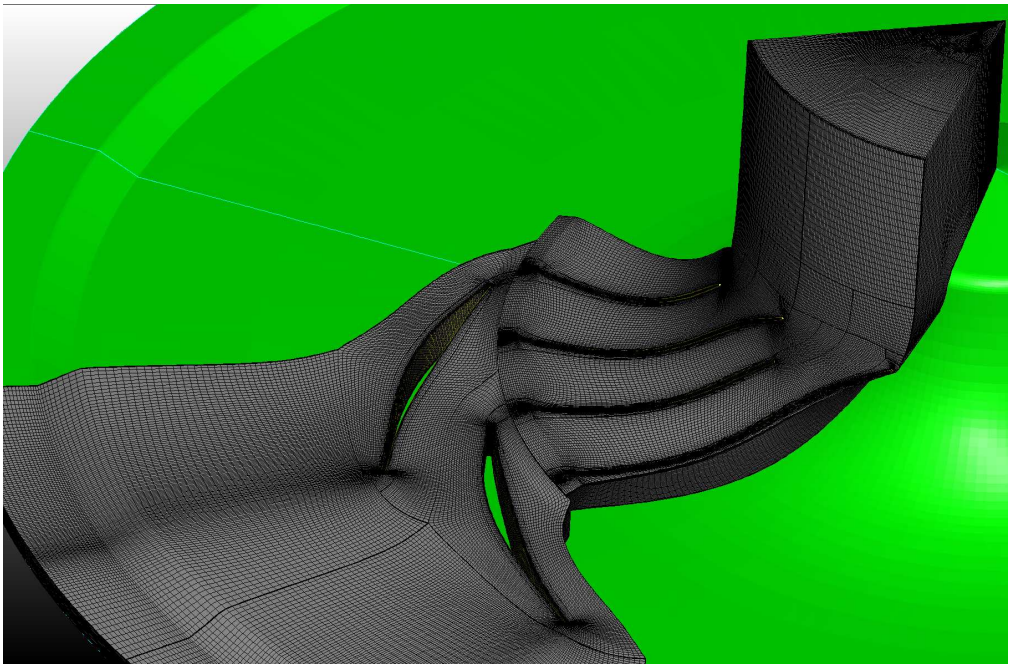

Figure C.19: Block wire mesh of the DEEP prototype.

Appendix D

FINE™/Turbo Setups of the Thesis Compressors

Information regarding the EURANUS™ solver setup of FINE™/Turbo (versions 8.4-3 and 8.7-2) for the thesis compressors are supplied in this section. The solver setup contains seven overall groups. Only two of these need to be supplied, *"Configuration"* and *"Boundary Conditions"*, as the other groups are user specific. Parameters for the compressor cases are summarised in Tables D.1 and D.2. Backflow control was enabled for all the compressors at the *"Outlet"* boundary condition.

Most of the solver setup is identical for all of the compressors. Thus, the identical information was grouped under one heading, *"All Cases"*. The only expert parameter enabled in *"Computation Steering > Control Variables > Integer Parameters"* was *"TORRO"*. This is to calculate the force and torque of the area defined rotating solids only (FINE™/Turbo Manual, 2010) which in this case is the hub.

Table D.1: FINE™/Turbo *"Configuration"* setup of the thesis compressors.

All Cases		
Fluid Model	Air (Perfect Gas)	
Flow Model	Time Configuration	Steady
	Mathematic Model	Turbulent Navier-Stokes
	Modelling of Turbulence	Spalart-Allmaras
Eckardt's O-Rotor		
Flow Model	Re_D Related Info	Charac. length = 0.14 m
		Charac. velocity = 80.0 m/s
		Charac. density = 1.225 kg/m^3
	Reference Values	Ref. temperature = 288.1 K
		Ref. pressure = 101 325 Pa
Rotating Machinery	Rotating Blocks	Impeller = −14 000 RPM
Radiver Test Case		
Flow Model	Re_D Related Info	Charac. length = 0.0722 m
		Charac. velocity = 135.0 m/s
		Charac. density = 1.2 kg/m^3
	Reference Values	Ref. temperature = 296 K
		Ref. pressure = 60 000 Pa
Rotating Machinery	Rotating Blocks	Impeller = 28 541 RPM
		Diffuser = 0 RPM
	Rotor-Stator	Non Reflecting 1-D (ID10)
DEEP Prototype		
Flow Model	Re_D Related Info	Charac. length = 0.122 m
		Charac. velocity = 130.0 m/s
		Charac. density = 1.18 kg/m^3
	Reference Values	Ref. temperature = 298 K
		Ref. pressure = 101 000 Pa
Rotating Machinery	Rotating Blocks	Impeller = −19 210 RPM
		Diffuser = 0 RPM
	Rotor-Stator	Full Non Matching Mixing Plane (ID10)

Table D.2: FINE™/Turbo *"Boundary Condition"* setup of the thesis compressors.

All Cases
Inlet ⇒ Total Quantities Imposed ⇒ Angle from Axial Direction (V Extrapolated)
⇒ arctg(Vt/Vz) = 0 rad
⇒ arctg(Vr/Vz) = 0 rad
⇒ Turbulent Viscosity = 0.0001 m^2/s
Solid ⇒ Adiabatic ⇒ Constant Rotation Speed
⇒ Shroud = 0 RPM
⇒ Area Defined Rotation Speed (Hub)
⇒ w_1 = 0 RPM
⇒ Rmin = 0 m
⇒ Zmin and Zmax adequately chosen
Eckardt's O-Rotor
Inlet ⇒ Total Quantities Imposed ⇒ Angle from Axial Direction (V Extrapolated)
⇒ Absolute Total Pressure = 101 325 Pa
⇒ Absolute Total Temperature = 288.1 K
Outlet ⇒ Mass Flow Imposed ⇒ Velocity Scaling
Solid ⇒ Adiabatic ⇒ Constant Rotation Speed
⇒ Blade = −14 000 RPM
⇒ Area Defined Rotation Speed (Hub)
⇒ w_2 = −14 000 RPM
⇒ Rmax = 0.2 m
Radiver Test Case
Inlet ⇒ Total Quantities Imposed ⇒ Angle from Axial Direction (V Extrapolated)
⇒ Absolute Total Pressure = 60 000 Pa
⇒ Absolute Total Temperature = 296 K
Outlet ⇒ Pressure Imposed ⇒ Static Pressure Imposed
Solid ⇒ Adiabatic ⇒ Constant Rotation Speed
⇒ Impeller Blade = 28 541 RPM
⇒ Diffuser Blade = 0 RPM
⇒ Area Defined Rotation Speed (Hub)
⇒ w_2 = 28 541 RPM
⇒ Rmax = 0.135 m
DEEP Prototype
Inlet ⇒ Total Quantities Imposed ⇒ Angle from Axial Direction (V Extrapolated)
⇒ Absolute Total Pressure = 101 000 Pa
⇒ Absolute Total Temperature = 298 K
Outlet ⇒ Mass Flow Imposed ⇒ Velocity Scaling
Solid ⇒ Adiabatic ⇒ Constant Rotation Speed
⇒ Impeller Blade = −19 210 RPM
⇒ Diffuser Blade = 0 RPM
⇒ Area Defined Rotation Speed (Hub)
⇒ w_2 = −19 210 RPM
⇒ Rmax = 0.215 m

Appendix E

y^+ Values of the Thesis Compressors

In order to demonstrate that the 3-D meshes and solver setups for all of the compressor cases were correct, the y^+ value plots from CFView™ are supplied in this section. As discussed in Section 2.3.2, the y^+ values are affected by the medium velocity and wall cell width. Thus only the y^+ values of the highest mass flow rate achieved during the 3-D simulations are presented.

E.1 The Eckardt O-Rotor

y^+ values obtained during the turbulence model comparison of Section 2.3.2 are shown in Figures E.1 and E.2. The decision was between the 1-equation model by Spalart and Allmaras (1992) ("S-A") and the standard k-ϵ with extended wall function model by Launder and Spalding (1974) ("k-ϵ"). As mentioned in Section 2.3.2, the recommended range of y^+ values for the S-A and k-ϵ models is $1 \leq y^+ \leq 10$ (FINE™/Turbo Manual, 2010). This is satisfied by Figures E.1 and E.2.

As mentioned in Section 2.3.2, the author aimed at achieving y^+ values lower than six for the thesis compressors. Some overshoot in areas of separation was acceptable. The reader can refer to Figures E.3 to E.5 for y^+ values of the O-Rotor, which shows y^+ values lower than six with the exception of the trailing edge.

E.2 The Radiver Test Case

y^+ values of the Radiver test case are provided in Figures E.6 to E.8. The y^+ values are predominately lower than six with some acceptable overshoot at the trailing edge.

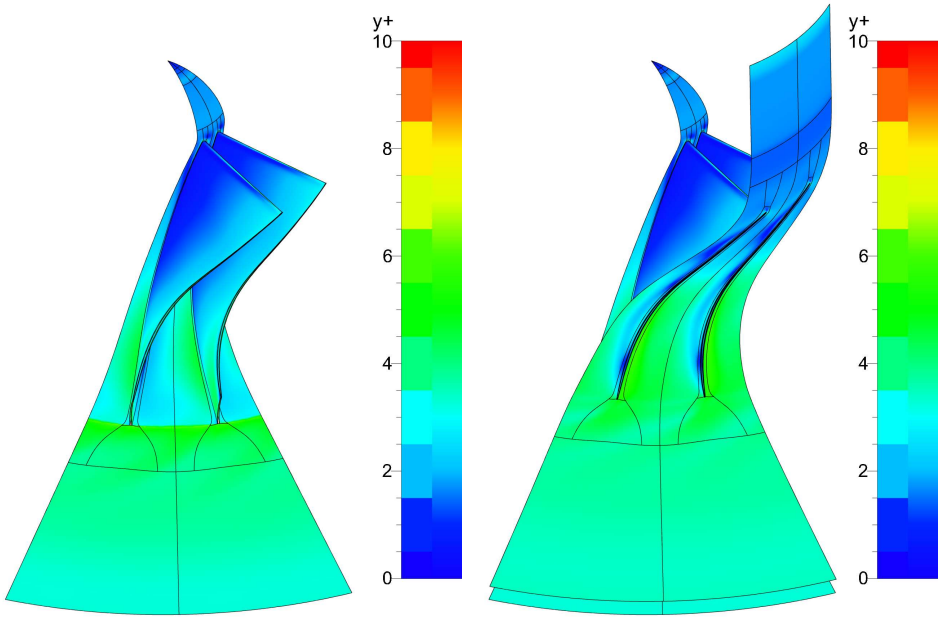

(a) Unshrouded. (b) Shrouded.

Figure E.1: y^+ values of the O-Rotor at 6.09 kg/s using the Spalart-Allmaras turbulence model.

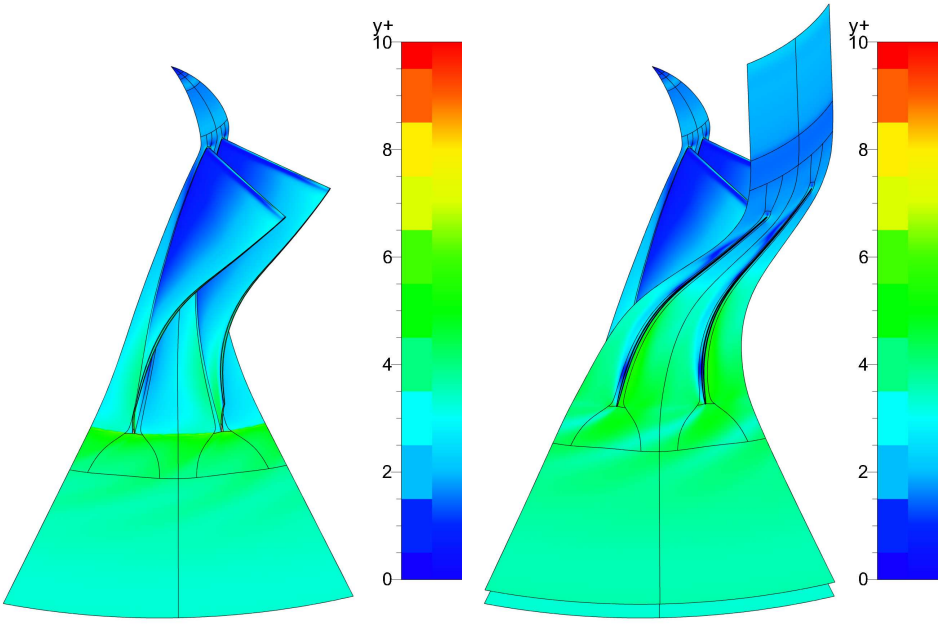

(a) Unshrouded. (b) Shrouded.

Figure E.2: y^+ values of the O-Rotor at 6.09 kg/s using the k-ϵ with extended wall function turbulence model.

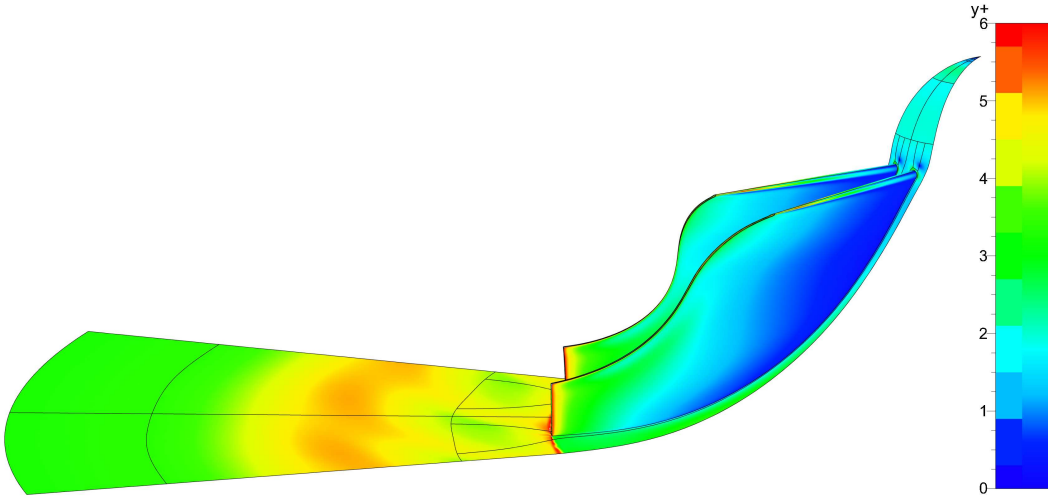

(a) Pressure surface.

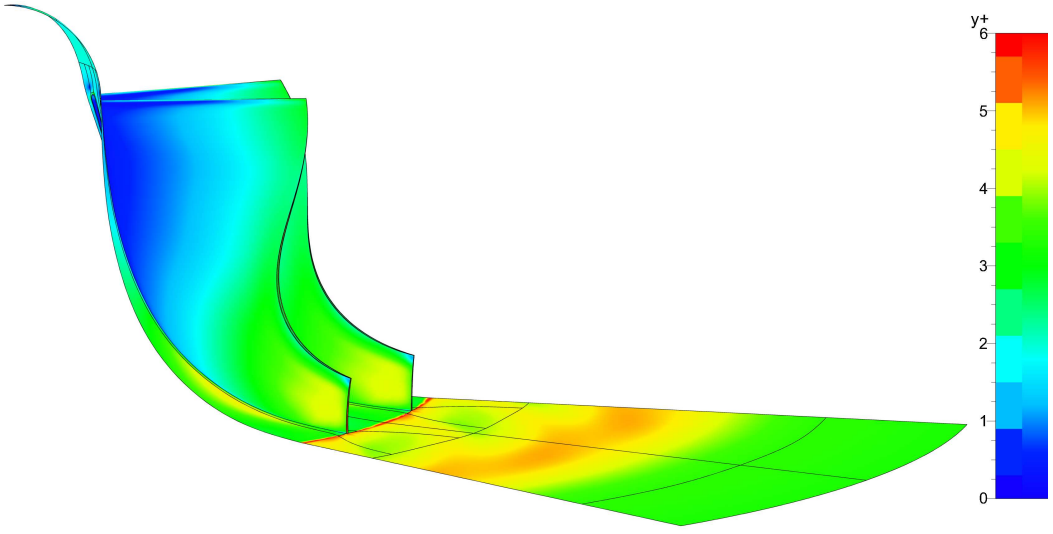

(b) Suction surface.

Figure E.3: Blade pressure and suction surface y^+ values of the O-Rotor at 6.19 kg/s.

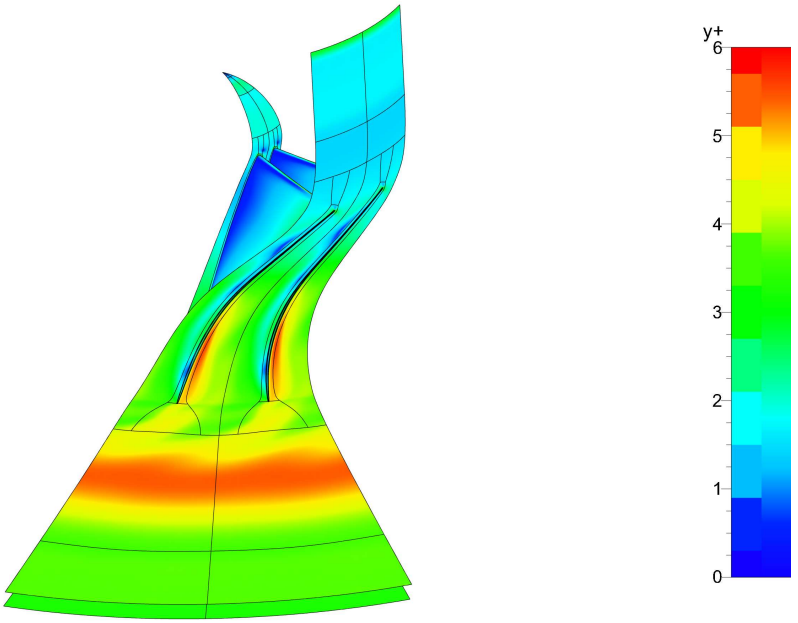

Figure E.4: Shrouded y^+ values of the O-Rotor at 6.19 kg/s.

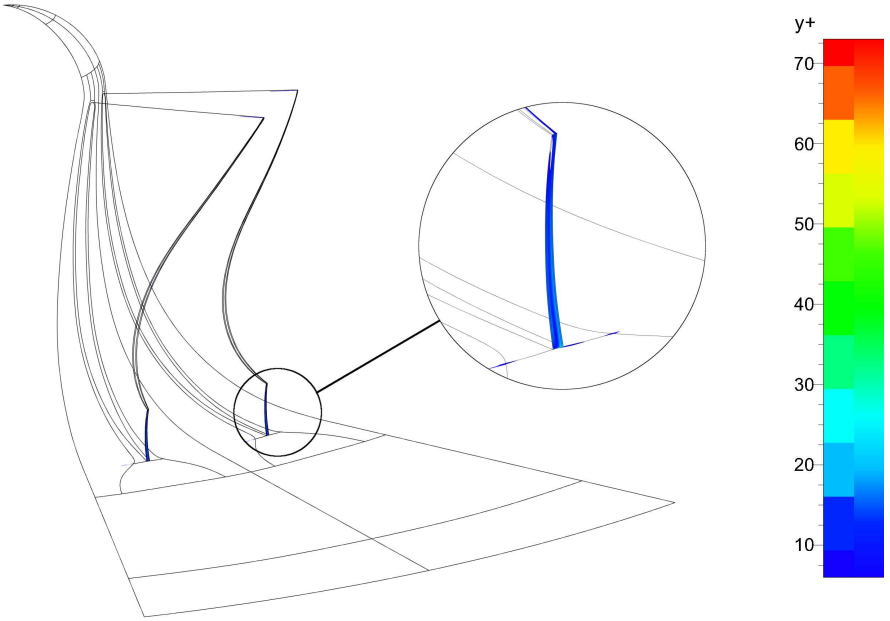

Figure E.5: y^+ values above six of the O-Rotor at 6.19 kg/s.

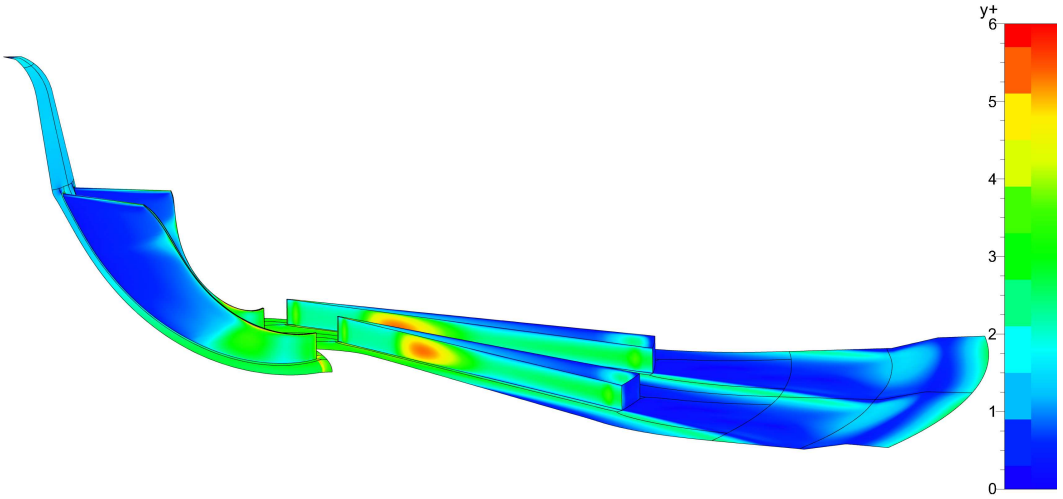

(a) Pressure surfaces.

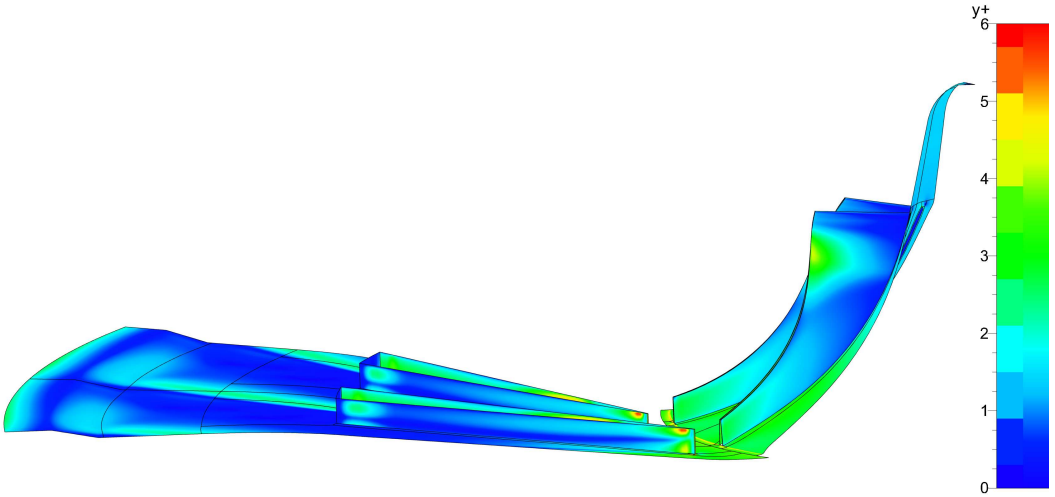

(b) Suction surfaces.

Figure E.6: Blade pressure and suction surfaces y^+ values of the Radiver test case at 2.161 kg/s.

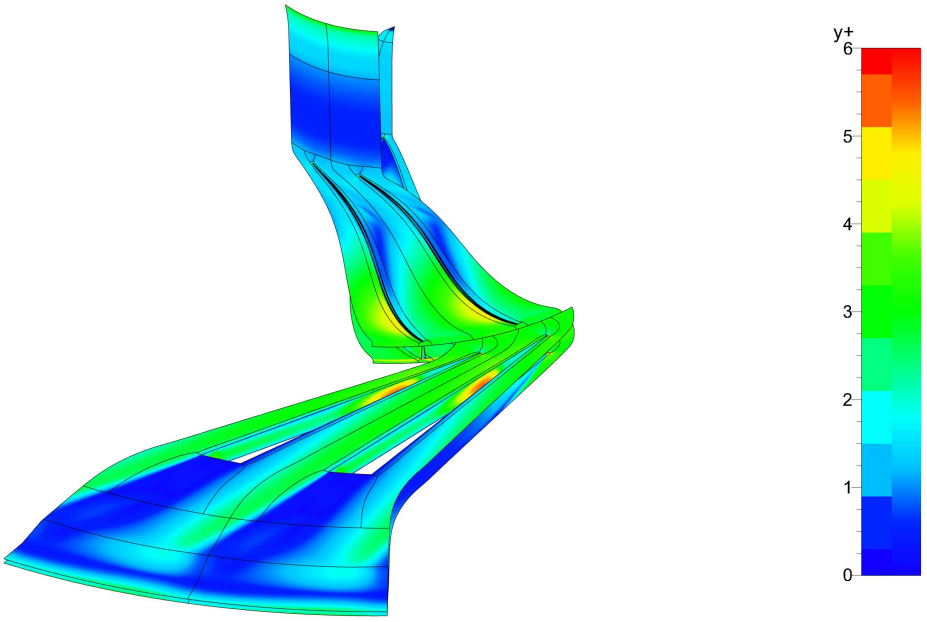

Figure E.7: Shrouded y^+ values of the Radiver test case at 2.161 kg/s.

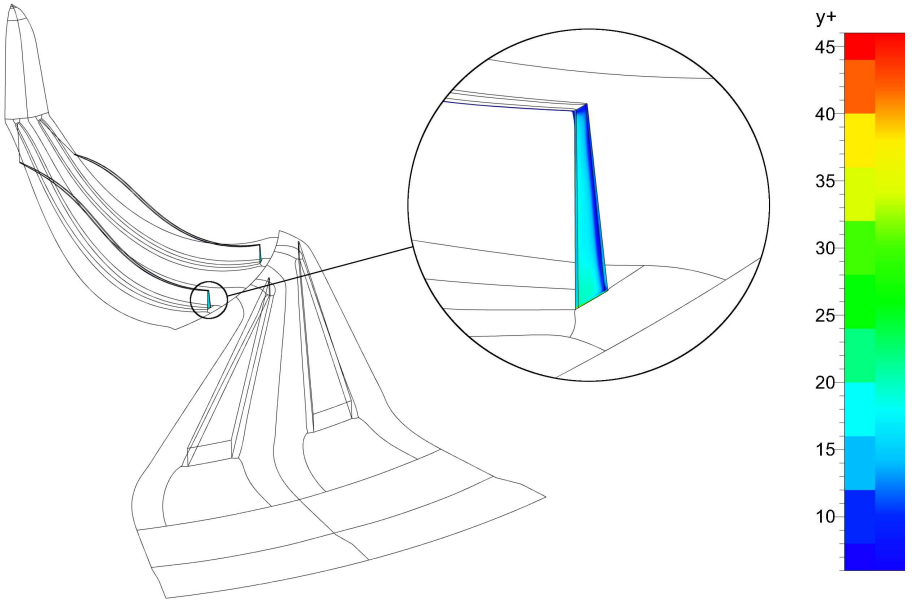

Figure E.8: y^+ values above six of the Radiver test case at 2.161 kg/s.

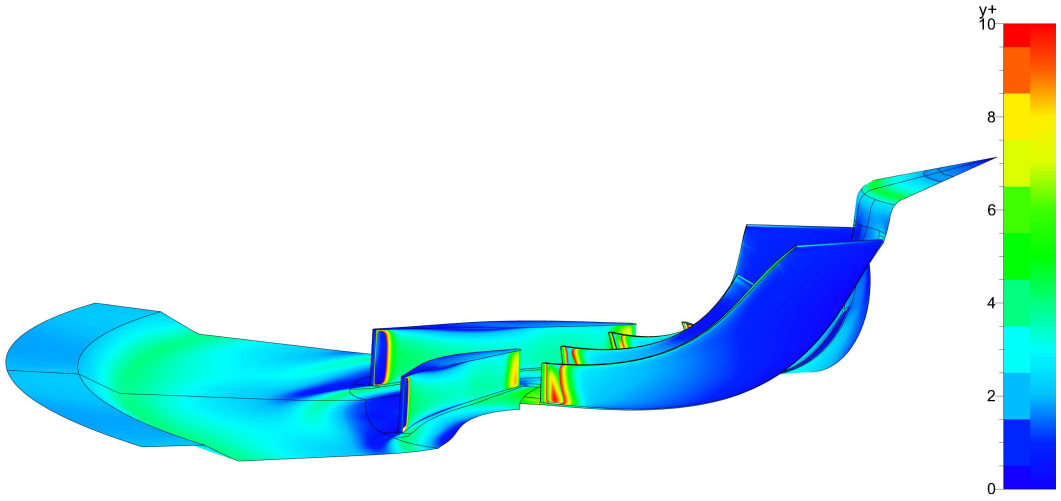

(a) Pressure surfaces.

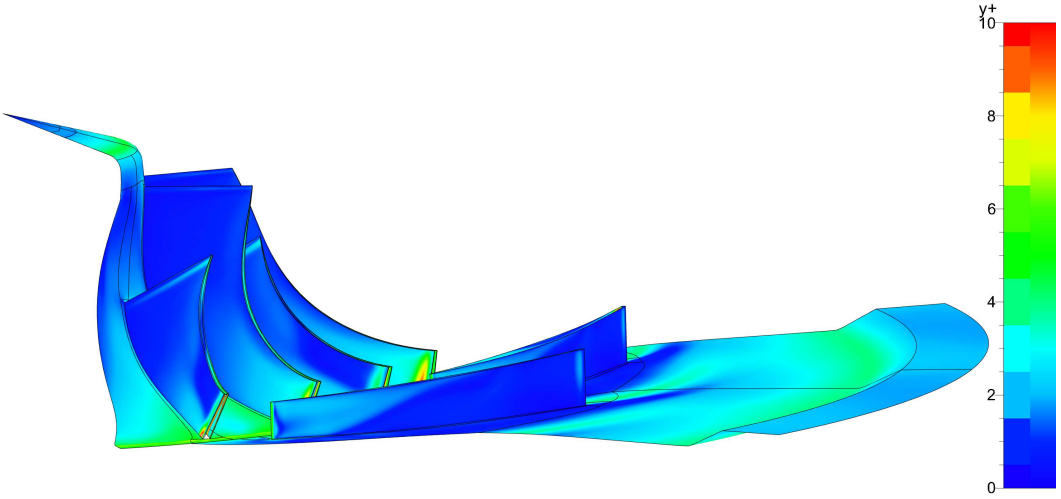

(b) Suction surfaces.

Figure E.9: Blade pressure and suction surfaces y^+ values of the DEEP prototype at 5.32 kg/s.

E.3 The DEEP Prototype

DEEP prototype y^+ values which are predominately below 10 were obtained with sufficient mesh refinement as shown in Figures E.9 and E.10. AutoGrid5™ v8.7-2 is unable to define a variable wall cell height along a blade surface, thus the patches with y^+ values larger than 10 in Figure E.11 could not be addressed without increasing the amount of cells significantly.

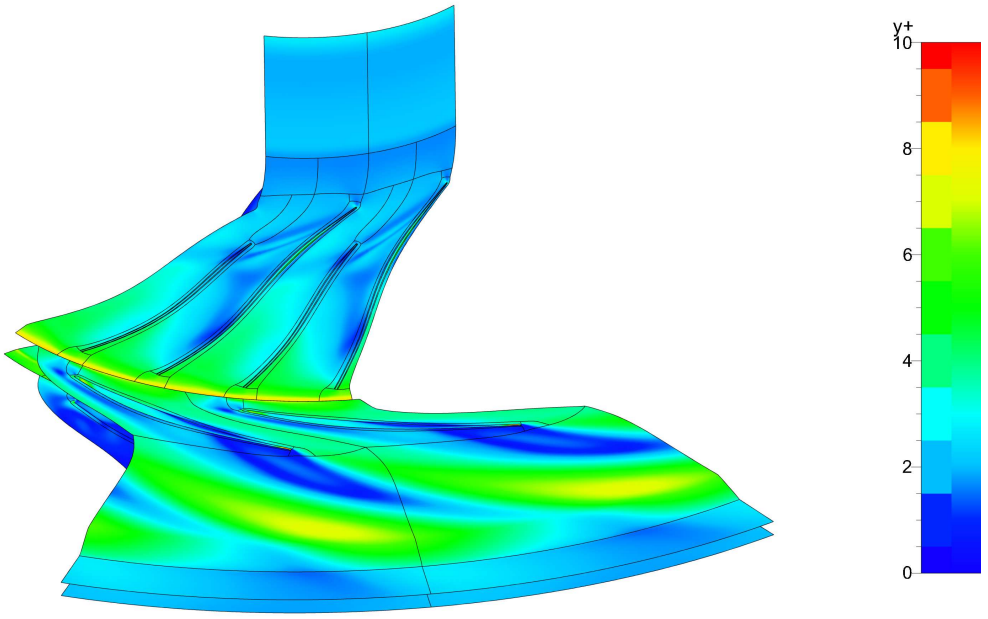

Figure E.10: Shrouded y^+ values of the DEEP prototype at 5.32 kg/s.

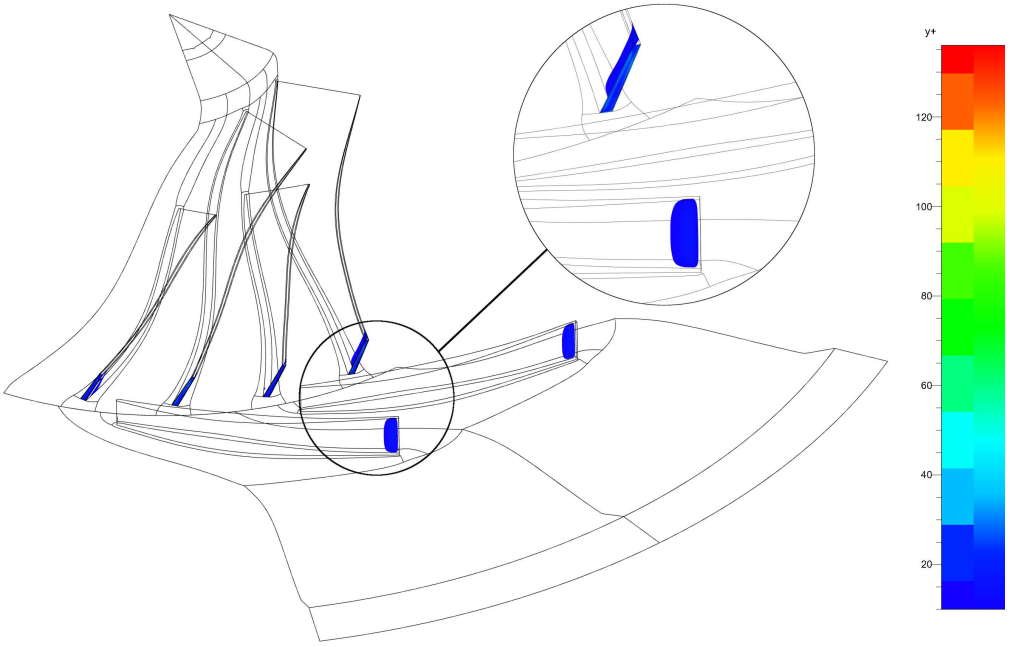

Figure E.11: y^+ values above 10 of the DEEP prototype at 5.32 kg/s.

Appendix F

O-Rotor Linear Tapered Shroud Results

Both a linear tapered and hyperbolic contoured shroud for the O-Rotor were investigated as discussed in Section 3.2.1, with results of the hyperbolic contoured shroud provided in Section 3.2.2. Results for the linear tapered shroud are provided in this section. The total-to-total pressure ratios and total-to-total efficiencies are shown in Figures F.1 and F.2.

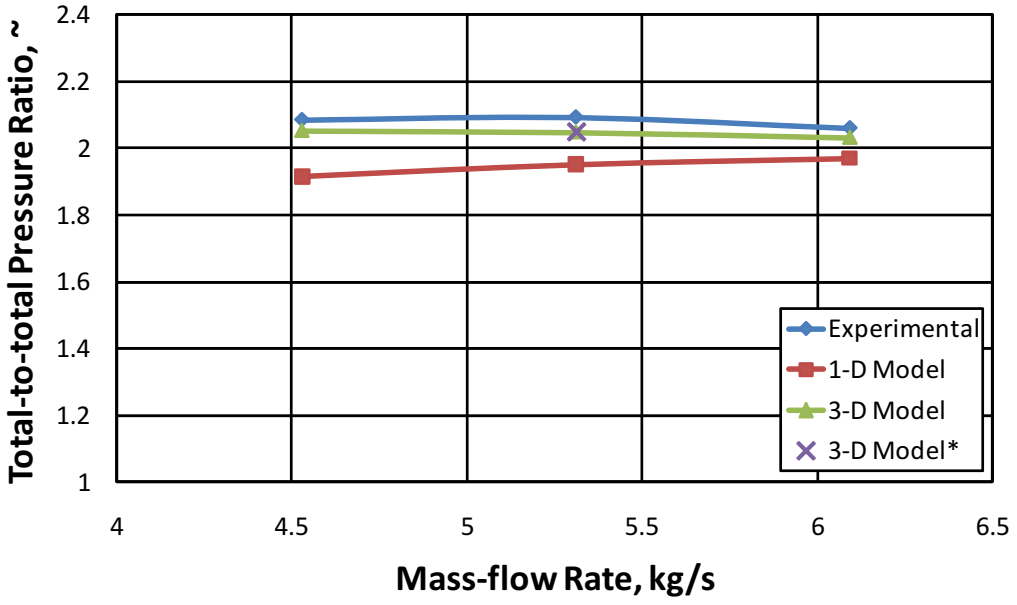

Figure F.1: Total-to-total pressure ratios of the O-Rotor with a linear tapered shroud at 14 000 RPM (Eckardt, 1975).

Pressure and flow angle results along the vaneless diffuser are provided in Figures F.4 and F.3.

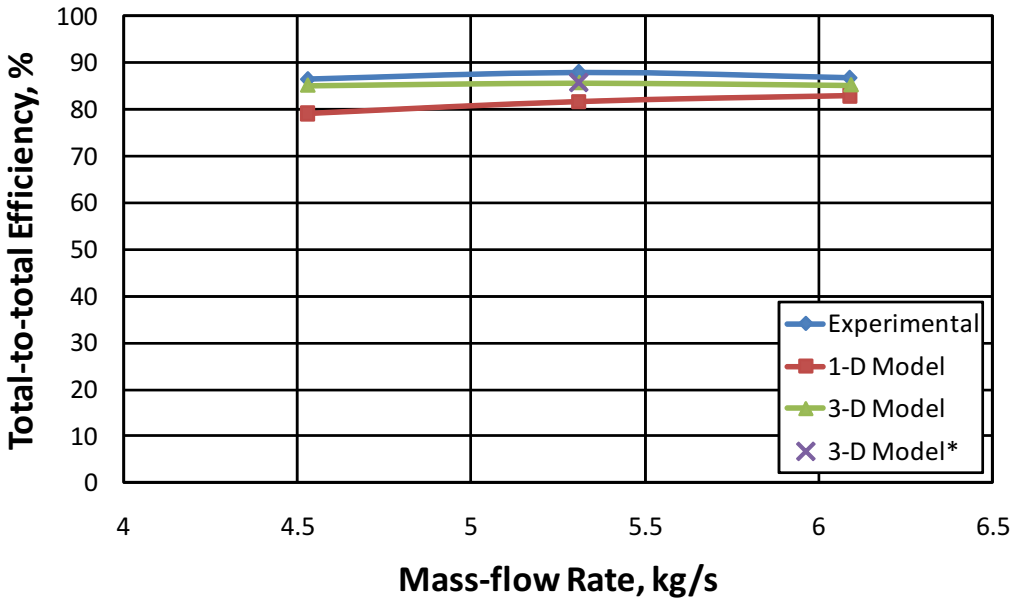

Figure F.2: Total-to-total efficiencies of the O-Rotor with a linear tapered shroud at 14 000 RPM (Eckardt, 1975).

Test results of the O-Rotor at 12 000 RPM by Eckardt and Trültzsch (1977) were obtained through Japikse and Oliphant (2005). Vaneless diffuser pressure and flow angle results at 3.86 kg/s are supplied in Figures F.5 and F.6.

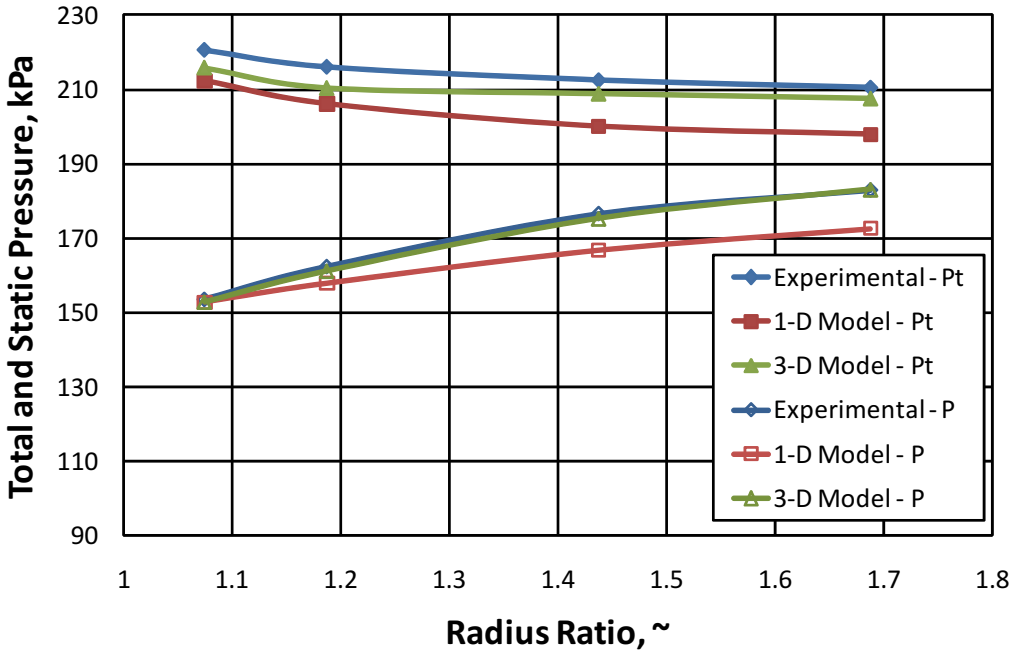

Figure F.3: Pressures along the diffuser of the O-Rotor with a linear tapered shroud at 14 000 RPM and 5.31 kg/s (Dubitsky and Japikse, 2008).

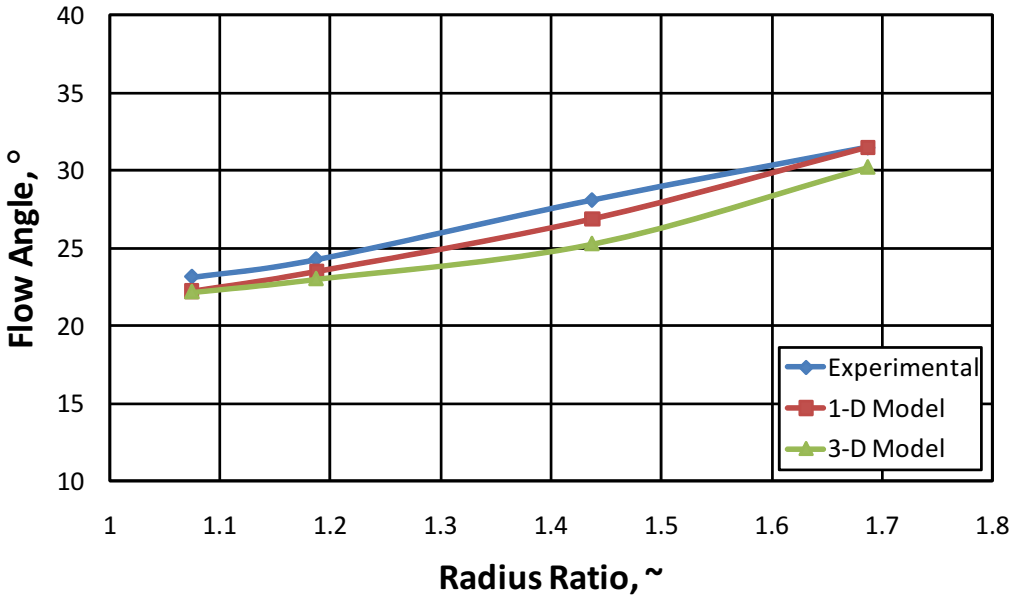

Figure F.4: Flow angles along the diffuser of the O-Rotor with a linear tapered shroud at 14 000 RPM and 5.31 kg/s (Dubitsky and Japikse, 2008).

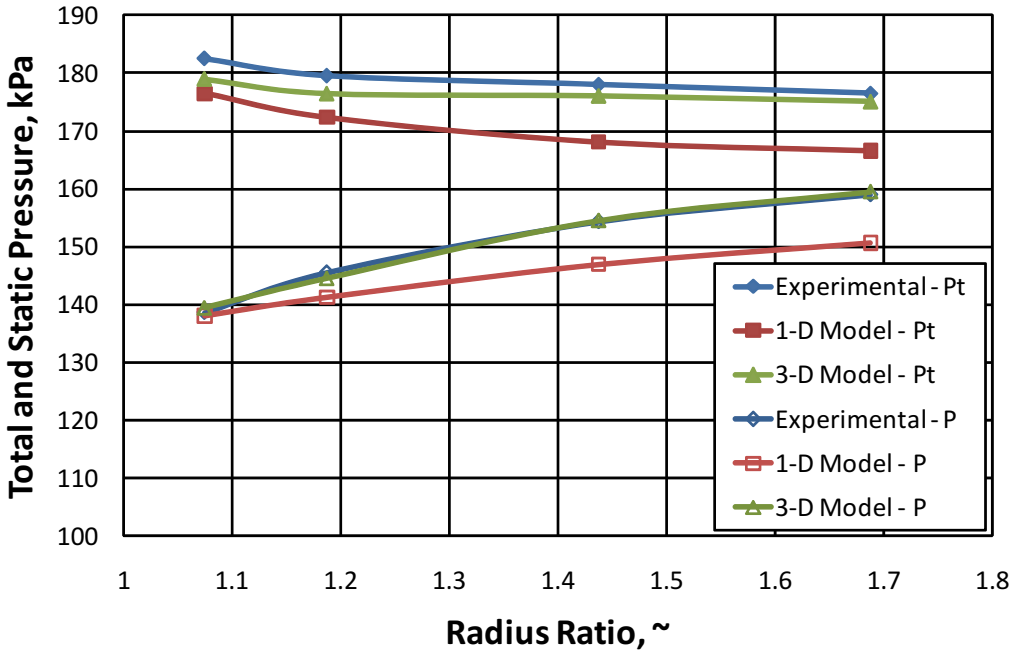

Figure F.5: Pressures along the diffuser of the O-Rotor with a linear tapered shroud at 12 000 RPM and 3.86 kg/s (Dubitsky and Japikse, 2008).

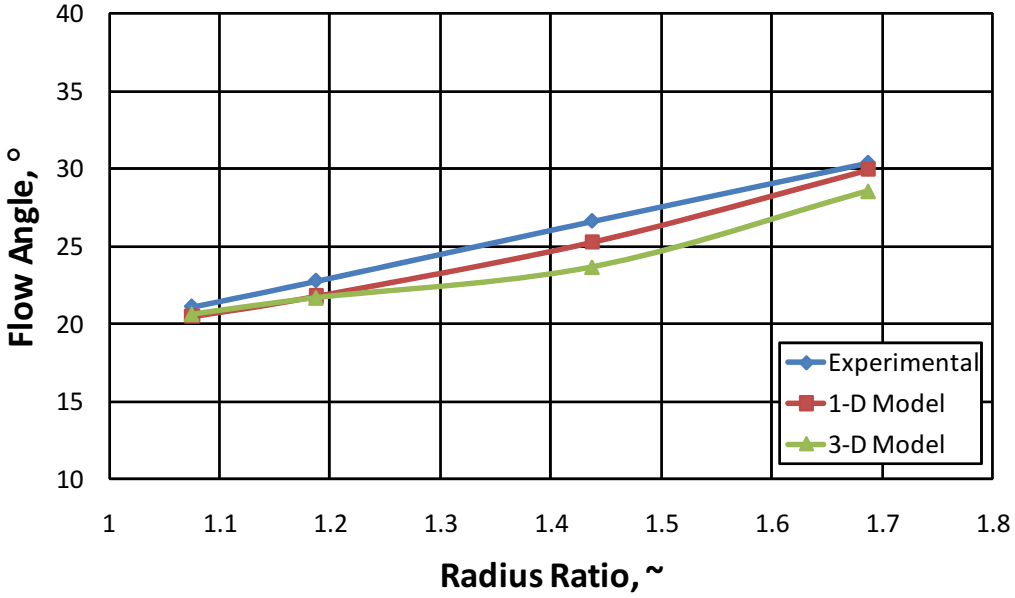

Figure F.6: Flow angles along the diffuser of the O-Rotor with a linear tapered shroud at 12 000 RPM and 3.86 kg/s (Dubitsky and Japikse, 2008).

List of References

Anderson, M.R. (2009). Optimization of Turbomachinery - Validation Against Experimental Results. Tech. Rep., Concepts NREC, White River Junction, Vermont, USA.

Aungier, R. (ed.) (1993 May). *Aerodynamic Design and Analysis of Vaneless Diffusers and Return Channels*. International Gas Turbine and Aeroengine Congress and Exposition, Cincinnati, Ohio.

Aungier, R.H. (1988). A Systematic Procedure for the Aerodynamic Design of Vaned Diffusers. *Flows in Non-Rotating Turbomachinery Components, ASME*, vol. 69, pp. 27–34.

Aungier, R.H. (1990). Aerodynamic performance analysis of vaned diffusers. *Fluid Machinery Components, ASME FED*, vol. 101, pp. 37–44.

Aungier, R.H. (1995 July). Mean Streamline Aerodynamic Performance Analysis of Centrifugal Compressors. *Journal of Turbomachinery, ASME*, vol. 117, pp. 360–366.

Aungier, R.H. (2000). *Centrifugal Compressors - A Strategy for Aerodynamic Design and Analysis*. ASME Press, New York.

Baldwin, B. and Lomax, H. (1978 January). Thin Layer Approximation and Algebraic Model for Separated Turbulent Flows. *AIAA-Paper 78-257*.

Benedict, R., Carlucci, N. and Swetz, S. (1966 January). Flow Losses in Abrupt Enlargements and Contractions. *Journal of Engineering for Power, ASME*, vol. 88, pp. 73–81.

Chien, K.Y. (1982). Predictions of Channel and Boundary-Layer Flows with a Low-Reynolds Number Turbulence Model. *AIAA*, vol. 20, no. 1, pp. 33–38.

Daily, J. and Nece, R.E. (1960 March*a*). Chamber Dimension Effects on Induced Flow and Frictional Resistance of Enclosed Rotating Discs. *Journal of Basic Engineering, ASME*, vol. 82, pp. 217–232.

Daily, J. and Nece, R.E. (1960 September*b*). Roughness Effects on Frictional Resistance of Enclosed Rotating Disks. *Journal of Basic Engineering, ASME*, vol. 82, pp. 553–562.

Dixon, S.L. (2005). *Fluid Mechanics and Thermodynamics of Turbomachinery.* Elsevier Butterworth-Heinemann.

Dubitsky, O. and Japikse, D. (2008 January). Vaneless Diffuser Advanced Model. *Journal of Turbomachinery, ASME*, vol. 130, p. 011020 (10 pages).

Eckardt, D. (1975 July). Instantaneous Measurements in the Jet-Wake Discharge Flow of a Centrifugal Compressor Impeller. *Journal of Engineering for Power, ASME*, vol. 97, pp. 337–346.

Eckardt, D. (1976 September). Detailed Flow Investigations Within a High-Speed Centrifugal Compressor Impeller. *Journal of Fluids Engineering, ASME*, vol. 98, pp. 390–402.

Eckardt, D. (1980). Flow Field Analysis of Radial and Backswept Centrifugal Compressor Impellers, Part I: Flow Measurements using a Laser Velocimeter. In: *Performance Prediction of Centrifugal Pumps and Compressors*, pp. 77–86. ASME.

Eckardt, D. and Trültzsch, K.-J. (1977). Vergleichende Strömungsuntersuchungen an drei Radialverdichter-Laufrädern mit konventionellen Messverfahren. *Forschungsberichte Verbrennungskraftmaschinen*, vol. 237, p. NA.

Haaland, S.E. (1983 March). Simple And Explicit Formulas For The Friction Factor In Turbulent Pipe Flow. *Journal of Fluids Engineering*, vol. 105, pp. 89–90.

Howell, A.R. (1947). Development of the British Gas Turbine Unit. Lecture: Fluid Dynamics of Axial Compressors, ASME Reprint, New York.

Japikse, D. and Baines, N.C. (1997). *Introduction to Turbomachinery.* Concepts ETI, Inc.

Japikse, D. and Baines, N.C. (1998). *Diffuser Design Technology.* Concepts ETI, Inc.

Japikse, D. and Oliphant, K.N. (2005 June 6-9). Turbomachinery Modeling: Explicit and Implicit Knowledge Capturing (2005A). In: *Proceedings of GT2005.* Concepts ETI, Inc.

Johnsen, I.A. and Bullock, R.O. (1965). Aerodynamic Design of Axial Flow Compressors. *NASA SP-36*, Fig. 177.

Johnston, J. and Dean, R. (1966 January). Losses in Vaneless Diffusers of Centrifugal Compressors and Pumps. *Journal of Engineering for Power, ASME*, vol. 88, pp. 49–62.

Krain, H. (1981 October). A Study on Centrifugal Impeller and Diffuser Flow. *Journal of Engineering for Power, ASME*, vol. 103, pp. 688–697.

Krain, H. and Eckardt, D. (eds.) (1978). *The Flow Field in a High-Speed Centrifugal Compressor Impeller. A Comparison of Experimental and Theoretical Results*, vol. B1-25 of *First International Conference on Centrifugal Compressor Techology.* Madras.

Kröger, D.G. (2004). *Air-cooled Heat Exchanger and Cooling Towers. Thermal-flow Performance Evaluation and Design.* PennWell.

Launder, B.E. and Sharma, B.I. (1974 November-December). Application of the energy-dissipation model of turbulence to the calculation of flow near a spinning disc. *Letters in Heat and Mass Transfer*, vol. 1, pp. 131–137.

Launder, B.E. and Spalding, D.B. (1974). The Numerical Computation of Turbulent Flow. *Computer Methods in Applied Mechanics and Engineering*, vol. 3, pp. 269–289.

Lieblein, S. (1959). Loss and Stall Analysis of Compressor Cascades. *Journal of Basic Engineering, ASME*, vol. 81, pp. 387–400.

Lien, F.S. and Kalitzen, G. (2001). Computations of Transonic Flow with the v^2-f Turbulence Model. *International Journal of Heat and Fluid Flow*, vol. 22, pp. 53–61.

Menter, F. (1994). Two-Equation Eddy Viscosity Turbulence Models for Engineering Applications. *AIAA*, vol. 32, no. 1, pp. 1598–1605.

NUMECA International (2010 May*a*). *Theoretical Manual FINE™/Turbo v8.7.* NUMECA International, 5 Franklin Roosevelt Avenue, 1050 Brussels, Belgium, v8b edn.

NUMECA International (2010 March*b*). *User Manual AutoGrid5™ v8.* NUMECA International, 5 Franklin Roosevelt Avenue, 1050 Brussels, Belgium, v8d edn.

NUMECA International (2010 May*c*). *User Manual FINE™/Turbo v8.7.* NUMECA International, 5 Franklin Roosevelt Avenue, 1050 Brussels, Belgium, v8b edn.

Qiu, X., Mallikarachchi, C. and Anderson, M. (eds.) (2007 May). *A New Slip Factor Model for Axial and Radial Impellers*, no. GT2007-27064 in GT2007. ASME, Concepts NREC, Montreal, Canada.

Reneau, L., Johnston, J. and Kline, S. (1967 March). Performance and Design of Straight Two-Dimensional Diffusers. *Journal of Basic Engineering, ASME*, vol. 89, pp. 141–150.

Rothstein, M. (1993). *Entwicklung und experimentelle Untersuchung eines Radialverdichters mit beschaufeltem Diffusor variabler Geometrie.* Doctoral, RWTH Aachen.

Rulth, M.R. and Kelecy, F.J. (2004 Spring). Mapping the Eckardt Centrifugal. Fluent NEWS.

Sayers, A.T. (1990). *Hydraulic and Compressible Flow Machines.* British Library Cataloguing in Publication Data.

Spalart, P.R. and Allmaras, S.R. (1992). A One-Equation Turbulence Model for Aerodynamic Flows. *AIAA-Paper 92-0439*, pp. 5–21.

Stewart, J. (2003). *Calculus*. 5th edn. Thomson Brooks/Cole.

Van der Spuy, J. (2003). Final Report - Spoornet "DEEP" Project: Turbocharger Redesign. Tech. Rep., CAE, registered as Stellenbosch Automotive Engineering (Pty) Ltd.

White, F.M. (2003). *Fluid Mechanics*, vol. Fifth Edition. McGraw Hill.

White, F.M. (2006). *Viscous Fluid Flow*, vol. Third Edition. Mcgraw Hill.

Wiesner, F. (1967 October). A Review of Slip Factors for Centrifugal Impellers. *Journal of Engineering for Power, ASME*, vol. 89, pp. 558–572.

Wilcox, D. (1993). Turbulence Modeling for CFD. Tech. Rep., DCW Industries, Inc., 5354 Palm Drive, La Canada, California.

Wilcox, D.C. (1988). Reassessment of the Scale-Determining Equation for Advanced Turbulence Models. *AIAA*, vol. 26, no. 1, pp. 1299–1310.

Yang, Z. and Shih, T.H. (1993). *A k-ϵ Model for Turbulence and Transitional Boundary Layer*, chap. Near-Wall Turbulent Flows, pp. 165–175. Elsevier-Science Publishers B.V.

Ziegler, K. (2003 September). *Centrifugal Compressor "Radiver" with MTU Impeller - Test Case CD-ROM Readme*. Aachen University, 1st edn.

Ziegler, K., Gallus, H. and Niehuis, R. (2003 January*a*). A Study on Impeller-Diffuser Interaction - Part I: Influence on the Performance. *Journal of Turbomachinery, ASME*, vol. 125, pp. 173 – 182.

Ziegler, K., Gallus, H. and Niehuis, R. (2003 January*b*). A Study on Impeller-Diffuser Interaction - Part II: Detailed Flow Analysis. *Journal of Turbomachinery, ASME*, vol. 125, pp. 183 – 192.

Ziegler, K., Gallus, H. and Niehuis, R. (2003 July*c*). *Experimentelle Untersuchung der Laufrad-Diffuser-Interaktion in einem Radialverdichter variabler Geometrie*. Ph.D. thesis, RWTH Aachen University, Faculty of Mechanical Engineering.

Ziegler, K., Ubben, S. and Niehuis, R. (eds.) (2004 January). *Experimental Investigation of Impeller-Diffuser Interaction Phenomena in a Centrifugal Compressor*, vol. 10 of *2004*. ISROMAC Conference.